Spring 1993

The Influence of Reynolds Number and Atmospheric Effects on Aircraft Wake Vortices Near the Ground

Zhongquan Charlie Zheng
Old Dominion University

THE INFLUENCE OF REYNOLDS NUMBER AND ATMOSPHERIC EFFECTS ON AIRCRAFT WAKE VORTICES NEAR THE GROUND

Zhongquan Charlie Zheng

B. S. August 1984, Shanghai Jiao Tong University, Shanghai, China

M. S. March 1987, Shanghai Jiao Tong University, Shanghai, China

A Dissertation submitted to the Faculty of Old Dominion University

in Partial Fulfillment of the Requirement for the Degree of

DOCTOR OF PHILOSOPHY

Mechanical Engineering and Mechanics

Old Dominion University

May, 1993

Approved by:

Robert L. Ash (Director)

Colin P. Britcher

John H. Heinbockel

George C. Greene

Osama A. Kandil

THE INFLUENCE OF REYNOLDS NUMBER AND ATMOSPHERIC EFFECTS ON AIRCRAFT WAKE VORTICES NEAR THE GROUND

Zhongquan Charlie Zheng

Department of Mechanical Engineering and Mechanics

Old Dominion University

May, 1993

Director: Dr. Robert L. Ash

ABSTRACT

Aircraft wakes represent potential hazards which can control aircraft spacing and thus limit airport capacity. Wake vortex trajectories and strengths are altered radically by interactions with the ground plane and by atmospheric conditions. This work has been concerned with developing more accurate numerical predictions. A two-dimensional, unsteady numerical-theoretical study is presented which has included viscous effects, the influence of stratification, crosswind and turbulence on vortex behavior near the ground plane, using a vorticity-streamfunction formulation.

A two-parameter perturbation procedure has been developed which uses analytic solutions for the initial flow field to accommodate the ground effect region in the numerical simulation. Using an order of magnitude analysis, it was possible to justify the Boussinesq approximations for turbulent wake vortex predictions, including ground effects and atmospheric stratification. It has been shown that the eddy-viscosity turbulence models were not effective in predicting wake vortex flows and a Reynolds stress transport model was implemented.

The numerical solutions to the Navier-Stokes equations have been compared with experimental results for the laminar, unstratified cases and good agreement has been obtained. The computational simulations show that the vortex rebound near the ground plane is caused by ground boundary-layer separation. High stratification levels can confine the motion of the vortex system and alleviate the primary vortex strength. Vortex

turbulence influences vortex trajectories more strongly than it influences the rate of change in vortex strength. Weak crosswinds cause the upstream primary vortex to rebound less strongly than the downstream vortex. Finally, suggestions are made for future research.

Dedication

To my dear wife Shirley, who is always my resource of inspiration, encouragement, confidence and perseverance, who has shared with me all the frustration, the happiness, the worry and the release during the research work. Without her patience and understanding, this work would never be done.

Acknowledgments

I would like to express my gratitude to Dr. Robert L. Ash for being my advisor. It is my great honor to have him to guide my doctoral study. He impresses me by his professional knowledge as well as his personality. I would like to thank Mr. George C. Greene for his support of this research. His profound intuition of vortex physics has always been very helpful for the research work. I am happy to have Dr. Osama A. Kandil in my guidance committee, who taught many of my Ph.D. courses and who has shared his valuable research ideas and given suggestions for the work. I am very thankful to Drs. Colin P. Britcher and John H. Heinbockel who have spent a lot of time with my candidate test, research proposal and this thesis.

The author would also like to thank NASA Langley Research Center for the support of NASA research grants NAG1-987 and NAG1-1437.

Table of Contents

List of Figures

Nomenclature

A, B	constants depending on the initial conditions of the vortex pair in potential theory
a, b	modeling coefficients of the Reynolds stress transport equation
a, b, c, d	parameters in grid mapping
C_α, C_β	coefficients of Reynolds stress transport model for isolated vortex
C_Λ	turbulnt length scale coefficient of the Reynolds stress transport model in ground effect problem
c_p	heat capacity at constant pressure
c_D, c_k	coefficients in one-equation turbulence model
c_1, c_2, c_μ	coefficients in two-equation turbulence model
erf, erfc	error function, complementary error function
F_v	Froude number
f_{pq}, g_{pq}	functions for asymptotic solutions
g	gravitational acceleration
h_0	initial height of the potential vortex pair
k	heat conduction coefficient, or turbulent kinetic energy
k_o	initial maximum turbulent kinetic energy
L_∞	vertical atmospheric length scale
l	turbulent mixing length
M	Mach number of the vortex flow, or Donaldson's turbulence scale factor
N	dimensionless Brunt-Väisälä frequency
N^*	Brunt-Väisälä frequency (1/second)
n	dimensionless density gradient
P	outer flow pressure
p, p_0, p_1, $\cdots$	inner flow pressure
p	total thermodynamic pressure

$\widetilde{p}$	dimensionless pressure departure or time-averaged dimensionless pressure departure
p'	dimensionless pressure departure fluctuation
p_∞, p_o	nominal and prescribed atmospheric pressures, respectively
Δp	pressure departure
Q_I, Q_{II}	triple-velocity-correlation modeling coefficients in the Reynolds stress transport model
q	a measure of turbulent kinetic energy defined as $(2k)^{1/2}$
R	gas constant
Re	circulation Reynolds number
Re_Λ	turbulent length scale Reynolds number
r	radial distance from the vortex center
r^*	vortex core radius of the isolated vortex
$\hat{r}$	dimensionless coordinate for the isolated vortex problem
r_c, r_o	initial vortex core radius
s, s_0	half span and initial half span of the vortex pair
T	total thermodynamic temperature
$\widetilde{T}$	dimensionless temperature departure or time-averaged dimensionless temperature departure
T'	dimensionless temperature departure fluctuation
ΔT	temperature departure
T_∞, T_o	nominal and prescribed ambient temperatures, respectively
t	time or dimensionless time
U, V, W (U_1, U_2, U_3)	lateral, vertical and axial velocity components, respectively, for outer flows, mean flows or ambient flows
U_0, U_1, $\cdots$	outer velocities at the edge of outer and inner flows
U_c, V_c	velocity components of a pair of potential vortices with their associated images
U_∞, V_∞	uniform velocity outside the crosswind boundary layer
u_c	crosswind speed
u, v, w (u_1, u_2, u_3)	lateral, vertical and axial components of total velocity, respectively, or inner velocity components for the asymptotic solutions

u', v', w' (u_1', u_2', u_3')	lateral, vertical and axial components of velocity fluctuations, respectively
V_o	initial maximum tangential velocity of the isolated vortex
X, Y	coordinates in the transformed domain
$X(t)$, $Y(t)$	vortex center position in ground effect problem
X_0, Y_0, x_0, y_0	initial locations of the vortex pair
x, y, z (x_1, x_2, x_3)	lateral, vertical and axial coordinates, respectively
x_l	the farthest horizontal distance from the symmetry plane
y^*	outer parameter at the edge of boundary layer
α	coefficient in the Reynolds stress transport model
β	prescribed temperature lapse rate
δ	crosswind boundary-layer thickness
δ_{ij}	Kronecker delta
ϵ	small parameter in the asymptotic solutions, or the turbulence dissipation
$\epsilon_{r\theta}$	mean strain rate component
η	inner vertical length variable in the asymptotic solutions, constant of mixing length
η^*	inner parameter at the edge of boundary layer
Γ, Γ_0	circulation, initial circulation of vortex wakes
γ	specific heat coeffecient or a solution to the transcendental equation the Chapter 6
Λ, Λ_I, Λ_{II}	turbulence length scales in the Reynolds stress transport model
κ	von Karman constant
λ	turbulent length scale factor
μ	dynamic viscosity
μ^*	second coefficient of viscosity
ν, ν_o	kinematic viscosity
ν_t	kinematic eddy-viscosity
Ψ, Ψ_0, $\Psi_1, \cdots$	streamfunctions for outer solutions in the asymptotic solutions
ψ, ψ_0, ψ_1, $\cdots$	streamfunctions for inner solution in asymptotic solutions
ψ_n	streamfunction on the grid locations adjacent to the ground

ρ	total thermodynamic density
$\widetilde{\rho}$	dimensionless density departure or time-averaged dimensionless density departure
ρ'	dimensionless density departure fluctuation
ρ_∞, ρ_o	nominal and prescribed atmospheric densities, respectively
$\Delta\rho$	density departure
σ_k	turbulent kinetic energy Prandtle number
σ_ϵ	turbulent dissipation Prandtle number
ζ	vorticity
∇	nabla operator

Subscripts

f	subscript for the variables in fixed coordinates

Chapter 1 Introduction

It is well-known that aircraft trailing vortex wakes can cause serious loss of control when following aircraft encounter them. The following aircraft can be subjected to rolling moments which exceed the aircraft's roll control authority, leading to a dangerous loss of altitude, and to possible structural failure. With the advent of large transport aircraft, the wake vortex problem has taken on added significance. Since the probability of an aircraft-vortex encounter is greatest in airports where aircraft operate in close proximity, aircraft spacing at congested airports is dictated by the characteristics of the vortex wakes left in the terminal area (Hallock, 1992). Moreover, the hazard is more severe near the ground because of the limited time and space available to maneuver the aircraft so as to recover from an upset. Therefore, prediction of wake vortex trajectories and strengths is especially important for effective airport flight control and maintain maximum traffic volume.

In order to fully assess the hazard, complete information is needed regarding such processes as the initial organization of the wake vortex sheet, the subsequent roll-up and generation of primary vortices, the descent and decay of the wake in a real atmosphere, and the response/control characteristics of the encountering aircraft. The detailed treatment of aircraft wake vortex formation (e.g. Kandil, Wong and Liu, 1991 and Wong, Kandil and Liu, 1992) is beyond the scope of the present research and will not be treated here. Rather, this work has focused on the viscous interaction between

vortex wakes and the ground plane, including atmospheric effects such as stratification, wind shear and turbulence. An in-depth understanding of the mechanisms that bring about wake dissipation can provide information which could enable augmentation of the decay process, and thus lead to the accelerated destruction of wake vortices, thereby contributing to the alleviation of airport congestion.

A numerical-theoretical study of the motion of a two-dimensional, unsteady vortex pair in close proximity to the ground is presented here. The purpose of this research was to predict the flow pattern, structure, motion and persistence of trailing vortices, approximating those generated by aircraft after the initial roll-up stage. While the wake structure is established quickly, within a few spans during roll-up, the resulting vortex pair is stable for a long time, sometimes over several minutes, and thus poses a safety hazard. The character and potential hazard of the residual wake structure are not well understood (Widnall, 1975). The transverse motions of these vortices, without the inclusion of the sinusoidal instability (Crow, 1970), are slow enough, relative to the flight speed, to be described by a two-dimensional model (Atias and Weihs, 1984).

A representative airplane type considered in this study is the Boeing 747. Its circulation Reynolds number (Γ/ν) is on the order of 10^7. Its span, which is a characteristic length for this problem, is about 60 m. The largest near ground lapse rate for a quasi-steady atmospheric temperature gradient is 0.2 C°/m, and this study has shown that the Boussinesq approximations can be used in modeling vortex wake behavior. That is, the density variation can be neglected except for the body force terms in momentum equations. The governing equations for turbulent, stably stratified, incompressible flows are

needed for the computations. The derivation procedure, which is not a simple matter, will be discussed in Chapter 3.

In the numerical computations, the vorticity-streamfunction formulation is used to model an unsteady, two-dimensional, incompressible flow approximation of the problem. One reason for the use of vorticity-streamfunction formulation is that the number of unknowns is reduced from three (two velocity components and pressure) to two. Furthermore, in this study the vorticity is of interest in its own right and it is desirable to compute its evolution directly, rather than compute the primitive variables and numerically differentiate the results. Besides, the pressure boundary condition on the ground is more difficult to represent than that for the vorticity. Then in Chapter 4, the computational domain and grid spacing have been chosen carefully for proper resolution which is conformable with available computational resources and budgets. The boundary conditions for the vorticity-streamfunction formulation are developed in the transformed domain.

Finite-difference schemes are developed to obtain the difference equations for the problem. At low altitude, the strong effects of the viscous ground boundary not only preclude inviscid theories and approximate models (Greene 1986), but these viscous effects also represent difficulties for finite-difference techniques. These vortex wake flows produce very thin shear layers near the ground boundary as well as at various other time-dependent locations throughout the region. A specially designed computational approach for this application is presented. In Chapter 5, a time-dependent, double-series, asymptotic expansion, in terms of circulation Reynolds number and dimensionless time, is developed for the initial flow field. The initial velocity field problem has been addressed previously by Peace and Riley (1983), but they used a single series expansion

in time, scaled by Reynolds number (t/Re), to start their asymptotic solution. Their method has difficulties in rigorously matching all the inner terms with the outer flow, particularly the pressure field which was not considered in their expansion. This so-called *unsteady Reynolds number* single-series expansion was replaced by a double-series similar to the method that had been used by Nam (1990), who expanded the series further in non-dimensional time. The double-series was required because the similarity conditions (Schlichting 1979) based on the unsteady Reynolds number are not always satisfied for the general unsteady flow. Since the boundary-layer thickness depends strongly on both Re and the elapsed time after the impulsive start, the choice of these two expansion parameters seems quite proper, a fact which has been shown previously by Nam (1990) for a different problem, and is developed in Chapter 5 for the wake vortex problem.

Turbulence models for vortex-dominated flows are evaluated in Chapter 6. Redistributions of the Reynolds stresses due to centrifugal and streamline curvature effects in these vortex flows have been reviewed in Bradshaw (1973) and Bushnell (1991). An isolated turbulent vortex, also studied by Donaldson (1972a), has been used as a test problem, because it only requires a small number of grid points, while incorporating streamline curvature and vortex core relaminarization effects. It is demonstrated in the test problem that eddy-viscosity approaches are inherently inadequate and that a Reynolds-stress transport model should be used to calculate turbulent vortex flows.

The computational results, performed on the Cray II and Cray Y-MP multi-CPU machines at NASA Langley Research Center, simulating Reynolds number effects, stratification and crosswind effects, are discussed in Chapters 7, 8 and 9, respectively.

Finally, conclusions from the present work and suggestions for the future research are contained in Chapter 10.

Chapter 2 Summary of Previous Research

In this chapter, a brief review of pertinent literature on the evolution of wake vortices of typical aircraft is presented. The discussion includes consideration of ground effects, stratification, wind shear and turbulence.

2.1 Ground Effects

As stated in the first chapter, one of the critical regions where wake penetration by other aircraft is of great concern is in the airport terminal area. The problem is most severe near ground level, where the aircraft may not have sufficient time or space to recover from the influence of the wake encounter. Also, the ground plays an important role in influencing the trajectory and strength of these generated vortex wakes. Viscous interaction with the ground boundary-layer flow changes the motion of the vortices dramatically. In practice, several other effects may be expected to modify the behavior of the vortices close to the ground. Because crosswind velocity profiles vary with the altitude from the ground plane, so do their effects on the vortices. Turbulence level and stratification intensity are different near the ground surface, when compared to conditions away from the ground.

Assuming that the ground surface acts as an image plane, potential theory representation of a pair of counter-rotating vortex filaments above an infinite plane yields reasonable estimates of wake vortex descent rates in an otherwise quiescent atmosphere,

as long as the wake is sufficiently far from the ground (Dee and Nicholas 1968, Saffman 1979). Following the methods of classical hydrodynamics, the trajectories of this four vortex system with mutual induction (a vortex pair and its images, as shown in Figure 2.1) have been given by Lamb (1945), where

$$1/x^2 + 1/y^2 = A\,, \tag{2.1}$$

and A is a constant depending on the initial positions, x_0 and h_0, of the vortices. These vortex system equations can be derived from the fact that the circumferential velocity, due to a single vortex of strength Γ_0, is

$$V = \Gamma_0/2\pi r \tag{2.2}$$

where r is the distance from the vortex axis. From Eqns. (2.1) and (2.2) Dee and Nicholas (1968) derived the time dependent positions

$$x^2 = \frac{2\left[64\pi^2/A\Gamma_0^2 + A(t+B)\right]}{64\pi^2/\Gamma_0^2}\left\{1 \mp \left(\frac{64\pi^2}{A^2\Gamma_0^2(t+B)^2} + 1\right)^{-\frac{1}{2}}\right\} \tag{2.3}$$

$$y^2 = \frac{2\left[64\pi^2/A\Gamma_0^2 + A(t+B)\right]}{64\pi^2/\Gamma_0^2}\left\{1 \pm \left(\frac{64\pi^2}{A^2\Gamma_0^2(t+B)^2} + 1\right)^{-\frac{1}{2}}\right\} \tag{2.4}$$

where B is another constant, defined by

$$B = \frac{4\pi}{A\Gamma_0}\left[\frac{Ah_0^2 - 2}{\left(Ah_0^2 - 1\right)^{1/2}}\right] \tag{2.5}$$

and where the upper alternating sign applies when $t < B$ and the lower sign applies when $t > B$. Hence, the vertical and horizontal displacements of the line vortices can be calculated as a function of time to give the potential theory vortex positions.

Harvey and Perry (1971) examined the observed flight data of Dee and Nicholas (1968) and found a noteworthy discrepancy which had not been emphasized in their original report. It was shown that in many tests the vortices departed from the path predicted by potential theory by rising again, after descending to within close proximity of the ground (Figure 2.2). Apparently, wake vortices rebound as well as separate when they interact with the ground.

Some of Harvey and Perry's experiments (1971) were conducted on a single vortex shed by a half-span wing over a moving floor in a low-speed wind tunnel. The primary objective of those experiments was to explain the cause of the vortex rebound phenomenon, which is considered to be a significant feature of the ground effect and which can influence terminal flight conditions. The experiments inferred that rebound was caused by separation of the ground boundary-layer flow underneath the vortex (see Figure 2.3). It is known that a trailing vortex system induces a cross flow along the ground with an attendant suction peak some place beneath the vortex core. The boundary layer, resulting from the interaction of this cross flow with the ground, has to negotiate an adverse pressure gradient once it has passed outboard from the suction peak under the vortex. When the vortex is sufficiently close to the ground, the pressure gradient is strong enough for separation to occur. A bubble containing vorticity of opposite sign to that of the primary vortex forms near the separation point and eventually detaches from the ground as a secondary vortex, fed by a vortex sheet emanating from the separation point. Although the subsequent interaction is complicated, Harvey and Perry argued that the development of the secondary vortex causes the primary vortex to rise.

Later Barker and Crow (1977) observed rebound for a two-dimensional vortex pair, generated in water, approaching either a free upper surface or a rigid horizontal plane beneath the water. They asserted that the rebound phenomenon could be attributed to the effect of finite vortex core size. Their explanation was intuitive, using the idea that an elliptical vortex core, which was originally a circular core and had been deformed while nearing the surface, might have a tendency to rotate as it moved along its "image plane". That rotation would lead to changes in both the distance of the vortex center from the bounding surface and in the propagation velocity of the vortex center. However, their arguments lacked rigorous proof for the causes of vortex rebound.

By introducing a pair of elliptical core vortices with axis ratio and orientation given by the inviscid theory of Moore and Saffman (1971), Saffman (1979) showed that in the framework of an inviscid theory it was not possible to explain the rebound phenomenon by finite core size and that the wallward velocity component could not change sign. Navier-Stokes computational results, performed by Bilanin, Teske and Hirsh (1978), demonstrated that rebound from a solid boundary did not occur unless the viscous, no-slip boundary condition was applied, even though the vortex cores were of finite size.

Recently, experiments were designed by Liu and Srnsky (1990) to minimize flow channel sidewall effects, which can mask the ground effect. From their dye visualization results in water, they identified the emergence of secondary, counter-rotating vortices near the ground plane, outboard from the vortex wake. They determined that as soon as the secondary vortex began to form, rebound of the main vortex was initiated. Specifically, the primary and secondary vortices form a vortex pair that moves upward. Those results

have confirmed the scenario of secondary vortex generation suggested by Harvey and Perry (1971).

Although there is no free surface boundary in the problem considered here, the rebound phenomenon was also observed by Barker and Crow (1977), Sarpkaya and Johnson (1983), Bernal *et al.* (1989) and Liu, Hwang and Srnsky (1991), where their vortices approached a free surface in water tank experiments. Sarpkaya and Johnson (1983) suggested that sidewalls could be responsible for the rebound. Bernal *et al.* (1989) investigated the effects of surface contamination and showed that surface contamination due to dust or surface active agents effectively caused the free surface to act like a solid boundary during vortex impingement; an opinion which was shared by Liu, Hwang and Srnsky (1991). Liu, Hwang and Srnsky (1991) suggested that no practical clean-surface existed that would fulfill the free-surface boundary condition requirements. However, low Reynolds number computational results by Peace and Riley (1983) predicted the rebound for a theoretically enforced stress-free boundary. Since rebound appeared for both a no-slip and a stress-free boundary, they argued that flow separation, which is not a feature associated with the stress-free boundary condition, did not occur even for the no-slip cases at the Reynolds numbers used in their calculations. Their Reynolds numbers were at least two orders of magnitude lower than those reported in experiments. They agreed that the occurrence of flow separation, observed by Harvey and Perry (1971), would certainly induce a rebound of the incident vortex. They stated that even in the absence of separation, rebound was caused by viscous effects, regardless of whether or not the boundary conditions were no-slip or zero shear. They argued that the viscous displacement effect of the no-slip boundary was sufficient to force the vortex away from

the boundary. For the zero-stress case there was no such effect and viscous effects were only significant at the boundary when vorticity had diffused from the neighborhood of the vortex pair to the ground boundary. This may explain why Orlandi (1990) found that for a flat slip-free surface, rebounding diminished with increasing Reynolds number until it ceased.

Another aspect of vortex-boundary interaction which is unique to free surface boundaries is a time-dependent nonlinear free surface interacting with a viscous vortex pair (Ohring and Lugt 1991). The generation of surface vorticity and secondary vortices on a curved, wavy free-surface were found to induce a specialized type of rebound of the main vortex.

In summary, aspects of the rebound phenomenon can be explained over different Reynolds number ranges. For low Reynolds number cases where separation may not occur, the viscous displacement will be large enough to force the primary vortex away from its no-slip boundary, and the vorticity diffusion on a free surface will cause the rebound. For high Reynolds number cases the no-slip boundary layer is very thin, so the separation scenario inferred by Harvey and Perry (1971) is correct for solid boundaries, but the rebound phenomenon does not show up on free surfaces because the diffusion process is not significant at high Reynolds numbers.

Many theoretical studies of a vortex pair in ground effect have been reported using inviscid theory, discrete vortex methods, and finite difference schemes. Potential theory has failed to describe the ground effect, even when elliptical vortex cores were considered (Saffman, 1979). Another type of inviscid method was introduced by Liu and Ting (1987), who studied the interaction of decaying trailing vortices in a spanwise shear flow near

the ground. They combined the matched asymptotic solution for decaying vortical spots with an Euler solution for the background, unsteady, rotational flow. Although some viscous core effects could be included in the leading terms of their asymptotic expansion, there was no ground boundary layer and the method could not be extended to include direct viscous interaction between the vortex and the ground. Starting from Leonard's (1980) methods, which approximated the vortex sheet by an array of point vortices, Atias and Weihs (1984) developed a discrete vortex method which simulated viscous effects via vorticity generation near the ground using distributed planar vortex elements. This method was also developed and applied by Chorin (1973, 1978) to approximate unsteady boundary layers. Since the number, type and distribution of the discrete vortices produce considerable uncertainty and yet the viscous interaction is still not properly represented, Navier-Stokes calculations with finite difference schemes have been adopted.

Bilanin, Teske and Hirsh (1978) developed a numerical simulation of a trailing vortex pair near the ground for both laminar and turbulent conditions. One of their important conclusions was that the proximity of a ground plane reduces the vortex hazard by "scrubbing". That is, the vortex pair separates or spreads and interacts viscously with the ground, thereby reducing its strength more rapidly.

The problem of the initial ground vorticity distribution was studied by Peace and Riley (1983) using an asymptotic solution to describe the early stages of fluid motion. Their low Reynolds number computational results showed the rebound for either a no-slip or a stress-free boundary.

A numerical study of the effects of stratification and wind shear on the evolution of aircraft wake vortices near the ground has been reported by Delisi, Robins and Fraser

(1987), who found that both effects reduce the extent of vortex rebound. They employed a mixed no-slip/slip boundary condition on the ground plane which required an empirical adjustment for different flow cases.

It is noted that here, in the absence of ground effects, even in more realistic atmospheric conditions, an approximate prediction model developed by Greene (1986) has demonstrated surprisingly good agreement with experimental data. That method was based upon empirical engineering approximations. Unfortunately, the extension to include ground effect does not appear to be compatible with Greene's model.

2.2 Stratification

The descent of a vortex pair in a stratified atmosphere poses a problem that has not been completely solved. There are fundamental differences in assumptions made previously by others and quite different conclusions have been reached (see Widnall 1975). For levels of stable stratification (when atmospheric temperature increases with the altitude from the ground) which occur typically in the atmosphere, inviscid studies (Scorer and Davenport 1970, Tombach 1971, Kuhn and Nielsen 1972, Lissaman et al. 1973, Crow 1974) have produced quite different results from the intuitive notion that stable stratification ought to produce effects similar to a rigid barrier, causing the vortices to decelerate and spread apart. All of these investigators concluded that stable stratification in an inviscid medium increased the rate of descent of the vortex pair with time. Ivanov *et al.* (1987) identified two important effects due to a stably stratified medium: a buoyancy effect and a vorticity effect. The buoyant force, due to departure from equilibrium density level, produces vortex deceleration. At the same time, the density difference at the edge of the moving medium leads to the generation of a vortex sheet. As a result

of the convective drift of vorticity along the edge of the recirculation zone, this sheet accelerates the vortex pair. The competition between these factors is extremely complex. However, the problem with any inviscid analysis of vortex descent is that it neglects the transport of vorticity across streamlines. The inviscid behavior described is not observed experimentally in any wake of appreciable age (Tombach 1973, Sarpkaya and Johnson 1983, Liu and Srnsky 1990), where the vorticity transport is dominant.

Liu and Srnsky (1990) discussed stratification effects with different ranges of internal Froude number. The Froude number in their experiments was defined as F=U/NL, where U, N and L are the characteristic scales for the velocity, Brunt-Väisälä frequency and characteristic length, respectively. At low Froude numbers, where the stratification effect can be large, Saffman's (1972) linear inviscid prediction agrees well with laboratory results (Sarpkaya and Johnson 1983, Liu and Srnsky 1990) and with numerical results (Hecht *et al.* 1979, Hirsh 1985). At high Froude numbers, Crow's hypothesis (1974) of detrainment, which proposes that the vortex translation speeds up and the vortex separation contracts, is only expected to apply within a short period. Since the inertia of the vortex system is dominant at high Froude numbers, the full nonlinear equations are then necessary (Hirsh, 1985).

Nonlinear numerical calculations have been performed by Hecht *et al.* (1979), Hirsh (1985), Delisi, Robins and Fraser (1987) and Robins and Delisi (1990). Hecht *et al.* (1979) calculated turbulent vortices in stably stratified fluids for both vortex rings and vortex pairs, using the second-order closure model of Donaldson (1972a). In a range of Froude numbers from 1 to 10, the descent velocity was a monotonically decreasing function and the spacing of the vortices in vortex pairs was nearly constant.

The Euler calculations of Hirsh (1985) demonstrated that for low Froude numbers, a linear inviscid description of the flow was possible. A specially constructed numerical procedure that conserved energy was used when there was nonlinear transfer between kinetic and potential energy. At low Froude numbers, the results were in good agreement with the experiments of Sarpkaya and Johnson (1983) and Liu and Srnsky (1990) and with the linear theory of Saffman (1972).

Robins and Delisi (1990) studied the influence of vertical shear and stratification effects on the evolution of a vortex pair away from the ground. Their numerical model, developed originally for use in gravity-wave-critical-level studies, was applied. Their model separated the solution for horizontally averaged quantities from the perturbations about those averages. Their equations for the average quantities and each term of their exponential series expansions of the perturbations were then calculated. With specified damping, their prediction of vortex ascent, obtained for non-sheared flow calculations agreed with the laboratory experiments of Barker and Crow (1977), Tomassian (1979) and Sarpkaya and Johnson (1983).

Delisi, Robins and Fraser (1987) also computed the case with ground effect, by applying *ad hoc* non-slip/slip-free boundary conditions along the ground plane. Their results showed no rebound of the vortex pair and that the inclusion of stratification inhibits the horizontal propagation of the vortices in ground effect.

2.3 Cross Wind

In a cross wind, the atmospheric shear vorticity must introduce some asymmetry into the wake. Aircraft flight tests have shown that the smoke contained in one of the two primary trailing vortices could vanish while the second smoke trail remained intact (see

Burnham *et al.*, 1978). Numerical calculations reported by Rossow (1976) and Bilanin, Teske and Hirsh (1978) demonstrated that the vortex with the same rotational sense as the shear gradient survives, while the vortex of opposite rotational sign is distorted rapidly. In addition, in the measurements by Burnham *et al.* (1978), vortex system tilting phenomenon was observed.

The unanswered question is: Why does the upwind vortex sometimes appear to rise relative to the downwind vortex, while at other times the opposite seems to occur (Donaldson and Bilanin 1975)? If atmospheric shear is constant and the wake is not in ground effect, a closed form potential flow solution approximation was found by Lissaman *et al.* (1973). For this ideal solution, even with wind shear, the two vortices descend at their classical rates, $v = \Gamma/4\pi s_0$, where Γ is the circulation and s_0 is the half-span of the vortex pair, and there is no tendency for the vortex pair to tip or tilt. The effect of a ground plane on the ideal solution was considered by Brashears, Logan and Hallock (1975). They studied the upwelling of streamlines by considering the stagnation point positions. The upper stagnation point of the two stagnation points in the flow field, caused by the interaction between crosswind shear and the vortex pair, agreed with the trends as to which vortex was observed to rise. But their solution could not predict the tilting phenomenon. The results showed that weak vertical shear will cause the downwind vortex to rise more rapidly than the upwind vortex and that strong vertical shear will have the opposite effect. The results of Delisi *et al.* (1987) for stable stratification, with and without ground effect, showed the same trend. Their ground effect results also showed that vertical shear reduced the rebound when compared with non-sheared flows.

2.4 Turbulence

The aging of a wake vortex will be influenced by turbulent diffusion, entrainment and dissipation. Two types of turbulence effects must be considered. Obviously, the ambient turbulence generated within the atmospheric background must be considered. In addition, the turbulence originating from or generated by the vortices must be considered. (While it is known that Helmholtz and Rayleigh instabilities can occur during roll-up of the vortex sheets, it is not possible to achieve that level of resolution with the current computational capability.) In practical cases, one cannot distinguish atmospheric turbulence effects from vortex-generated turbulence effects. However, since they must have distinctly different effects on the evolution of the vortex structures, they will be discussed separately in this chapter.

2.4.1 Ambient Turbulence

The life-span of wakes in an ambient turbulence environment have been studied experimentally by Tombach (1973), Crow and Bate (1976), Sarpkaya and Daly (1987) and Liu (1992). The wakes were generated by a light airplane in Tombach's (1973) experiments. He proposed that the life-span of wakes correlates with the reciprocal of the cube root of turbulent dissipation. He showed a strong correlation between atmospheric turbulence and both vortex linking and bursting instabilities. The linking instabilities, which result from mutual induction instabilities of the vortex pair, called Crow instabilities (Crow 1970), are considered to be inviscid instabilities (Donaldson and Bilanin 1975). Crow and Bate (1976) investigated large scale atmospheric turbulence effects and found that the linking instabilities were the first in a sequence of processes

that destroyed the coherence of a vortex wake. Sarpkaya and Daly (1987) suggested that the life-span of the vortices was influenced strongly by the intensity of turbulence and, to a lesser extent, by its scale. In Liu's (1992) tow-tank experiments, weak turbulence with large integral scales, compared with the vortex separation distance, produced flows where vortex linking was the dominant mode of instability. As the turbulence intensity was increased, vortex bursting occurred and eventually replaced linking as the dominant mode. For turbulence with small integral scales, the bursting instability was dominant and relatively weak intensity, small-scale turbulence was more effective than its large-scale counterpart in reducing the life-span of the wake. Ground effects were not considered in these experiments.

The effect of vortex transport of atmospheric turbulence was studied theoretically by Donaldson and Bilanin (1975) and Bilanin, Teske and Hirsh (1978) in their investigation of rates of decay and descent of vortex pairs. Their two-dimensional models were incapable of addressing the behavior either of sinusoidal instabilities or of vortex breakdown since both phenomena are inherently three-dimensional. Donaldson and Bilanin (1975) used eddy-viscosity ideas to model velocity-vorticity fluctuation correlations. Using a constant ambient turbulence kinetic energy and the one eighth separation distance between the vortices as their integral scale, they obtained expressions for descent rates and circulation as functions of time, in the absence of a ground boundary. The maximum wake descent rates, given by their expressions, were in rough agreement with the observations of Tombach (1973). Greene (1986) used the same relation in his approximate model for turbulence effects.

Bilanin, Teske and Hirsh (1978) applied a second-order moment closure model developed by Donaldson (1972a). The initial vortex turbulence was computed together with atmospheric turbulence, assuming constant shear and homogeneous turbulence in the absence of a vortex wake. The background turbulence was assumed to be the result of a gradient in the headwind and the turbulence levels were determined using the "super-equilibrium" limit for the turbulent transport model (Donaldson 1973). The results for a vortex Reynolds number of 10,000, without ground effect, showed substantial diffusion of the vorticity, with a drop in maximum value of about an order-of-magnitude below the maximum vorticity value in the zero background turbulence case. Ground boundary effects were also considered in the calculations at Reynolds numbers of 100 for a laminar case and 10,000 for a turbulence case.

2.4.2 Vortex Core Turbulence

There are turbulent regions in the trailing vortices, produced during roll-up of vortex sheets. Barker and Crow (1977) determined from their flow-visualization photographs that two-dimensional vortices were unstable in an annular region surrounding the core. Transition began in the annular region, via instability waves which progressed radially inward and outward. The flow in the vortex recirculation cell remained fully turbulent until the vortices had dissipated, except for a small region near the center of each vortex. This inner region, or vortex core, appeared to remain laminar and grew slowly in radius during the evolution of the vortex. Intermittent patches of highly turbulent and partially relaminarized fluid in the vortex core were also found in the experiments by Bandyopadhyay, Stead and Ash (1991). Their experiments revealed the exchange

of momentum between the outer turbulent region and the core carried out by organized motions.

An essential understanding of the nature of viscous transport of vortex wakes in a quiescent, neutrally stable atmosphere is still difficult. Experimentally, it is difficult to carry out systematic experiments because some parameters such as the core size and turbulence distributions in the core cannot be varied systematically and quantitative measurements of turbulence stresses are smeared by the vortex motion, owing to the presence of a probe and the "vortex meandering" due to free stream turbulence (Phillips and Graham 1984).

Theoretically, many problems associated with turbulence modeling, even for two-dimensional vortex wakes, still remain. The streamline curvature in vortex flows is expected to influence turbulence transport and the extra rates of strain must be modeled. Consideration of vortex core stability via Rayleigh stabilization or destabilization should also be included. The central, forced-vortex region, defined as an inner viscous region or vortex core, exhibits flow field and turbulence characteristics with unusual and interesting behavior. Such subtle details as vortex core relaminarization, along with the local anisotropy of Reynolds stresses, invalidate eddy-viscosity models for wake vortex problems. The influence of streamline curvature on turbulent flows has been reviewed by Bradshaw (1973) and Bushnell (1991).

Attempts have been made to establish the laws governing the flow in a turbulent line vortex along lines similar to the methods used in turbulent boundary-layer theory. The belief was that there was somehow a similarity between vortex cores and the viscous sublayers which occur in turbulent boundary layers. Ragsdale (1961) tested the

applicability of mixing length theory to a compressible, turbulent vortex system, using both Prandtl and von Karman similarity functions. Some of his expressions failed to correlate with experimental data. A logarithmic distribution of circulation was utilized by Saffman (1973) for the outer region (outside the vortex core) and the inner region was represented using solid body rotation. Iversen (1974) studied a so-called "plateau" region trailing from a lifting airfoil where the decay of the vortex due to viscous or turbulent shear was very slow. He suggested that the delay in vortex decay was due to nonequilibrium turbulence in which the magnitude of the turbulent shear stresses take a significant period of time to catch up with the turbulent energy distribution. Both constant and variable eddy-viscosity models were applied to his calculations of the decay of a single line vortex. Donaldson and Bilanin (1975) studied a pair of vortices in descent, under the condition that the primary turbulent fluctuations were not due to the atmosphere but were due to the vortex swirling motion itself. The expressions they developed, using simple eddy-viscosity, were similar to the drag effect term in Greene's (1986) approximate model. Both approaches showed that turbulent transport, associated with the vortex motion, was incapable of stopping the descent of a vortex pair in a neutrally stable environment but that it could reduce the rate of descent.

Raj and Iversen (1979) employed zero-, one- and two-equation models in computational simulations of turbulent vortex merger and decay. They utilized a spatially-varying mixing-length model to incorporate the streamline curvature effect. For appropriate choices of constants, the results of the zero- and one-equation formulations could be made to agree well with that of the two-equation model. Ayad and Cermak (1980) used a standard k-ϵ model with coefficients taken from Launder and Spalding (1974) to study

the interaction of tornado-like swirling flows with the ground. Their maximum tangential velocity result was in qualitative agreement with the results of Lewellen, Teske and Sheng (1979), who used a second-order turbulence closure. Recently, Childs (1990) compared the standard k-ϵ model (Launder and Spalding, 1974) with the one modified for curvature for the ground vortex region beneath impinging jets. The *ad hoc* model coefficients had to be adjusted to achieve reasonable results.

Using a super-equilibrium model and Taylor's (1923) stability analysis, Donaldson (1972b) determined, for the case of a turbulent line vortex, that eddy-transport models led to erroneous conclusions. He then developed an invariant Reynolds stress transport model (Donaldson and Sullivan 1971) to calculate the decay of isolated vortices. Encouraging results were obtained that included similarity solutions which were reached after long time iteration. Since streamline curvature effects and anisotropy of the normal stresses are incompatible with eddy-viscosity models but remain crucial to describe vortex motion properly, Reynolds stress transport models have to be considered. Reynolds stress transport models have the advantage, when applied to vortex flows, of including the physical mechanisms that the other models cannot imbed.

At the second moment closure level, algebraic stress models have also been applied to model swirl in turbulent flow systems (Sloan, Smith and Smoot 1986). Unfortunately, in some cases these algebraic stress models can be shown to reduce to eddy-viscosity models. Consequently, for the isolated turbulent line vortex case these models have drawbacks similar to those described by Donaldson (1972b) because they force turbulent shear in the vortex to be related directly to the local deformation.

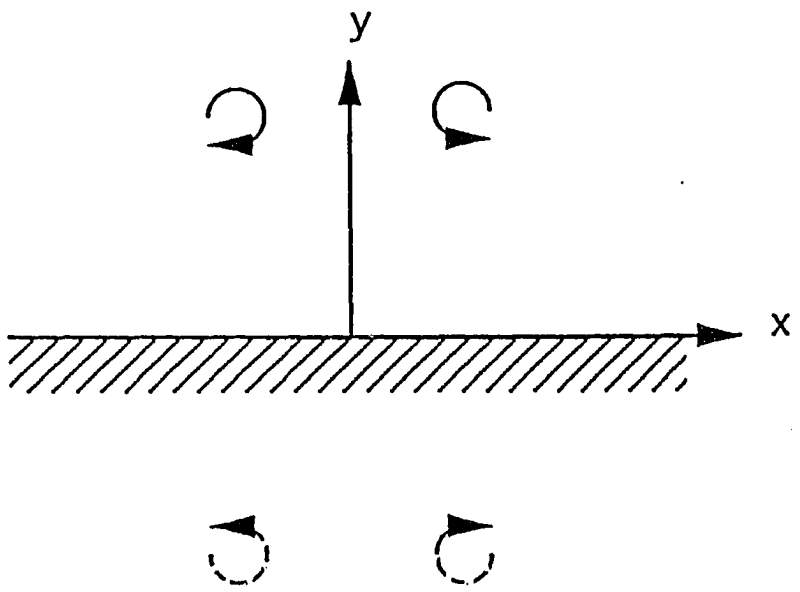

Figure 2.1 A vortex pair above an infinite plane and its images

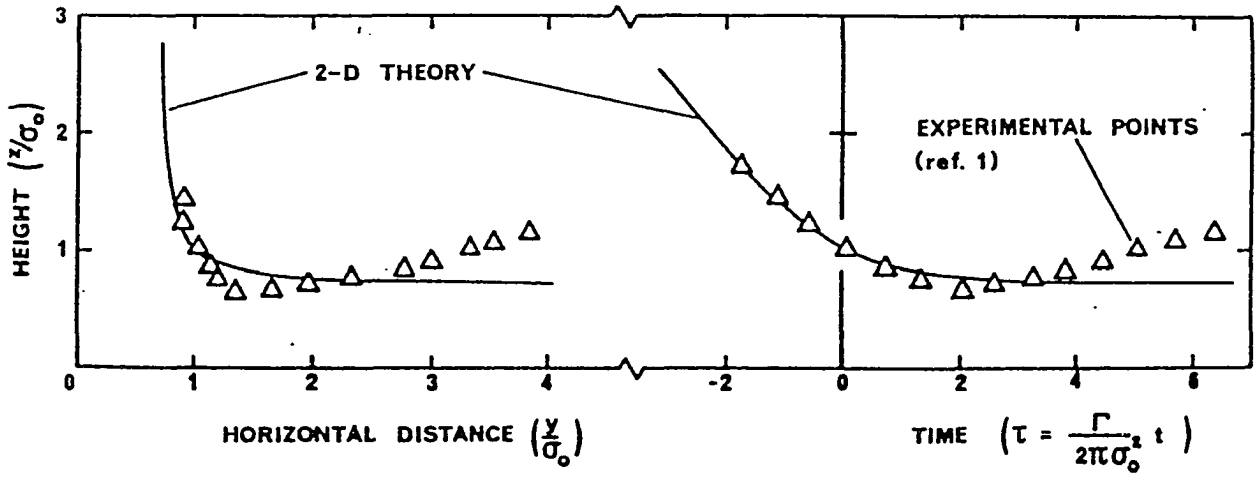

Figure 2.2 Comparison between two-dimensional, potential theory prediction and flight experimental data of Dee and Nicholas (1968) for vortex path, excerpted from Harvey and Perry's (1971) Figure 1.

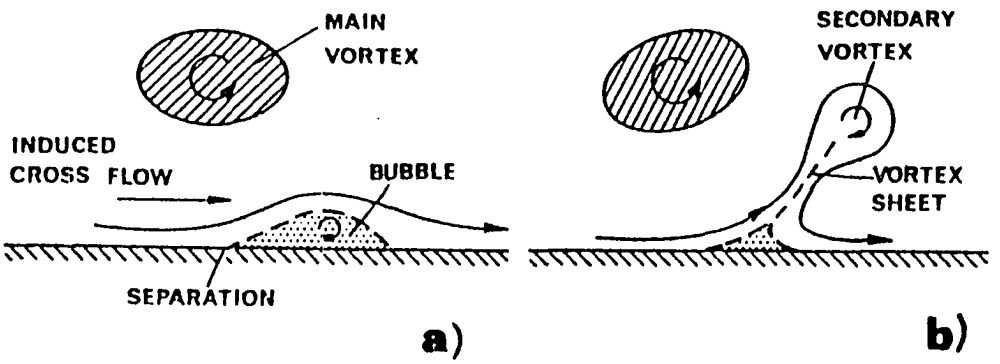

Figure 2.3 Suggested interpretation of vortex rebound caused by ground booundary layer separation by Harvey and Perry (1971): (a) a section downstream of the initial separation, (b) the subsequent development of the secondary vortex

Chapter 3 Derivation of Governing Equations

In this chapter, starting from the full, unsteady, three-dimensional, compressible Navier-Stokes equations, a set of governing equations is derived for wake vortex systems in ground effect. In order to consider atmospheric influences, such as stratification and crosswind, temperature and density effects must be included in the governing equations. Two types of flows — the atmosphere and the wake vortex system — must be considered simultaneously. The appropriate governing equations of motion can be simplified by properly establishing order of magnitude estimates of each term in the various general governing equations. Beginning by establishing characteristic scales for atmospheric processes, limits can be placed on the scales that represent aircraft wakes in ground effect. In Section 3.2, the conservation laws will be discussed using Boussinesq approximations, which will enable the compressible equations of motion to be approximated by modified incompressible equations. Then the equations will be reduced to two-dimensional flow cases for the vortex wake problem in Section 3.3. The modeled turbulent form of the equations will be discussed employing Donaldson's Reynolds-stress-transport model (1972a, 1973) in Section 3.4. The dimensionless form of the equations will be introduced in Section 3.5. A coordinate system employed in this study is shown in Figure 3.1.

It has been noted that many researchers attempted to provide a rigorous derivation of Boussinesq equations. The reader is referred to the works of Spiegel and Veronis (1960), Mihaljan (1962) and Dutton and Fichtl (1969), who were concerned with atmospheric

processes. None of them were able to come up with a mathematically rigorous justification in terms of asymptotic expansion developments. While *ad hoc* assumptions were unavoidably employed in their derivations, their assumptions were concerned exclusively with atmospheric flows. Since aircraft vortex dynamics is the goal of this research, the following discussion tries to establish a set of dynamic equations for a representative aircraft vortex system, treating atmosphere as an ambient flow. Therefore, the discussion is based on the scales of a typical large aircraft vortex system to justify the applicability of the Boussinesq approximations for the present problem. This development, to the author's knowledge, is original.

3.1 Atmospheric Flow Conditions

Following Donaldson (1973), the vertical atmospheric length scale, L_∞, can be represented in terms of the nominal atmospheric density gradient. The length scale, L_∞, is thus be defined as

$$L_\infty = \frac{1}{\rho_\infty} \frac{d\rho_\infty}{dy} \tag{3.1}$$

where $\rho_\infty(y)$ is the nominal atmospheric density at altitude y. Using the U. S. Standard Atmosphere (1962), L_∞ is on the order of 10^4 m in the lower atmosphere. Plate (1971) has discussed the importance of Coriolis acceleration effects on atmospheric processes. However, if it is recognized that the region in which wake vortices interact simultaneously with the atmosphere and the ground is only a few hundred meters, Coriolis acceleration terms are found to be four orders of magnitude smaller than gravitational acceleration and vortex inertial terms, even for crosswind velocities of up to 15m/s. (Higher crosswind velocities produce turbulent fluctuations which are comparable in magnitude to wake

vortex effects, making wake-vortex forecasting requirements less important.) Hence, Coriolis effects can be neglected in the domain of interest.

Using the lapse rate (dT_∞/dy, where T_∞ is the nominal ambient temperature distribution) to characterize buoyancy effects, it can be assumed that the maximum sustainable lapse rate is less than 20 °C in 100 m (the average standard atmosphere gradient is about 6.51 °C/km and local gradients as high as 0.5 °C/m have been recorded, but over very small regions) so that

$$\frac{dT_\infty}{dy} < 0.2°C/m\,, \tag{3.2}$$

with respect to buoyancy induced flow effects. Furthermore, it is assumed that the ambient surface temperature $T_\infty(0)$ is within the interval $230K \leq T_\infty(0) \leq 320K$. Under these temperature extremes, variation in thermophysical properties (μ and k) are less than 10 percent within the wake vortex domain.

Treating air as an ideal gas, the stratified ambient conditions (p_∞, ρ_∞, T_∞) can be related to an assumed lapse rate. It is noted that, unlike meteorological studies, detailed flow field modeling of the background atmosphere is not attempted. The flow field of interest is the vortex system, interacting with certain assumed atmospheric conditions. The time scale of the vortex motion is very small compared to atmospheric response time. Therefore, the ambient atmosphere is assumed in a steady-state when vortex wakes have not appeared and the equilibrium of the atmosphere has already been established. Its significant motion can be approximated by cross-flow velocities $U = U(y)\,, V = W = 0$. If $T_\infty(y)$ is given by

$$T_\infty(y) = T_o + \beta y\,, \tag{3.3}$$

where β is the (prescribed) lapse rate, conservation of momentum and energy for constant thermophysical properties, with the specified cross-flow, simplify to

$$\frac{dp_\infty}{dy} = -\rho_\infty(y)g \tag{3.4}$$

and

$$\frac{d^2T_\infty}{dy^2} = 0\,, \tag{3.5}$$

respectively. Hence, the ambient density and pressure distribution are given by

$$\rho_\infty(y) = \rho_o\left[\frac{T_\infty(y)}{T_o}\right]^{-g/R\beta+1} \tag{3.6}$$

and

$$p_\infty(y) = p_o\left[\frac{T_\infty(y)}{T_o}\right]^{-g/R\beta}\,, \tag{3.7}$$

where R is the gas constant for air and ρ_o and p_o are the (prescribed) ambient density and pressure at the surface. If it is assumed that $(\beta y/T_o)_{max} = 20/230$, i.e. temperature varies by less than ten percent through the anticipated computational domain, then a simple calculation using Eqn. (3.6) and (3.7) can show that density varies by less than ten percent and pressure varies by less than 2%.

3.2 Conservation Equations for Wake Vortex System in Ground Effect

If a Boeing 747 is considered as the current upper limit on vortex wake scales, the appropriate length scale is on the order of the wing span and using terminal flight conditions for reference, the velocity and lift can be used to estimate characteristic vortex velocities, Γ/s, where Γ is the circulation and s is the aircraft half-span. Typical vortex velocities are therefore on the order of 5m/s (Burhnam, *et al*, 1978), which yields a Mach

number on the order of 10^{-2}, justifying the neglect of mechanical compressibility effects. However, compressibility must still be considered with respect to stratification.

Treating air as an ideal gas, the thermodynamic variables are further considered in terms of their departure from their ambient distributions. That is, take

$$\begin{aligned} \rho(x,y,z,t) &= \rho_\infty(y) + \Delta\rho(x,y,z,t)\,, \\ p(x,y,z,t) &= p_\infty(y) + \Delta p(x,y,z,t)\,, \\ T(x,y,z,t) &= T_\infty(y) + \Delta T(x,y,z,t)\,, \end{aligned} \tag{3.8}$$

with

$$p = \rho R T\,. \tag{3.9}$$

It can be seen that

$$p_\infty = \rho_\infty R T_\infty \tag{3.10}$$

and

$$\frac{\Delta p}{p_\infty} = \frac{\Delta\rho}{\rho_\infty} + \frac{\Delta T}{T_\infty} + \frac{\Delta\rho}{\rho_\infty}\frac{\Delta T}{T_\infty}\,. \tag{3.11}$$

The dimensionless thermodynamic departure variables are defined as

$$\begin{aligned} \widetilde{\rho} &\equiv \Delta\rho/\rho_\infty\,, \\ \widetilde{p} &\equiv \Delta p/p_\infty\,, \end{aligned}$$

and

$$\widetilde{T} \equiv \Delta T/T_\infty\,.$$

3.2.1 Conservation of Mass

The continuity equation

$$\frac{D\rho}{Dt} + \rho\frac{\partial u_j}{\partial x_j} = 0 \tag{3.14}$$

can be rewritten, using the steady-state ambient density distribution and thermodynamic departure variables, as

$$\frac{D\widetilde{\rho}}{Dt} + (1+\widetilde{\rho})\left[u_2\frac{d(ln\rho_\infty)}{dy} + \frac{\partial u_j}{\partial x_j}\right] = 0\,. \tag{3.15}$$

Furthermore, the maximum stratification case yields $d(ln\rho_\infty)/dy < 0.001$, justifying the neglect of the logarithmic density transport term, so that

$$\frac{\partial u_j}{\partial x_j} \simeq -\frac{1}{1+\widetilde{\rho}}\frac{D\widetilde{\rho}}{Dt}\,. \tag{3.16}$$

To go further, estimates of the vortex-induced flow quantities must be introduced. Beginning by assuming that $\widetilde{\rho}$, $\widetilde{p}$ and $\widetilde{T}$ are much less than unity, product terms can then be dropped in Eqn. (3.11), leaving

$$\widetilde{p} = \widetilde{\rho} + \widetilde{T}\,. \tag{3.17}$$

Furthermore, pressure departure can only be on the order of the dynamic pressure so that

$$|\widetilde{p}| \leq \frac{\rho u_j^2}{2p_\infty} = \frac{u_j^2}{2RT_\infty} = \frac{1}{2}\gamma M^2\,. \tag{3.18}$$

We have already determined that $M \ll 1$, justifying the approximation

$$\widetilde{\rho} + \widetilde{T} = 0\,, \tag{3.19}$$

so the conservation of mass can be written as

$$\frac{\partial u_j}{\partial x_j} = \frac{D\widetilde{T}}{Dt} . \tag{3.20}$$

A fact is also noted from Eqn. (3.19) that compared with $\widetilde{\rho}$ and $\widetilde{T}$, $\widetilde{p}$ is more than an order of magnitude smaller.

At this point it is necessary to estimate the physical orders of magnitude of the terms in Eqn. (3.20). This can be pursued by comparing the velocity gradient terms with the rates of temperature change, which include the changes due to both convection and local unsteadiness.

Using the estimated characteristic vortex velocity, it is likely that the vertical velocity component (v) will vary from zero (at the ground plane) to Γ/s in one half-span (s). Hence,

$$\frac{\partial v}{\partial y} = O\left(\Gamma/s^2\right) \approx O(0.1/sec) \tag{3.21}$$

for the Boeing 747 case. The most extreme temperature departure is on the order of the total ambient change and, assuming a vertical convection speed of Γ/s, over a required distance of $2s$ (to achieve a maximum time rate of change of particle temperature), the order of magnitude of the temperature derivative, due to velocity convection, is estimated to be

$$\frac{D\widetilde{T}}{Dt} = O\left[\frac{\Gamma}{s}\left(\frac{\beta y}{T_o}\right)_{max}\frac{1}{2s}\right] = O\left(10^{-3}/sec\right) . \tag{3.22}$$

Hence, the velocity gradient terms are nearly two orders of magnitude larger than the rates of change of the temperature departure (due to convection) so that, if local unsteadiness is not considered (no high frequency heat sources), enforcing conservation of mass as

$$\frac{\partial u_j}{\partial x_j} = 0 , \tag{3.23}$$

is accurate to within two orders of magnitude. It is noted that Gebhart (1973) used an order of magnitude comparison approach to reach the same conclusion for a generalized three-dimensional atmospheric flow.

3.2.2 Conservation of Momentum

The momentum equation for compressible flows

$$\rho\frac{Du_i}{Dt} = -\frac{\partial p}{\partial x_i} + \mu\frac{\partial}{\partial x_j}\left(\frac{\partial u_i}{\partial x_j} + \frac{\partial u_j}{\partial x_i}\right) + \delta_{ij}\frac{\partial}{\partial x_j}\left(\mu^*\frac{\partial u_m}{\partial x_m}\right) + \rho g_i \,, \tag{3.24}$$

after invoking the continuity equation Eqn. (3.23) and the expansion of Eqn. (3.8), becomes

$$(\rho_\infty + \Delta\rho)\frac{Du_i}{Dt} = -\frac{\partial(p_\infty)}{\partial x_i} - \frac{\partial(\Delta p)}{\partial x_i} + \mu\frac{\partial^2 u_i}{\partial x_j \partial x_j} + \rho_\infty g_i + \Delta\rho g_i \,. \tag{3.25}$$

Dividing the equation by ρ_∞ and utilizing the ambient state Eqn. (3.4), along with the fact that $\widetilde{\rho} \ll 1$, the following expression is obtained:

$$\frac{Du_i}{Dt} = -\frac{1}{\rho_\infty}\frac{\partial(\Delta p)}{\partial x_i} + \frac{\mu}{\rho_\infty}\frac{\partial^2 u_i}{\partial x_j \partial x_j} + \widetilde{\rho} g_i \,. \tag{3.26}$$

This equation shows that density variation effects can be neglected in the momentum equations except for the body force term. This fact is sometimes called the Boussinesq hypothesis (Turner, 1973). The extra body force term in this equation, compared with the incompressible momentum equations, is the only term in the dynamic equations where the density variation effects are included. Later in Section 3.2, it will shown that in the vorticity transport equation, this term will create vorticity due to density departure.

3.2.3 Conservation of Energy

The energy conservation equation can be written:

$$\rho c_p \frac{DT}{Dt} = \frac{Dp}{Dt} + k\frac{\partial^2 T}{\partial x_j \partial x_j} + \mu\left(\frac{\partial u_i}{\partial x_j} + \frac{\partial u_j}{\partial x_i}\right)\frac{\partial u_i}{\partial x_j} \tag{3.27}$$

where the solenoidal velocity field Eqn. (3.23) has already been used to neglect the bulk viscous effects. Moreover, The last term in Eqn. (3.27), the energy dissipation term, describes the heating of the medium caused by the internal friction of the vortex motion. This heating plays a completely insignificant role in changing the temperature field of high Reynolds number and low Mach number flows, since it is on the order of M^2/Re, compared with the other terms in Eqn. (3.27). Thus, the following equation is obtained, with Eqn. (3.8),

$$(\rho_\infty + \Delta\rho)c_p\left(u_j\frac{\partial T_\infty}{\partial x_j} + \frac{D(\Delta T)}{Dt}\right) = \left(u_j\frac{\partial p_\infty}{\partial x_j} + \frac{D(\Delta p)}{Dt}\right) + k\frac{\partial^2(\Delta T)}{\partial x_j \partial x_j}, \tag{3.28}$$

and it can be rewritten as

$$(1+\widetilde{\rho})c_p\left[u_j\frac{\partial T_\infty}{\partial x_j}\left(1+\widetilde{T}\right) + T_\infty\frac{D\widetilde{T}}{Dt}\right] = \frac{u_j}{\rho_\infty}\frac{\partial p_\infty}{\partial x_j}(1+\widetilde{p}) + RT_\infty\frac{D\widetilde{p}}{Dt} + \frac{k}{\rho_\infty}\frac{\partial^2(\Delta T)}{\partial x_j \partial x_j}. \tag{3.29}$$

Since all the "tilde" terms are much smaller than unity, and neglecting the second order terms and terms with $\widetilde{p}$ compared with $\widetilde{T}$, the following approximate equation is justified:

$$\frac{D\widetilde{T}}{Dt} = \frac{u_j}{T_\infty}\left(\frac{1}{\rho_\infty c_p}\frac{\partial p_\infty}{\partial x_j} - \frac{\partial T_\infty}{\partial x_j}\right) + \frac{k}{\rho_\infty T_\infty c_p}\frac{\partial^2(\Delta T)}{\partial x_j \partial x_j}. \tag{3.30}$$

Then, making use of the nominal state relations Eqns. (3.3) and (3.4),

$$\frac{D\widetilde{T}}{Dt} = \frac{u_2}{T_\infty}\left(\frac{g}{c_p} - \beta\right) + \frac{k}{\rho_\infty T_\infty c_p}\frac{\partial^2(\Delta T)}{\partial x_j \partial x_j} \tag{3.31}$$

is obtained. In this equation, g/c_p represents the adiabatic lapse rate for air in neutral equilibrium (Plate, 1971), which is about 0.001 °C/m and can thus be neglected in comparison with β. The diffusion term can also be neglected for high Reynolds number flows except near the ground boundary. However, since the time required for the atmosphere to establish an equilibrium thermal boundary layer is much longer than the characteristic time of the vortex motion, dynamic thermal boundary layer effects can be ignored in terms of their influence on unsteady temperature departure-driven vortex dynamics. Hence, the approximate conservation of energy equation finally becomes

$$\frac{D\widetilde{T}}{Dt} = -\beta \frac{u_2}{T_\infty} . \tag{3.32}$$

It can be shown, from 3.1.1, that this equation can also be treated as a higher order representation of the conservation of mass.

To further simplify Eqns. (3.26) and (3.32), it has been noted that the background thermodynamic variables, ρ_∞, p_∞, T_∞, which are functions of the vertical distance from the ground, have appeared in Eqns. (3.26) and (3.32) as coefficients of certain terms. From Eqns (3.3), (3.6) and (3.7), it can be assumed that within the altitude range of ground-coupled vortex motion, these coefficients can be treated as constants to first order accuracy. That is, $\rho_\infty \approx \rho_o$, $p_\infty \approx p_o$ and $T_\infty \approx T_o$ have been assumed. Then the momentum and energy conservation equations, Eqns. (3.26) and (3.32), become

$$\frac{Du_i}{Dt} = -\frac{p_o}{\rho_o}\frac{\partial \widetilde{p}}{\partial x_i} + \nu_o \frac{\partial^2 u_i}{\partial x_j \partial x_j} + \widetilde{\rho} g_i , \tag{3.33}$$

where ν_o is the kinematic viscosity, and

$$\frac{D\widetilde{\rho}}{Dt} = \beta \frac{u_2}{T_o} , \tag{3.34}$$

respectively. In obtaining Eqn. (3.34), the relation between temperature departure and density departure in Boussinesq approximation, Eqn. (3.19), has been used.

Eqns. (3.23), (3.33) and (3.34) have been used to formulate the governing equations for both laminar and turbulent vortex wakes in a stratified atmosphere. If the stratification effects are not considered, only Eqns. (3.23) and (3.33) are needed to calculate the vortex motion, since the body force term is dropped in Eqn. (3.33), leaving the dynamic equations for incompressible flows.

3.3 Reduction to Two-Dimensional Cases

The coordinate system is shown in Figure 3.1, where the positive z-direction is perpendicular outward from the plane of the paper and is assumed to be parallel with the vortex rotational axes. Hence, x_1, x_2 and x_3 correspond to x, y and z, respectively. The coordinate system is fixed with respect to the ground and a section at a specified z is considered.

The near field structure of an aircraft wake vortex system is quite complex and is influenced by the actual aircraft geometry, including trim and speed. While some progress has been made in predicting near field vortex behavior (see Wong, Kandil and Liu, 1992, for example), the work presented here is restricted to the far field. That is, it is assumed that the vortex system has evolved into a prescribed vortex pair, of known strength and spacing.

In vortex hazard problems, only vortex wakes in the far field from the aircraft are studied, where the changes in the flow field in the vortex axial (z) direction are small

compared with changes in the plane of the vortex. So it can be assumed that

$$\frac{\partial}{\partial z} \ll \frac{\partial}{\partial x}, \frac{\partial}{\partial z} \ll \frac{\partial}{\partial y}. \tag{3.35}$$

With these assumptions, Eqns. (3.23), (3.33) and (3.34) can be written as

$$\frac{\partial u}{\partial x} + \frac{\partial v}{\partial y} = 0, \tag{3.36}$$

$$\frac{\partial u}{\partial t} + u\frac{\partial u}{\partial x} + v\frac{\partial u}{\partial y} = -\frac{p_o}{\rho_o}\frac{\partial \widetilde{p}}{\partial x} + \nu_o\left(\frac{\partial^2 u}{\partial x^2} + \frac{\partial^2 u}{\partial y^2}\right), \tag{3.37}$$

$$\frac{\partial v}{\partial t} + u\frac{\partial v}{\partial x} + v\frac{\partial v}{\partial y} = -\frac{p_o}{\rho_o}\frac{\partial \widetilde{p}}{\partial y} + \nu_o\left(\frac{\partial^2 v}{\partial x^2} + \frac{\partial^2 v}{\partial y^2}\right) - \widetilde{\rho} g, \tag{3.38}$$

$$\frac{\partial w}{\partial t} + u\frac{\partial w}{\partial x} + v\frac{\partial w}{\partial y} = \nu_o\left(\frac{\partial^2 w}{\partial x^2} + \frac{\partial^2 w}{\partial y^2}\right), \tag{3.39}$$

and

$$\frac{\partial \widetilde{\rho}}{\partial t} + u\frac{\partial \widetilde{\rho}}{\partial x} + v\frac{\partial \widetilde{\rho}}{\partial y} = v\beta. \tag{3.40}$$

It can be seen that with the quasi-two-dimensional assumptions, Eqn. (3.35), the z-component of the conservation of momentum equation, Eqn. (3.39), is independent from the other two-dimensional equations. Since only the flows in the swirling velocity plane are of interest in the present study, Eqn. (3.39) can be omitted for the purposes of calculating velocities in the x-y plane for both laminar and time-averaged turbulent flows. That is, a fully two-dimensional assumption is made, setting the axial velocity component equal to zero or a constant, i.e. by assuming that both sides of Eqn. (3.39) are identically zero.

In unsteady, two-dimensional, incompressible flows, vorticity-streamfunction formulations can be employed. Furthermore, the vorticity field in this problem is a major variable of interest. Taking the cross-product of Eqns. (3.37) and (3.38), the vorticity transport equation is obtained:

$$\frac{D\zeta}{Dt} = \nu_o \nabla^2 \zeta - g\frac{\partial \widetilde{\rho}}{\partial x}\,, \tag{3.41}$$

where

$$\zeta = \frac{\partial v}{\partial x} - \frac{\partial u}{\partial y}\,. \tag{3.42}$$

From the incompressibility condition Eqn. (3.36), the streamfunction equation,

$$\nabla^2 \psi = -\zeta\,, \tag{3.43}$$

applies, where

$$u = \frac{\partial \psi}{\partial y}, \quad \text{and} \quad v = -\frac{\partial \psi}{\partial x}\,. \tag{3.44}$$

Eqns. (3.40), (3.41) and (3.43) are the set of equations required to simulate laminar vortex flows with stratification effects.

The boundary conditions for the cases without cross-flow effects are specified as

$$\zeta(0,y,t) = 0\,,\ \psi(0,y,t) = 0\,,\ \frac{\partial \widetilde{\rho}}{\partial x}(0,y,t) = 0\,, \tag{3.45}$$

$$\zeta(\infty,y,t) = 0\,,\ \psi(\infty,y,t) = 0\,,\ \widetilde{\rho}(\infty,y,t) = 0\,, \tag{3.46}$$

$$\zeta(x,0,t) = -\frac{\partial^2 \psi}{\partial y^2}(x,0,t)\,,\ \psi(x,0,t) = 0\,,\ \widetilde{\rho}(x,0,t) = 0\,, \tag{3.47}$$

and

$$\zeta(x,\infty,t)=0\,,\ \psi(x,\infty,t)=0\,,\ \widetilde{\rho}(x,\infty,t)=0\,. \tag{3.48}$$

The cross-flow boundary conditions will be discussed in Chapter 9.

3.4 Two-Dimensional, Stratified Turbulent Flows

In this section, equations for turbulent vortex flows have been derived based on Eqns. (3.36)-(3.40), where the velocity field is decomposed as:

$$u_i = U_i + u_i' \tag{3.49}$$

and the thermodynamic departure variables can be decomposed by assuming the departure variables represent unsteady mean and fluctuating flows, i.e. $\widetilde{(\ )}$ is replaced by $\widetilde{(\ )}$ + $(\ )'$, where the tilde variables are assumed to be unsteady solutions to the time averaged turbulent equations. For simplicity, in the following the prime for the fluctuation variables is omitted. Substituting the decompositions into Eqns. (3.36)-(3.40) and taking time averages, the following equations are gotten:

For the mean flow variables:

$$\frac{\partial U}{\partial x}+\frac{\partial V}{\partial y}=0 \tag{3.50}$$

$$\frac{\partial U}{\partial t}+U\frac{\partial U}{\partial x}+V\frac{\partial U}{\partial y}=-\frac{p_o}{\rho_o}\frac{\partial \widetilde{p}}{\partial x}+\nu_o\left(\frac{\partial^2 U}{\partial x^2}+\frac{\partial^2 U}{\partial y^2}\right)-\frac{\partial \overline{u^2}}{\partial x}-\frac{\partial \overline{uv}}{\partial y} \tag{3.51}$$

$$\frac{\partial V}{\partial t}+U\frac{\partial V}{\partial x}+V\frac{\partial V}{\partial y}=-\frac{p_o}{\rho_o}\frac{\partial \widetilde{p}}{\partial y}+\nu_o\left(\frac{\partial^2 V}{\partial x^2}+\frac{\partial^2 V}{\partial y^2}\right)-\rho g-\frac{\partial \overline{uv}}{\partial x}-\frac{\partial \overline{v^2}}{\partial y} \tag{3.52}$$

$$\frac{\partial \widetilde{\rho}}{\partial t} + u\frac{\partial \widetilde{\rho}}{\partial x} + v\frac{\partial \widetilde{\rho}}{\partial y} = -v\beta - \frac{\partial \overline{\rho u}}{\partial x} - \frac{\partial \overline{\rho v}}{\partial y} \,. \tag{3.53}$$

For the fluctuation field:

$$\frac{D\overline{u^2}}{Dt} = -2\left(\overline{u^2}\frac{\partial U}{\partial x} + \overline{uv}\frac{\partial U}{\partial y}\right) - \frac{\partial \overline{u^3}}{\partial x} - \frac{\partial \overline{u^2 v}}{\partial y} - 2\frac{p_o}{\rho_o}\frac{\partial \overline{pu}}{\partial x} + 2\frac{p_o}{\rho_o}\overline{p\frac{\partial u}{\partial x}}$$
$$+\nu_o\left(\frac{\partial^2 \overline{u^2}}{\partial x^2} + \frac{\partial^2 \overline{u^2}}{\partial y^2}\right) - 2\nu_o\left(\overline{\frac{\partial u}{\partial x}\frac{\partial u}{\partial x}} + \overline{\frac{\partial u}{\partial y}\frac{\partial u}{\partial y}} + \overline{\frac{\partial u}{\partial z}\frac{\partial u}{\partial z}}\right) \,, \tag{3.54}$$

$$\frac{D\overline{v^2}}{Dt} = -2\left(\overline{uv}\frac{\partial V}{\partial x} + \overline{v^2}\frac{\partial V}{\partial y}\right) - \frac{\partial \overline{uv^2}}{\partial x} - \frac{\partial \overline{v^3}}{\partial y} - 2\frac{p_o}{\rho_o}\frac{\partial \overline{pv}}{\partial y} + 2\frac{p_o}{\rho_o}\overline{p\frac{\partial v}{\partial y}}$$
$$+\nu_o\left(\frac{\partial^2 \overline{v^2}}{\partial x^2} + \frac{\partial^2 \overline{v^2}}{\partial y^2}\right) - 2\nu_o\left(\overline{\frac{\partial v}{\partial x}\frac{\partial v}{\partial x}} + \overline{\frac{\partial v}{\partial y}\frac{\partial v}{\partial y}} + \overline{\frac{\partial v}{\partial z}\frac{\partial v}{\partial z}}\right) - 2g\overline{\rho v} \,, \tag{3.55}$$

$$\frac{D\overline{w^2}}{Dt} = -2\left(\overline{uw}\frac{\partial W}{\partial x} + \overline{vw}\frac{\partial W}{\partial y}\right) - \frac{\partial \overline{uw^2}}{\partial x} - \frac{\partial \overline{vw^2}}{\partial y} + 2\frac{p_o}{\rho_o}\overline{p\frac{\partial w}{\partial z}}$$
$$+\nu_o\left(\frac{\partial^2 \overline{w^2}}{\partial x^2} + \frac{\partial^2 \overline{w^2}}{\partial y^2}\right) - 2\nu_o\left(\overline{\frac{\partial w}{\partial x}\frac{\partial w}{\partial x}} + \overline{\frac{\partial w}{\partial y}\frac{\partial w}{\partial y}} + \overline{\frac{\partial w}{\partial z}\frac{\partial w}{\partial z}}\right) \,, \tag{3.56}$$

$$\frac{D\overline{uv}}{Dt} = -\left(\overline{u^2}\frac{\partial V}{\partial x} + \overline{v^2}\frac{\partial U}{\partial y}\right) - \frac{\partial \overline{u^2 v}}{\partial x} - \frac{\partial \overline{uv^2}}{\partial y} - \frac{p_o}{\rho_o}\left(\frac{\partial \overline{pu}}{\partial y} + \frac{\partial \overline{pv}}{\partial x}\right) + \frac{p_o}{\rho_o}\overline{p\left(\frac{\partial u}{\partial y} + \frac{\partial v}{\partial x}\right)}$$
$$+\nu_o\left(\frac{\partial^2 \overline{uv}}{\partial x^2} + \frac{\partial^2 \overline{uv}}{\partial y^2}\right) - 2\nu_o\left(\overline{\frac{\partial u}{\partial x}\frac{\partial v}{\partial x}} + \overline{\frac{\partial u}{\partial y}\frac{\partial v}{\partial y}} + \overline{\frac{\partial u}{\partial z}\frac{\partial v}{\partial z}}\right) - g\overline{\rho u} \,, \tag{3.57}$$

$$\frac{D\overline{uw}}{Dt} = -\left(\overline{uw}\frac{\partial U}{\partial x} + \overline{vw}\frac{\partial U}{\partial y}\right) - \frac{\partial \overline{u^2 w}}{\partial x} - \frac{\partial \overline{uvw}}{\partial y} - \frac{p_o}{\rho_o}\frac{\partial \overline{pw}}{\partial x} + \frac{p_o}{\rho_o}\overline{p\left(\frac{\partial u}{\partial z} + \frac{\partial w}{\partial x}\right)}$$
$$+\nu_o\left(\frac{\partial^2 \overline{uw}}{\partial x^2} + \frac{\partial^2 \overline{uw}}{\partial y^2}\right) - 2\nu_o\left(\overline{\frac{\partial u}{\partial x}\frac{\partial w}{\partial x}} + \overline{\frac{\partial u}{\partial y}\frac{\partial w}{\partial y}} + \overline{\frac{\partial u}{\partial z}\frac{\partial w}{\partial z}}\right) \,, \tag{3.58}$$

$$\frac{D\overline{wv}}{Dt} = -\left(\overline{uw}\frac{\partial V}{\partial x} + \overline{vw}\frac{\partial V}{\partial y}\right) - \frac{\partial \overline{uvw}}{\partial x} - \frac{\partial \overline{v^2 w}}{\partial y} - \frac{p_o}{\rho_o}\frac{\partial \overline{pw}}{\partial y} + \frac{p_o}{\rho_o}\overline{p\left(\frac{\partial v}{\partial z} + \frac{\partial w}{\partial x}\right)}$$
$$+\nu_o\left(\frac{\partial^2 \overline{vw}}{\partial x^2} + \frac{\partial^2 \overline{vw}}{\partial y^2}\right) - 2\nu_o\left(\overline{\frac{\partial v}{\partial x}\frac{\partial w}{\partial x}} + \overline{\frac{\partial v}{\partial y}\frac{\partial w}{\partial y}} + \overline{\frac{\partial v}{\partial z}\frac{\partial w}{\partial z}}\right) - g\overline{\rho w} \quad , \tag{3.59}$$

$$\frac{D\overline{\rho^2}}{Dt} = -2\overline{\rho u}\frac{\partial \widetilde{\rho}}{\partial x} - 2\overline{\rho v}\left(\beta + \frac{\partial \widetilde{\rho}}{\partial y}\right) - \frac{\partial \overline{\rho^2 u}}{\partial x} - \frac{\partial \overline{\rho^2 v}}{\partial y} \quad , \tag{3.60}$$

$$\frac{D\overline{\rho u}}{Dt} = -\overline{u^2}\frac{\partial \widetilde{\rho}}{\partial x} - \overline{uv}\left(\beta + \frac{\partial \widetilde{\rho}}{\partial y}\right) - \overline{\rho u}\frac{\partial U}{\partial x} - \overline{\rho v}\frac{\partial U}{\partial y} - \frac{\partial \overline{\rho u^2}}{\partial x} - \frac{\partial \overline{\rho uv}}{\partial y}$$
$$-\frac{p_o}{\rho_o}\frac{\partial \overline{\rho p}}{\partial x} + \frac{p_o}{\rho_o}\overline{p\frac{\partial \rho}{\partial x}} - \nu_o\rho\overline{\left(\frac{\partial^2 u}{\partial x^2} + \frac{\partial^2 u}{\partial y^2}\right)} \quad , \tag{3.61}$$

$$\frac{D\overline{\rho v}}{Dt} = -\overline{uv}\frac{\partial \widetilde{\rho}}{\partial x} - \overline{v^2}\left(\beta + \frac{\partial \widetilde{\rho}}{\partial y}\right) - \overline{\rho u}\frac{\partial V}{\partial x} - \overline{\rho v}\frac{\partial V}{\partial y} - \frac{\partial \overline{\rho uv}}{\partial x} - \frac{\partial \overline{\rho v^2}}{\partial y} - g\overline{\rho^2}$$
$$-\frac{p_o}{\rho_o}\frac{\partial \overline{\rho p}}{\partial y} + \frac{p_o}{\rho_o}\overline{p\frac{\partial \rho}{\partial y}} - \nu_o\rho\overline{\left(\frac{\partial^2 v}{\partial x^2} + \frac{\partial^2 v}{\partial y^2}\right)} \quad , \tag{3.62}$$

and

$$\frac{D\overline{\rho w}}{Dt} = -\overline{uw}\frac{\partial \widetilde{\rho}}{\partial x} - \overline{vw}\left(\beta + \frac{\partial \widetilde{\rho}}{\partial y}\right) - \overline{\rho u}\frac{\partial W}{\partial x} - \overline{\rho v}\frac{\partial W}{\partial y} - \frac{\partial \overline{\rho uw}}{\partial x} - \frac{\partial \overline{\rho vw}}{\partial y}$$
$$+\frac{p_o}{\rho_o}\overline{p\frac{\partial \rho}{\partial z}} - \nu_o\rho\overline{\left(\frac{\partial^2 w}{\partial x^2} + \frac{\partial^2 w}{\partial y^2}\right)} \quad . \tag{3.63}$$

Careful examination of Eqns. (3.58), (3.59) and (3.63) suggests that if it can be assumed that initially all the turbulent Reynolds shear stresses and all the density-velocity correlations are zero (or arbitrarily small), the source terms in those equations are not operational at first. If the source terms subjected to the interactions between the axial

velocity gradients and the density-velocity correlations in Eqn. (3.63) can be neglected, the influence of $\overline{uw}$, $\overline{vw}$ and $\overline{\rho w}$ on the mean flow variables can be neglected in comparison with the influence from the other Reynolds stresses and density-velocity correlations, since they have no significant source terms in their equations at any time. Here, neglect of the z-component velocity correlations is assumed to be a reasonable approximation for the two-dimensional study.

Using the same argument as in Section 3.1 that the diffusion effects can be neglected in the density departure equation, all the diffusion terms in the equations for density-velocity correlation can be neglected. Then following the Reynolds-stress-transport model suggested by Donaldson (see Donaldson 1972a, 1973 and Lewellen, Teske and Donaldson, 1976), the following modeled equations are obtained for the fluctuation field:

$$\frac{D\overline{u^2}}{Dt} = -2\left(\overline{u^2}\frac{\partial U}{\partial x} + \overline{uv}\frac{\partial U}{\partial y}\right) + \frac{\partial}{\partial x}\left(3Q_1\frac{\partial \overline{u^2}}{\partial x}\right) + \frac{\partial}{\partial y}\left[Q_I\left(2\frac{\partial \overline{uv}}{\partial x} + \frac{\partial \overline{u^2}}{\partial y}\right)\right]$$
$$+2\frac{p_o}{\rho_o}\frac{\partial}{\partial x}\left[Q_{II}\left(\frac{\partial \overline{u^2}}{\partial x}\right)\right] - \frac{q}{\Lambda}\frac{2\overline{u^2} - \overline{v^2} - \overline{w^2}}{3}$$
$$+\nu_o\left(\frac{\partial^2 \overline{u^2}}{\partial x^2} + \frac{\partial^2 \overline{u^2}}{\partial y^2}\right) - 2\nu_o a\frac{\overline{u^2}}{\Lambda^2} - \frac{2bq}{\Lambda}\left(\alpha\overline{u^2} + \frac{1-\alpha}{2}q^2\right) , \qquad (3.64)$$

$$\frac{D\overline{v^2}}{Dt} = -2\left(\overline{uv}\frac{\partial V}{\partial x} + \overline{v^2}\frac{\partial V}{\partial y}\right) + \frac{\partial}{\partial x}\left[Q_I\left(2\frac{\partial \overline{uv}}{\partial y} + \frac{\partial \overline{v^2}}{\partial x}\right)\right] + \frac{\partial}{\partial y}\left(3Q_I\frac{\partial \overline{v^2}}{\partial y}\right)$$
$$-2\frac{p_o}{\rho_o}\frac{\partial}{\partial y}\left[Q_{II}\left(\frac{\partial \overline{uv}}{\partial x} + \frac{\partial \overline{v^2}}{\partial y}\right)\right] - \frac{q}{\Lambda}\frac{2\overline{v^2} - \overline{u^2} - \overline{w^2}}{3}$$
$$+\nu_o\left(\frac{\partial^2 \overline{v^2}}{\partial x^2} + \frac{\partial^2 \overline{v^2}}{\partial y^2}\right) - 2\nu_o a\frac{\overline{v^2}}{\Lambda^2} - \frac{2bq^2}{\Lambda}\left(\alpha\overline{v^2} + \frac{1-\alpha}{3}q^2\right) - 2g\overline{\rho v} , \qquad (3.65)$$

$$\frac{D\overline{w^2}}{Dt} = \frac{\partial}{\partial x}\left(Q_I\frac{\partial\overline{w^2}}{\partial x}\right) + \frac{\partial}{\partial y}\left(Q_I\frac{\partial\overline{w^2}}{\partial y}\right) - \frac{q}{\Lambda}\frac{2\overline{w^2} - \overline{u^2} - \overline{v^2}}{3}$$
$$+\nu_o\left(\frac{\partial^2\overline{w^2}}{\partial x^2} + \frac{\partial^2\overline{w^2}}{\partial y^2}\right) - 2\nu_o a\frac{\overline{w^2}}{\Lambda^2} - \frac{2bq}{\Lambda}\left(\alpha\overline{w^2} + \frac{1-\alpha}{3}q^2\right) , \qquad (3.66)$$

$$\frac{D\overline{uv}}{Dt} = -\left(\overline{u^2}\frac{\partial V}{\partial x} + \overline{v^2}\frac{\partial U}{\partial y}\right) + \frac{\partial}{\partial x}\left[Q_I\left(2\frac{\partial\overline{uv}}{\partial x} + \frac{\partial\overline{u^2}}{\partial y}\right)\right] + \frac{\partial}{\partial y}\left[Q_I\left(\frac{\partial\overline{v^2}}{\partial x} + 2\frac{\partial\overline{uv}}{\partial y}\right)\right]$$
$$+\frac{\partial}{\partial x}\left[Q_{II}\left(\frac{\partial\overline{uv}}{\partial x} + \frac{\partial\overline{v^2}}{\partial y}\right)\right] + \frac{\partial}{\partial y}\left[Q_{II}\left(\frac{\partial\overline{u^2}}{\partial x} + \frac{\partial\overline{uv}}{\partial y}\right)\right] - \frac{q}{\Lambda}\overline{uv}$$
$$+\nu_o\left(\frac{\partial^2\overline{uv}}{\partial x^2} + \frac{\partial^2\overline{uv}}{\partial y^2}\right) - 2\nu_o a\frac{\overline{uv}}{\Lambda^2} - \frac{2bq}{\Lambda}\alpha\overline{uv} - g\overline{\rho u} \quad , \qquad (3.67)$$

$$\frac{D\overline{\rho^2}}{Dt} = -2\overline{\rho u}\frac{\partial\widetilde{\rho}}{\partial x} - 2\overline{\rho v}\left(\beta + \frac{\partial\widetilde{\rho}}{\partial y}\right) + 3\left[\frac{\partial}{\partial x}\left(Q_I\frac{\partial\overline{\rho^2}}{\partial x}\right) + \frac{\partial}{\partial y}\left(Q_I\frac{\partial\overline{\rho^2}}{\partial y}\right)\right] - \frac{0.45q}{\Lambda}\overline{\rho^2} , \qquad (3.68)$$

$$\frac{D\overline{\rho u}}{Dt} = -\overline{u^2}\frac{\partial\widetilde{\rho}}{\partial x} - \overline{uv}\left(\beta + \frac{\partial\widetilde{\rho}}{\partial y}\right) - \overline{\rho u}\frac{\partial U}{\partial x} - \overline{\rho v}\frac{\partial U}{\partial y}$$
$$+3\left[\frac{\partial}{\partial x}\left(Q_I\frac{\partial\overline{\rho u}}{\partial x}\right) + \frac{\partial}{\partial y}\left(Q_I\frac{\partial\overline{\rho u}}{\partial y}\right)\right] - \frac{0.75q}{\Lambda}\overline{\rho u} , \qquad (3.69)$$

and

$$\frac{D\overline{\rho v}}{Dt} = -\overline{uv}\frac{\partial\widetilde{\rho}}{\partial x} - \overline{v^2}\left(\beta + \frac{\partial\widetilde{\rho}}{\partial y}\right) - \overline{\rho u}\frac{\partial V}{\partial x} - \overline{\rho v}\frac{\partial V}{\partial y}$$
$$+3\left[\frac{\partial}{\partial x}\left(Q_I\frac{\partial\overline{\rho v}}{\partial x}\right) + \frac{\partial}{\partial y}\left(Q_I\frac{\partial\overline{\rho v}}{\partial y}\right)\right] - \frac{0.75q}{\Lambda} - g\overline{\rho v} , \qquad (3.70)$$

where

$$Q_I = \Lambda_I q = \Lambda_I\left(\overline{u^2} + \overline{v^2} + \overline{w^2}\right)^{1/2} ,$$
$$Q_{II} = \Lambda_{II} q = \Lambda_{II}\left(\overline{u^2} + \overline{v^2} + \overline{w^2}\right)^{1/2} , \qquad (3.71)$$

and

$$\Lambda_I = \Lambda_{II} = 0.1\Lambda\,,$$

$$a = 3.25\,,\ b = 0.125\,,\ \alpha = 0\,, \tag{3.72}$$

and Λ is the turbulence length scale and q^2 is twice of the turbulent dynamic pressure or turbulent kinetic energy.

The vorticity-streamfunction formulation can still be used for turbulent cases if Eqns. (3.51) and (3.52) are combined into

$$\frac{D\zeta}{Dt} = \nu_o \nabla^2 \zeta + \frac{\partial}{\partial y}\left(\frac{\partial \overline{u^2}}{\partial x} + \frac{\partial \overline{uv}}{\partial y}\right) - \frac{\partial}{\partial x}\left(\frac{\partial \overline{uv}}{\partial x} + \frac{\partial \overline{v^2}}{\partial y}\right) - g\frac{\partial \widetilde{\rho}}{\partial x} \tag{3.73}$$

The streamfunction equation remains the same as Eqn. (3.43).

The fluctuation variable boundary conditions are

$$\frac{\partial \overline{u_I^2}}{\partial x}(0,y,t) = 0,\ \ \overline{u_I^2}(\infty,y,t) = 0\,,\ \ \frac{\partial \overline{\rho^2}}{\partial x}(0,y,t) = 0$$

$$\overline{u_I^2}(x,0,t) = 0\,,\ \ \overline{u_I^2}(x,\infty,t) = 0\,,\ \ \overline{\rho^2}(x,0,t) = 0\,,\ \ \overline{\rho^2}(x,\infty,t) = 0 \tag{3.74}$$

where I = 1, or 2, or 3, without summation, and

$$\overline{uv} = 0\,,\ \overline{\rho u} = 0\,,\ \text{and}\ \overline{\rho v} = 0 \tag{3.75}$$

on all the boundaries.

3.5 Dimensionless Form of the Equations

The system of equations were made dimensionless using the initial vortex half-span, s_0, as the characteristic length and the initial circulation, Γ_0, along with the fluid density, ρ_0, to formulate the other dimensionless variables. The characteristic flow Reynolds number is

$$Re = \Gamma_0/\nu_o \,. \tag{3.76}$$

Characteristic velocity, time and pressure are given by Γ_0/s_0, s_0^2/Γ_0 and $\rho_o\Gamma_0^2/s_0^2$, respectively.

If the same notations for the dimensionless variables as the corresponding dimensional variables are used, the non-dimensional form of the vorticity transport equation (3.41) becomes

$$\frac{\partial\zeta}{\partial t} + \left(\vec{u}\cdot\vec{\nabla}\right)\zeta = -\frac{1}{F_v^2}\frac{\partial\tilde{\rho}}{\partial x} + \frac{1}{Re}\nabla^2\zeta \,, \tag{3.77}$$

where

$$F_v^2 = \Gamma_0^2/gs_0^3 \tag{3.78}$$

is a Froude number, while the dimensionless form of the streamfunction is the same as Eqn. (3.43). The density departure equation (3.40) becomes

$$\frac{\partial\widetilde{\rho}}{\partial t} + u\frac{\partial\widetilde{\rho}}{\partial x} + v\frac{\partial\widetilde{\rho}}{\partial y} = n^2 v \,, \tag{3.79}$$

where the non-dimensional density/temperature gradient is defined by

$$n^2 \equiv \frac{\beta s_o}{T_o} \,. \tag{3.80}$$

In fact, all the corresponding non-dimensional governing equations can be obtained by just replacing ν_o , g and β with Re , $1/F_v^2$ and n^2, defined in Eqns. (3.76), (3.78) and (3.80), respectively. The actual effects of stratification depend on the ratio between n^2 and F_v^2, which will give another dimensionless parameter called the non-dimensional Brunt-Väisälä Frequency. The physical meaning of this parameter will be discussed in Chapter 8.

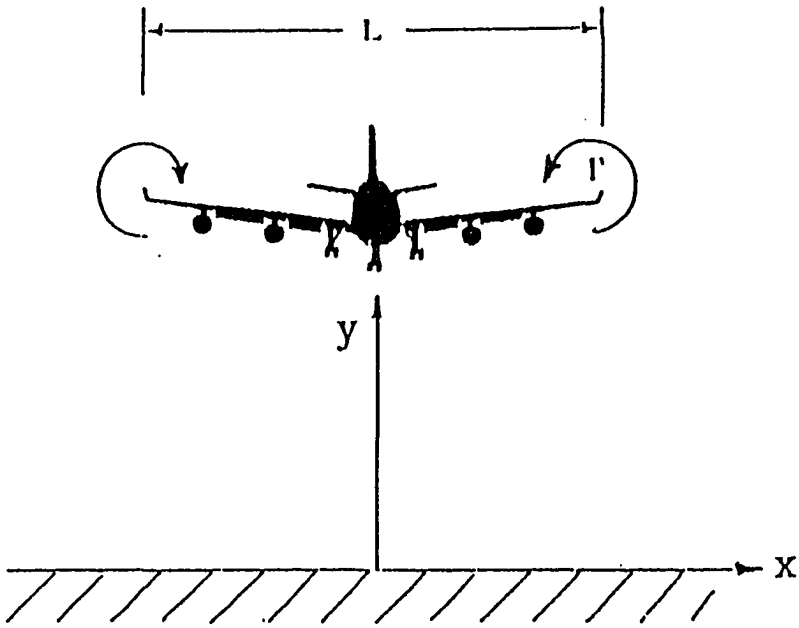

Figure 3.1 Right hand coordinate system employed

Chapter 4 Domain Transformation and Boundary Conditions

4.1 Domain Transformation

A moving grid was considered for this study but was discarded subsequently, due to the complexity of the vortex trajectory in ground effect and to uncertainty in the viscous zones requiring fine grid resolution. It was deemed more reasonable to pack grid points adjacent to the symmetry- and ground-planes and allow the vortex system to move with respect to the grid. This was possible because the nominal regions where viscous effects occurred were known to a first order of approximation. It is noted further that the elliptic character of the incompressible flow field mandates enforcing the boundary conditions at the infinite limits of x and y or alternatively the development of rigorous boundary condition approximations within a finite domain must be addressed.

Bilanin *et al.* (1977) and Ting (1983) studied the far field boundary condition problem. They used the far field expansions of Poisson integrals which could be employed in a finite subdomain of an unbounded fluid. By doing this, they obtained the approximate solutions for streamfunctions at the boundaries of the finite subdomain. The exponential decay laws for vorticity distributions were required for the convergence of the far field expansions (Ting 1983), since the convergence of Poisson integrals must be guaranteed by the vorticity distribution. The expansions were extended by Ting (1983) using integral invariants. Unfortunately, neither the decay laws nor the integral invariants apply when a

no-slip boundary is present, because the vorticity distribution in the viscous ground-plane boundary layer cannot be estimated *a priori*.

Here a coordinate mapping has been used, employing a simple exponential transformation which yields densely packed grid points near the ground plane and stretches the grid as the infinite limits are approached. The mapping

$$X = a\left(1 - e^{-bx}\right),$$
$$Y = c\left(1 - e^{-dy}\right), \tag{4.1}$$

transforms $0 \leq x < \infty,\ 0 \leq y < \infty$ into the finite domain $0 \leq X < a,\ 0 \leq Y < c$. The corresponding spacing intervals are

$$\Delta X \approx abe^{-bx}\Delta x\,,$$
$$\text{and } \Delta Y \approx cde^{-dy}\Delta y\,. \tag{4.2}$$

Hence boundary layer and vortex core resolution can be controlled by adjusting arbitrary constants a, b, c and d.

Since the ground plane spacing is compressed automatically via the coordinate mapping, resolution requirements are more severe in the far field. In addition, vortex core resolution in the vertical direction is most sensitive at start-up ($y = y_0$), while horizontal resolution is least accurate at the end of the numerical simulation (when the vortex core is at the greatest horizontal distance from the symmetry plane) — say x_l. Since the vortex is expected to dilate as time increases, selecting the appropriate grid spacing based on the initial vortex core size produces conservative spacing levels at later times.

As a representative example, when the initial vortex core radius is $r_c = 0.2$, it has been required that $\Delta y_{\max} = 0.02\ (= r_c/10)$ at y_0, and that $\Delta x_{\max} = 0.1\ (= r_c/2)$ at

x_l. The $\Delta x_{\max}$ spacing will be more compact relative to the vortex core due to dilation beginning from $t = 0$. However, the spacing interval is given by:

$$\Delta X \leq 0.1\ abe^{-bx_l}\,, \tag{4.3}$$

and

$$\Delta Y \leq 0.02\ cde^{-dy_o}\,. \tag{4.4}$$

Since the number of grid increments in the X-direction must satisfy $M\Delta X = a$, while $N\Delta Y = c$, the requirements for M and N are:

$$M \geq \frac{10e^{bx_l}}{b}\,, \tag{4.5}$$

and

$$N \geq \frac{50e^{dy_o}}{d}\,. \tag{4.6}$$

The minimum number of grid points for acceptable resolution occurs when $b = 1/x_l$ and $d = 1/y_0$, and is given by

$$M \geq 10x_l e\,, \tag{4.7}$$

and

$$N \geq 50y_o e\,. \tag{4.8}$$

A representative segment of a 150×300 grid is shown in physical coordinates in Figure 4.1. That system was set up for a vortex pair, located initially at $x_0 = \pm 1,\ y_0 = 2$, and was inteded to resolve the lateral trajectory out to $x_l = 5$. The large lateral resolution requirement, coupled with the need to resolve the very thin viscous ground-plane boundary layer, produces very different packing in the two coordinate directions.

4.2 Vorticity-Streamfunction Boundary Conditions and Their Compatibility with Velocity Boundary Conditions

Since the vorticity-streamfunction formulation is used in this study, all the boundary conditions, as in Chapter 3, are given for vorticity and streamfunction rather than requiring velocity boundary conditions. If the boundary conditions on the velocity field were enforced directly, the streamfunction would be over-determined. The present problem is not well-posed unless it can be shown that the boundary conditions for the vorticity-streamfunction formulation satisfy equivalent velocity boundary conditions, at least within the computational order of accuracy. The mathematical aspects of the equivalent requirements have been discussed by Anderson (1986). In the following, it is necessary to verify that the necessary boundary condition compatibility can be achieved in the transformed domain.

The boundary conditions in the transformed domain are:

$$\zeta(0,Y,t) = 0, \qquad \psi(0,Y,t) = 0, \tag{4.9}$$

$$\zeta(a,Y,t) = 0, \qquad \psi(a,Y,t) = 0, \tag{4.10}$$

$$\zeta(X,0,t) = -c^2 d^2 \frac{\partial^2 \psi}{\partial Y^2}(X,0,t), \tag{4.11}$$

$$\psi(X,0,t) = 0, \tag{4.12}$$

$$\zeta(X,c,t) = 0, \quad \text{and} \quad \psi(X,c,t) = 0. \tag{4.13}$$

Following Roache (1972), the first-order accurate, discretized expression for the ground-plane vorticity, Eqn.(4.11), can be developed using the Taylor series expansion

$$\psi_n = \psi|_{y=0} + \Delta y \frac{\partial \psi}{\partial y}\Big|_{y=0} + \frac{(\Delta y)^2}{2}\frac{\partial^2 \psi}{\partial y^2}\Big|_{y=0} + O\Big((\Delta y)^3\Big)\,, \tag{4.14}$$

where the subscript, n, indicates the grid locations adjacent to the ground plane. Since on the ground boundary, $\psi|_{y=0} = 0$ and $\frac{\partial \psi}{\partial y}|_{y=0} = 0$, the ground-plane vorticity is given in the transformed domain as

$$\zeta(X, 0, t) \approx -2\psi_n c^2 d^2 / \Delta Y^2\,. \tag{4.15}$$

This is the equivalent vorticity non-slip boundary condition on the ground. In this study, the vertical grid spacing was constructed with sufficient fineness to permit implementation of the no-slip boundary condition on the ground plane without exaggerating numerically the viscous interaction, as was encountered previously by Delisi, Robins and Fraser (1987).

While the velocity boundary conditions appear to be over specified, they are compatible with the velocity components in the transformed domain, given by

$$\begin{aligned} u &= \frac{\partial \psi}{\partial Y} \cdot d \cdot (c - Y) \\ v &= -\frac{\partial \psi}{\partial X} \cdot b \cdot (a - X) \end{aligned} \tag{4.16}$$

which can be verified. The symmetry-plane boundary condition, Eqn. (4.9), gives

$$u(0, Y, t) = \frac{\partial \psi(0, Y, t)}{\partial Y} \cdot d \cdot (c - Y) = 0\,, \tag{4.17}$$

and

$$\frac{\partial v}{\partial x}\Big|_{x=X=0} = -\frac{\partial^2 \psi}{\partial x^2}\Big|_{x=0} = \left(\zeta + \frac{\partial^2 \psi}{\partial y^2}\right)\Big|_{x=0} = \zeta(0,Y,t) + \frac{\partial^2 \psi(0,Y,t)}{\partial y^2} = 0\,. \quad (4.18)$$

At the infinite boundary limits, Eqns. (4.10) and (4.13) give

$$\begin{aligned} u(a,Y,t) &= \frac{\partial \psi(a,Y,t)}{\partial Y} \cdot d \cdot (c - Y) = 0\,, \\ v(a,Y,t) &= -\frac{\partial \psi}{\partial X}\Big|_{X=a} \cdot b \cdot (a - a) = 0\,, \end{aligned} \quad (4.19)$$

and

$$\begin{aligned} u(X,c,t) &= \frac{\partial \psi}{\partial Y}\Big|_{Y=c} \cdot d \cdot (c - c) = 0\,, \\ v(X,c,t) &= -\frac{\partial \psi(X,c,t)}{\partial X} \cdot b \cdot (a - X) = 0\,. \end{aligned} \quad (4.20)$$

The zero normal-velocity component requirement at the ground boundary is easily verified as

$$v(X,0,t) = -\frac{\partial \psi(X,0,t)}{\partial X} \cdot b \cdot (a - X) = 0\,, \quad (4.21)$$

while the non-slip condition can be expressed using the Taylor expansion Eqn. (4.14), with the ground vorticity boundary condition Eqn. (4.15), so that

$$u(X,0,t) = \frac{\partial \psi}{\partial y}\Big|_{y=0} = O\Big((\Delta y)^2\Big)\,, \quad (4.22)$$

which means that the first-order accurate vorticity ground-boundary condition guarantees enforcement of the non-slip boundary condition to second-order accuracy. Thus all of the velocity boundary conditions can be satisfied to within computational accuracy. These boundary conditions also satisfy the integral conditions developed by Anderson (1986).

An alternating-direction implicit (ADI) scheme (Anderson, Tannehill and Pletcher 1984) was used to solve the vorticity transport equation, Eqn. (3.41), with the upwind

flux-splitting method applied to the convection terms and central-differencing for the diffusion terms. An efficient Poisson solver (Swarztrauber and Sweet, 1979) was used to solve Eqn. (3.43), which can achieve 10^{-8} accuracy in the iteration residue. Viscous flow in a driven cavity was used as the test problem for that computational scheme to explore the capability of capturing the secondary-vortex evolution phenomena associated with high Reynolds number flow cases. The systematic numerical studies of this problem are well-documented in Bozeman and Dalton (1973) and Rubin and Harris (1975).

Based upon the discussions shown in Chapter 5, it has been determined that the vortex core centers can be placed initially at $x_0 = 1$, $y_0 = 2$ (and $x_0 = -1$, $y_0 = 2$, from symmetry) to start the simulations. That vertical distance ($y_0 = 2$) has been deemed close enough to the ground plane to produce detectable coupling effects after moderate start-up time intervals, but it is also far enough from the ground plane to enable the vortex flow field to establish itself prior to strong ground-plane interactions. The initial vortex core is assumed to have a core radius, r_c, of 0.2, which is about the size of the vortex core after the rolling-up is complete at moderate Reynolds numbers (Barker and Crow, 1977) and the wake of the vortex pair has evolved but the viscous vortex region is still small. A 150×300 grid in the x-y plane has then been employed in the numerical simulations reported herein for the right-half upper plane in the symmetric flow cases, while a 300×300 grid has been used in non-symmetric cases in Chapter 9. Computations were continued until the vortex system moved out of the grid region possessing the required resolution. Calculations have been performed using the Cray II and Cray Y-MP computers at NASA Langley Research Center.

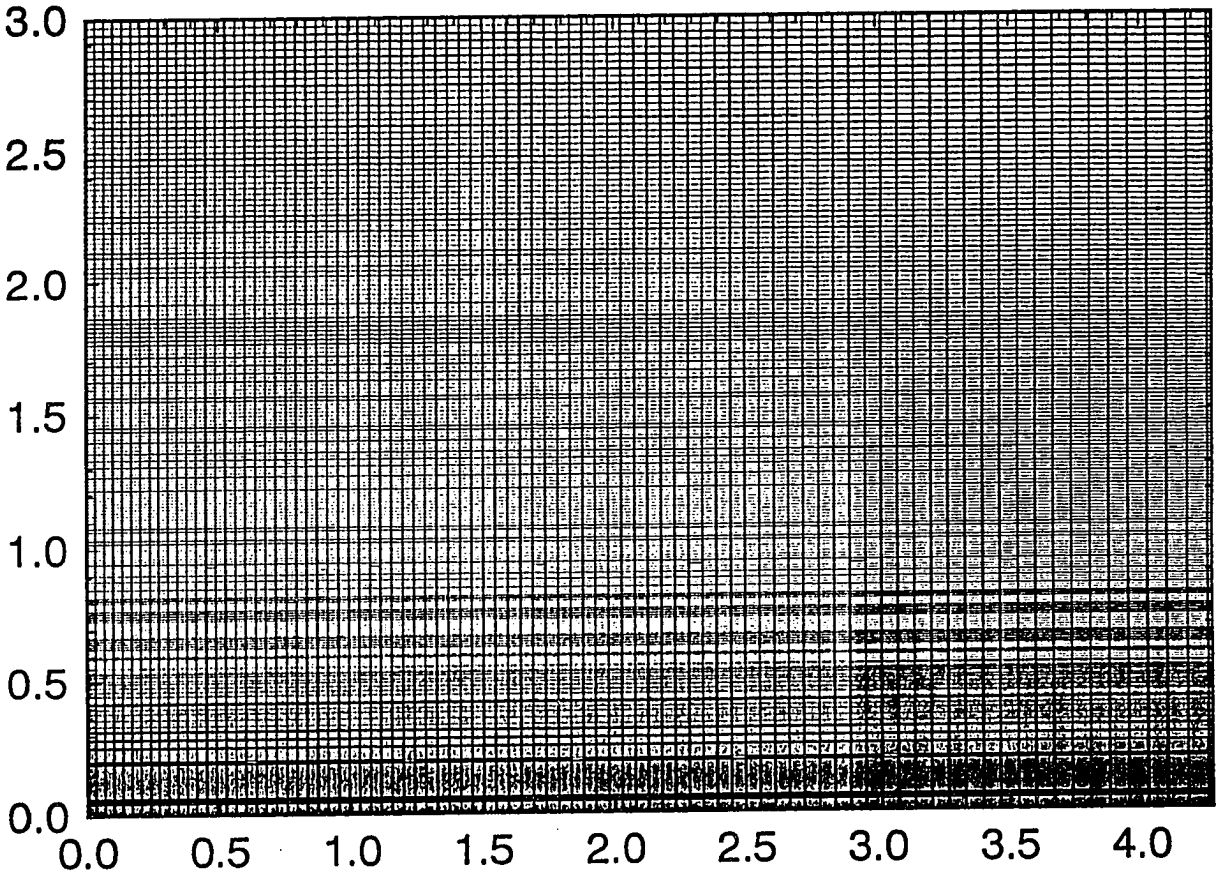

Figure 4.1 Sketch of part of the 150×300 grid

Chapter 5 Asymptotic Techniques for Flow Field Initialization

Since the flow is for the most part inviscid, with an unsteady, viscous ground-plane boundary layer and a small viscous vortex core region, problems were encountered in starting the numerical calculations. A goal of this study was to extend the Reynolds number range over which vortex-ground plane interactions could be modeled. Consequently, viscous effects were anticipated in both the vortex core and boundary-layer regions long before any interactions between the vortex core(s) and boundary layer occurred. Furthermore, a fine numerical grid was required for both the vortex region, including its path of descent, and the ground-plane boundary layer. The grid requirements demanded an initial velocity field which was free of anomalous velocity gradients. In the following, approximate analytic solutions for both the regions containing vortex cores and within the ground boundary are obtained to initiate the computational scheme. The outer flow (outside these regions) can be considered as a potential flow. Considerable effort has been devoted to developing an appropriate initial velocity field which resolved the ground effect region in the numerical simulation, without producing non-physical numerical start-up transients.

Asymptotic expansions, in terms of $\epsilon = \sqrt{t/R_e}$ (recall that t is dimensionless), have been used for both the outer flow and the inner flow representations. That approach is warranted because those solutions can be developed as similarity solutions in terms of an unsteady Reynolds number t/Re. The Oseen (1911) type vortex, which has been used as

the initial vortex, represents this type of similarity solution, where the vortex core size depends on t/Re. Blasius' solution for an unsteady boundary layer (Schlichting, 1979) is also a similarity solution in terms of t/Re and t. However, that solution is only valid when the outer velocity is steady, which is obviously not true for the present problem. When the outer flow is non-uniform and unsteady, the inner solutions cannot be expanded simply in terms of a single parameter ϵ, because the expansions cannot match the outer flow. The difficulty can be related to the boundary layer similarity property requirements developed by Schlichting (1979), which cannot be satisfied using a single parameter. However, since the influence of the outer flow on the inner boundary layer depends strongly on both Re and elapsed time, it is logical to consider a series representation which includes both time t and the small parameter ϵ (Nam, 1990). For the present problem, it will be shown that analytic solutions can be obtained when the inner solution, near the ground boundary, is expanded in terms of both time and the small parameter ϵ.

The two-dimensional, unsteady incompressible, Navier-Stokes equations were used as the governing equations. Peace and Riley (1983) and Nam (1990) have both employed the fourth-order differential equation for streamfunction, which eliminated the pressure terms, in studies involving similar unsteady boundary layer problems. However, the Navier-Stokes equations represent one integration of the fourth-order streamfunction equation. Consequently, that integration recovers the pressure terms, which are included explicitly, and yields the additional advantage that the streamfunction and velocity can be matched asymptotically along with pressure by employing van Dyke (1976) type matching procedures. Thus the present Navier-Stokes formulation enables a more consistent asymptotic approach.

After the asymptotic solutions are obtained, the dimensionless time limits, over which the analytic initial solutions can be employed, will be discussed. These limits must meet accuracy requirements for the truncated asymptotic expansions, as well as satisfy the resolution requirements imposed by the grid developed in the previous chapter.

5.1 Flow Field Near the Initial Vortices and the Outer Flow

The Oseen vortex is an exact solution to the Navier-Stokes equations for the diffusion of a vortex filament into a viscous region of infinite extent. For any time greater than zero, the Oseen vortex includes viscosity, while at $t = 0$, it is an inviscid point vortex. Hence, placing a pair of those vortices at $\pm x_0,\ y_0$ at $t = 0$, is equivalent to placing a pair of potential vortices at those locations, but then allowing viscous effects to occur immediately after placement. Oseen vortex solutions do not include either non-linear coupling of the vortex pair or the viscous influence of a ground plane. Peace and Riley (1983) proved that the influence of one vortex on the other is on the order of $O((t/Re)^2)$, which is a higher order influence than can be considered in the truncated asymptotic expansion series employed here. Therefore, a mirror image pair of Oseen vortices (at $\pm x_0,\ -y_0$) can be used to initiate a ground plane interaction without introducing conflicting approximations. Since those vortices evolve immediately as viscous flows, they appear to be a more realistic starting flow than that of a pair of potential vortices, for any practical numerical grid.

The actual numerical computations start when the vortices have finite cores. This is true physically because some vorticity has already been rolled up into the center of the wake vortices during the rolling-up process. For the purpose of specifying initial conditions for the numerical solution, the Oseen vortices were assumed to have evolved

sufficiently to possess finite vortex cores prior to initiation of the numerical computations. The core size was assumed to be sufficiently small, in comparison with the distances between the viscous regions, so that direct viscous interactions between the vortices and with the ground could be neglected. Hence, other than a time restriction on the asymptotic solution, the vortex starting positions for numerical modeling, with respect to permitting the evolution of realistic viscous interactions, needed to be justified.

Since the characteristic length was chosen as the initial half-span of the vortex pair, x_0 was logically assumed to be unity. On the other hand, y_0 must be chosen to satisfy the conditions: (1) the distances between the vortices and ground boundary must be large enough to permit direct viscous interactions to be neglected; and (2) for computational efficiency, the initial heights must be as small as possible to avoid wasting the considerable computational resources required for the Navier-Stokes model of the flow field. Vortex trajectories can be predicted approximately via potential flow theory at large distances from the ground plane.

Vortex core size is a reasonable measure of the viscous scales in this initial flow problem. After rolling-up, the core radius of the wake vortex is about twenty percent of the half-span for a moderate Reynolds number vortex system (Barker and Crow, 1977) and the core size changes more slowly with time at high Reynolds numbers. A non-dimensional initial core radius $r_c = 0.2$, was chosen here and it was assumed that the core size was constant during the development of the initial flow field.

Liu and Ting (1987) used the initial vortex core size as a small parameter in an inviscid asymptotic representation for vortices near the ground. They tried to avoid viscous interactions between the vortices and the ground boundary in their inviscid solution and

suggested that if the vortex was a few core-diameters away from the ground, the inviscid solution was still valid. Since the boundary-layer thickness was not considered in their inviscid solution, a larger initial height, y_0, was anticipated for the present problem.

An initial height which was one order of magnitude larger than the initial vortex core size was considered to be adequate. Since the initial boundary layer could be resolved by the present computational grid when the boundary layer thickness was about one tenth of the vortex core, the order of magnitude increase in initial height satisfied the uncoupled viscous development requirements without over-taxing computer resources. Therefore, in the following calculations, it has been chosen that

$$y_0 = 10r_c = 2\,. \tag{5.1}$$

The flight experiments reported by Dee and Nicholas (1968), represented in Figure 2.2, reinforce the idea that the vortex trajectories begin to deviate measurably from their potential theory predictions only within a height interval of approximately two half-spans above the ground. Therefore, the prescribed initial height can avoid the consumption of viscous computational resources on an essentially inviscid solution (if y_0 is too large) and yet safely satisfy the requirement that direct viscous interactions can be neglected initially.

In effect, an Oseen vortex in the first quadrant can be represented in the form of a non-dimensional vorticity function,

$$\zeta = \frac{1}{\pi r_c^2} exp\left(-\frac{r^2}{r_c^2}\right) \tag{5.2}$$

where r is the distance from the vortex center. Thus, it can be seen that the viscous influence of the vortex decays exponentially with distance. The maximum initial viscous influence between the two vortices in the vortex pair is on the order of $exp(-x_0^2/r_c^2) \approx$

e^{-25} and the maximum initial viscous vortex influence from the ground was estimated to be on the order of $exp(-y_0^2/r_c^2) \approx e^{-100}$, for an initial vortex pair height of $y_0 = 2$ with vortex core radii equal to 0.2. Thus the magnitudes of the initial viscous effects are so small that they can be neglected justifiably.

From the previous discussion, it is apparent that each viscous region can be treated separately, and the outer region can be modeled as a potential flow field. As mentioned at the beginning of the section, the Oseen vortex can be as accurate as $O((t/Re)^2)$ in the region near the vortices, but since the outer regions of the Oseen vortices are essentially inviscid, the ground boundary layer can be initiated by using the unmodified potential vortex pressure and velocity distributions. The development of the initial boundary-layer flow field will be presented in the next section. The present section will be concluded by developing the appropriate "far-field" velocity components, required to drive the unsteady boundary layer during the time over which the asymptotic solutions apply.

The outer flow field has been treated as the far field of a pair of potential vortices, with their associated ground plane images. Utilizing non-dimensional Cartesian velocity components, the potential vortex flow system can be represented by

$$U_c(x,y,t) = (y-y_0)[\Phi(x,y,t;x_0,y_0) - \Phi(x,y,t;-x_0,y_0)] + (y+y_0)[\Phi(x,y,t;x_0,-y_0) - \Phi(x,y,t;-x_0,-y_0)] \quad (5.3)$$

and

$$V_c(x,y,t) = (x-x_0)[\Phi(x,y,t;x_0,y_0) - \Phi(x,y,t;x_0,-y_0)] + (x+x_0)[\Phi(x,y,t;-x_0,-y_0) - \Phi(x,y,t;-x_0,y_0)] \quad (5.4)$$

where

$$\Phi(x,y,t;\alpha,\beta) = \frac{1}{2\pi}\frac{1}{(x-\alpha)^2+(y-\beta)^2} \tag{5.5}$$

and where $x_0 = x_0(t)$, $y_0 = y_0(t)$ represent the instantaneous centers of the vortices. It should be noted here that during the time interval over which the asymptotic solutions apply, the downward displacement of the vortex pair can be neglected. Furthermore, these velocity functions are restricted to small time, where they do not alter the asymptotic matching conditions.

In the next section, it will be shown that the maximum allowable dimensionless time for the asymptotic representations cannot exceed 0.1 for the required truncation accuracy. Since the initial induced non-dimensional velocity at one vortex core is less than 0.1 at the initial position, $x_0 = 1$ and $y_0 = 2$, during the time period over which the asymptotic solution develops, changes in the initial vortex core positions are only $O(10^{-3})$ and can be neglected, as stated previously. The trajectories for x_0 and y_0 are only important when the unsteadiness of the outer velocity field is considered. That is, while $\frac{\partial x_0}{\partial t}$ and $\frac{\partial y_0}{\partial t}$ cannot be neglected in terms of their influence on the outer flow velocities, the values of x_0 and y_0 can be treated as constants in terms of estimating the imposed initial velocity distribution above the ground-plane boundary layer.

5.2 Asymptotic Solutions for the Ground Boundary Layer

Analytic perturbation methods can be used to predict the flow near the ground plane during the initial time interval (when the magnitudes of local velocity gradients create severe problems for numerical techniques). In the following development, a two-term expansion has been developed for that application. First, the expansion for the streamfunction and velocity will be presented. Then matching conditions have been

obtained by switching outer and inner variables according to van Dyke's (1976) procedure. Since pressure can be derived in incompressible flows when the velocity field is known, pressure matching is accomplished through the governing equations. Hence, the pressure distribution will be developed after the governing equations for the inner and outer regions are discussed. Subsequently, closed form solutions for the two-term expansions are developed. Finally, the maximum time allowed, in terms of the validity of the solution, and the minimum development time required for the numerical grid are discussed.

5.2.1 Expansions and Matching for Streamfunction and Velocity

The appropriate streamfunction for the outer flow can be written

$$\Psi = \Psi_o(x,y,t) + \epsilon\Psi_1(x,y,t) + O\left[\epsilon^2\right], \tag{5.6}$$

where

$$U = \frac{\partial\Psi}{\partial y} = \frac{\partial\Psi_o}{\partial y} + \epsilon\frac{\partial\Psi_1}{\partial y} + O\left[\epsilon^2\right], \tag{5.7}$$

and

$$V = -\frac{\partial\Psi}{\partial x} = -\frac{\partial\Psi_o}{\partial x} - \epsilon\frac{\partial\Psi_1}{\partial x} + O\left[\epsilon^2\right]. \tag{5.8}$$

This streamfunction must satisfy the initial potential vortex requirements of both a symmetry plane and a ground plane.

Similarly, the inner flow is represented as

$$\psi = 2\epsilon[\psi_o(x,\eta,t) + \epsilon\psi_1(x,\eta,t)] + O\left[\epsilon^3\right], \tag{5.9}$$

where $\eta = y/2\epsilon$ is the inner stretched vertical coordinate (where, following Blasius's solution [Schlichting, 1979], 2ϵ is used instead of ϵ, for algebraic simplicity in the matching). Here, the inner velocity components are

$$u = \frac{\partial \psi}{\partial y} = 2\epsilon\left(\frac{1}{2\epsilon}\frac{\partial \psi_o}{\partial \eta} + \frac{1}{2}\frac{\partial \psi_1}{\partial \eta}\right) + O[\epsilon^2]$$
$$= \frac{\partial \psi_o}{\partial \eta} + \epsilon\frac{\partial \psi_1}{\partial \eta} + O[\epsilon^2] \ , \tag{5.10}$$

and

$$v = -\frac{\partial \psi}{\partial x} = -2\epsilon\left(\frac{\partial \psi_o}{\partial x} + \epsilon\frac{\partial \psi_1}{\partial x}\right) + O[\epsilon^3] \ . \tag{5.11}$$

This streamfunction must satisfy the no-slip boundary conditions.

Following van Dyke's (1976) generalized matching principle, which requires that the inner and outer asymptotic expansions match at their overlapping limits, the outer expansion is rewritten in terms of the inner variable η, while the inner expansion is rewritten in the outer variable y. Subsequently, both the streamfunction and velocity expansions are rewritten and the corresponding terms must be matched. Using this matching procedure allows the streamfunction and velocity representations to be matched simultaneously along the overlap zone, and yields:

For $O[\epsilon^o]$:

$$\Psi_o(x, 0, t) = 0 \ , \tag{5.12}$$

$$\frac{\partial \Psi_o}{\partial y}(x, 0, t) = \frac{\partial \psi_o}{\partial \eta}(x, \infty, t) = U_o \ , \tag{5.13}$$

and

$$\frac{\partial \Psi_o}{\partial x}(x, 0, t) = 0 \ . \tag{5.14}$$

For $O[\epsilon^1]$:

$$\Psi_1(x,0,t) = 2\psi_o(x,\eta,t)\Big|_{\eta\to\infty} - 2\eta\frac{\partial\Psi_o}{\partial y}(x,0,t)\Big|_{\eta\to\infty}, \tag{5.15}$$

$$\frac{\partial\Psi_1}{\partial y}(x,0,t) = \frac{\partial\psi_1}{\partial\eta}(x,\eta,t)\Big|_{\eta\to\infty} - 2\eta\frac{\partial^2\Psi_o}{\partial y^2}(x,0,t)\Big|_{\eta\to\infty}, \tag{5.16}$$

and

$$\frac{\partial\Psi_1}{\partial x}(x,0,t) = 2\frac{\partial\psi_o}{\partial x}(x,\eta,t)\Big|_{\eta\to\infty} - 2\eta\frac{\partial^2\Psi_o}{\partial x\partial y}(x,0,t)\Big|_{\eta\to\infty}. \tag{5.17}$$

As expected, Eqns. (5.12)-(5.17) either give the bottom boundary condition for the outer flow or the top boundary condition for the inner-flow. Equations (5.12) and (5.14) are equivalent and they therefore give one boundary condition for Ψ_o, which is obviously the no-penetration boundary condition. Equation (5.13) is the top boundary condition for ψ_o which must match (at the edge) the x-component of velocity, U_o. Equations (5.15) and (5.17) are also equivalent and they provide a boundary condition for Ψ_1, while Eqn. (5.16) is a boundary condition for ψ_1. The equivalence between Eqns. (5.12) and (5.14) and between (5.15) and (5.17) shows that the streamfunction and velocity matching can be achieved simultaneously and without contradiction in this procedure. The physical boundary conditions are thus retained by the mathematical manipulation.

From the matching procedure, the solution for the two series can proceed sequentially; first the outer solution, Ψ_o, then the inner solution, ψ_o can be developed, followed sequentially by solution of Ψ_1, and so on.

5.2.2 Governing Equations

As stated previously, the governing equations used are the two-dimensional unsteady, incompressible Navier-Stokes equations. Since continuity is implied by introducing the streamfunction, the conservation of momentum equations are all that need to be considered.

a. Outer Flow

Because viscous terms do not have any direct effect in the series until terms of order ϵ^2 are important, it is not necessary to include viscous effects for the two-term representation of the outer solution. Thus, the outer flow must satisfy the two-dimensional Euler equations:

$$\frac{\partial U}{\partial t} + U\frac{\partial U}{\partial x} + V\frac{\partial U}{\partial y} = -\frac{\partial P}{\partial x} \ , \tag{5.18}$$

and

$$\frac{\partial V}{\partial t} + U\frac{\partial V}{\partial x} + V\frac{\partial V}{\partial y} = -\frac{\partial P}{\partial y} \ . \tag{5.19}$$

In addition, it was shown in the previous section that the induced flow, resulting from the far field of the Oseen vortices, is irrotational near the edge of the boundary layer, justifying the use of the potential flow relation

$$\nabla^2 \Psi = 0 \, , \tag{5.20}$$

instead of Eqns. (5.18) and (5.19). That has been done here and the Euler equations have been used only to determine the pressure field from the velocity field.

The following equations result from consideration of different orders of ϵ:

$$O[\epsilon^o]: \quad \nabla^2\Psi_o = 0\,, \tag{5.21}$$

and

$$O[\epsilon^1]: \quad \nabla^2\Psi_1 = 0\,. \tag{5.22}$$

Since the outer solution here is only used for the purpose of generating the boundary-layer solution, the potential solution may or may not be applied to the whole outer flow field. It is also noted that, to $O(\epsilon^1)$, the Oseen vortex solution has no viscous influence because it is introduced at $O(\epsilon^2)$ accuracy.

b. Inner Flow

The dimensionless boundary layer momentum equation can be written

$$\frac{\partial u}{\partial t} + u\frac{\partial u}{\partial x} + v\frac{\partial u}{\partial y} = -\frac{dp}{dx} + \frac{1}{Re}\frac{\partial^2 u}{\partial y^2}\ , \tag{5.23}$$

where the standard boundary layer approximations apply. (When the vortex system approaches closer to the ground, it is obvious that $\frac{\partial p}{\partial y}$ will become important, thus negating the boundary layer approximations.) From Eqns. (5.9) and (5.10), the velocity derivatives can be calculated to yield:

$$\frac{\partial u}{\partial t} = \frac{\partial^2\psi_o}{\partial\eta\partial t} - \frac{\eta}{2t}\frac{\partial^2\psi_o}{\partial\eta^2} + \epsilon\left[\frac{1}{2t}\frac{\partial\psi_1}{\partial\eta} + \frac{\partial^2\psi_1}{\partial\eta\partial t} - \frac{\eta}{2t}\frac{\partial^2\psi_1}{\partial\eta^2}\right] + O[\epsilon^2]\,, \tag{5.24}$$

$$\frac{\partial u}{\partial y} = \frac{1}{2\epsilon}\left[\frac{\partial^2\psi_o}{\partial\eta^2} + \epsilon\frac{\partial^2\psi_1}{\partial\eta^2}\right] + O[\epsilon]\,, \tag{5.25}$$

and

$$\frac{\partial^2 u}{\partial y^2} = \frac{1}{4\epsilon^2}\left[\frac{\partial^3 \psi_o}{\partial \eta^3} + \epsilon \frac{\partial^3 \psi_1}{\partial \eta^3}\right] + O[\epsilon^o]\,. \tag{5.26}$$

Now, representing pressure as:

$$p = p_o(x,t) + \epsilon p_1(x,t) + O\left[\epsilon^2\right], \tag{5.27}$$

these expressions (Eqns. 5.24–5.27), along with Eqn. (5.11), can be substituted into Eqn. (5.23), to obtain the streamfunction equations for different orders of ϵ.

For $O[\epsilon^o]$:

$$\begin{aligned}\frac{\partial^2 \psi_o}{\partial \eta \partial t} - \frac{\eta}{2t}\frac{\partial^2 \psi_o}{\partial \eta^2} + \frac{\partial \psi_o}{\partial \eta}\frac{\partial^2 \psi_o}{\partial \eta \partial x} - \frac{\partial^2 \psi_o}{\partial \eta^2}\frac{\partial \psi_o}{\partial x} \\ = -\frac{dp_o}{dx} + \frac{1}{4t}\frac{\partial^3 \psi_o}{\partial \eta^3}\quad .\end{aligned} \tag{5.28}$$

The three boundary conditions are the no-penetration and non-slip boundary conditions and the matching condition Eqn. (5.13):

$$\psi_o(x,0,t) = 0\,, \tag{5.29}$$

$$\frac{\partial \psi_o}{\partial \eta}(x,0,t) = 0\,, \tag{5.30}$$

and

$$\frac{\partial \psi_o}{\partial \eta}(x,\infty,t) = \frac{\partial \Psi_o}{\partial y}(x,0,t) = U_o\,. \tag{5.31}$$

For $O\left[\epsilon^1\right]$:

$$\begin{aligned}\frac{1}{2t}\frac{\partial \psi_1}{\partial \eta} + \frac{\partial^2 \psi_1}{\partial \eta \partial t} - \frac{\eta}{2t}\frac{\partial^2 \psi_1}{\partial \eta^2} + \frac{\partial \psi_o}{\partial \eta}\frac{\partial^2 \psi_1}{\partial \eta \partial x} \\ + \frac{\partial \psi_1}{\partial \eta}\frac{\partial^2 \psi_o}{\partial \eta \partial x} - \frac{\partial \psi_o}{\partial x}\frac{\partial^2 \psi_1}{\partial \eta^2} - \frac{\partial \psi_1}{\partial x}\frac{\partial^2 \psi_o}{\partial \eta^2} \\ = -\frac{dp_1}{dx} + \frac{1}{4t}\frac{\partial^3 \psi_1}{\partial \eta^3}\,.\end{aligned} \tag{5.32}$$

The three boundary conditions for ψ_1 are again the solid-wall conditions and the matching condition Eqn. (5.16):

$$\psi_1(x,0,t) = 0\,, \tag{5.33}$$

$$\frac{\partial \psi_1}{\partial \eta}(x,0,t) = 0\,, \tag{5.34}$$

and

$$\frac{\partial \psi_1}{\partial \eta}(x,\eta,t)\,\Big|_{\eta\to\infty} -2\eta \frac{\partial^2 \Psi_o}{\partial y^2}(x,0,t)\,\Big|_{\eta\to\infty} = \frac{\partial \Psi_1}{\partial y}(x,0,t)\,. \tag{5.35}$$

From Eqn. (5.21),

$$\frac{\partial^2 \Psi_o}{\partial x^2}(x,0,t) + \frac{\partial^2 \Psi_o}{\partial y^2}(x,0,t) = 0\,,$$

while Eqn. (5.12) yields $\Psi_o(x,0,t) = 0$.

Hence

$$\frac{\partial^2 \Psi_o}{\partial y^2}(x,0,t) = -\frac{\partial^2 \Psi_o}{\partial x^2}(x,0,t) = 0\,. \tag{5.37}$$

Therefore, Eqn. (5.35) can be rewritten:

$$\frac{\partial \psi_1}{\partial \eta}(x,\infty,t) = \frac{\partial \Psi_1}{\partial y}(x,0,t) = U_1\,. \tag{5.38}$$

5.2.3 Pressure Gradient Matching

As mentioned earlier, to second order, $\frac{\partial P}{\partial y} = 0$, in the boundary layer for the asymptotic expansions developed here. Consequently, the pressure gradient relationship can be written:

$$\left.\frac{\partial P}{\partial x}\right|_{y=0} = \frac{dp}{dx}\,. \tag{5.39}$$

From the governing equation for the outer flow (Eqn. 5.18), the "free-slip" requirement is

$$\left.\frac{\partial U}{\partial t}\right|_{y=0} + U\left.\frac{\partial U}{\partial x}\right|_{y=0} = -\left.\frac{\partial P}{\partial x}\right|_{y=0}\,. \tag{5.40}$$

Now

$$U(x,0,t) = U_o(x,t) + \epsilon U_1(x,t) \tag{5.41}$$

so that

$O[\epsilon^o]$:

$$\frac{\partial U_o}{\partial t} + U_o\frac{\partial U_o}{\partial x} = -\frac{dp_o}{dx}\,, \tag{5.42}$$

and

$O[\epsilon^1]$:

$$\frac{\partial U_1}{\partial t} + \frac{1}{2t}U_1 + U_o\frac{\partial U_1}{\partial x} + U_1\frac{\partial U_o}{\partial x} = -\frac{dp_1}{dx}\,. \tag{5.43}$$

Thus the pressure distribution can be determined from the outer-flow representations of the velocity.

5.2.4 Solution for the Inner Flow

From the discussion at the beginning of this chapter, it was shown that in an unsteady boundary layer, a two-series expansion is needed, which will be developed here in terms of ϵ and t. It is therefore necessary to expand each inner solution, to different orders of ϵ, as power series in terms of t. Since these solutions are required only as initial flow conditions for this problem, dimensionless time can be chosen to be arbitrarily small so that only the first several terms in the asymptotic expansions are needed in each representation. Closed form solutions are thus obtained for the first two terms of the expansions.

$O[\epsilon^o]$:

Let

$$\psi_o = \sum_{p=0}^{\infty} t^p \phi_p^o(x, \eta, t) \ . \tag{5.44}$$

Then the first two terms are:

$$\psi_o = U_o f_{01} + t\left(\frac{\partial U_o}{\partial t} f_{11} + U_o \frac{\partial U_o}{\partial x} f_{12}\right) + O\left[t^2\right] . \tag{5.45}$$

Substituting Eqn. (5.45) into Eqn. (5.28), with boundary conditions, Eqns. (5.29), (5.30) and (5.31), then employing the pressure gradient Eqn. (5.42), the expressions, $f_{ij}(\eta)$, for different orders of t are

$O[t^o]$:

$$f_{01}''' + 2\eta f_{01}'' = 0, \tag{5.46}$$

subject to:

$$f_{01}(0) = f_{01}'(0) = 0 \, , \tag{5.47}$$

$$f'_{01}(\infty) = 1\,, \tag{5.48}$$

$O[t^1]$:

$$f'''_{11} + 2\eta f''_{11} - 4f'_{11} = -4 + 4f'_{01}\,, \tag{5.49}$$

subject to:

$$f_{11}(0) = f'_{11}(0) = 0\,, \tag{5.50}$$

and

$$f'_{11}(\infty) = 0\,, \tag{5.51}$$

along with

$$f'''_{12} + 2\eta f''_{12} - 4f'_{12} = -4 + 4\left(f'_{01}\right)^2 - 4f_{01}f'_{01}\,, \tag{5.52}$$

subject to:

$$f_{12}(0) = f'_{12}(0) = 0\,, \tag{5.53}$$

and

$$f'_{12}(\infty) = 0\,. \tag{5.54}$$

The solutions for f_{01}, f_{11} and f_{12} are given as:

$$f_{01} = \eta\ erf(\eta) + \frac{1}{\pi^{1/2}}e^{-\eta^2} - \frac{1}{\pi^{1/2}}\ , \tag{5.55}$$

$$f_{11} = \frac{1}{3\pi^{1/2}}\left(1 - e^{-\eta^2}\right) - \frac{2}{3}\eta^3 erfc(\eta) + \frac{2}{3\pi^{1/2}}\eta^2 e^{-\eta^2}\,, \tag{5.56}$$

and

$$f_{12} = -\frac{11}{6\pi^{1/2}}\left(1 - e^{-\eta^2} erfc(\eta)\right) + \frac{8}{3\sqrt{2}\pi^{1/2}} erf\left(\sqrt{2}\eta\right) - \frac{1}{3}\left(2 + \frac{4}{3\pi}\right)\eta^3 erfc(\eta)$$
$$- \frac{2}{3\pi^{1/2}}\eta^2 e^{-\eta^2} erfc(\eta) + \frac{1}{3\pi}\eta e^{-2\eta^2} - \frac{1}{2}\eta\, erfc^3(\eta) + \left(\frac{3}{2\pi^{1/2}} - \frac{4}{9\pi^{3/2}}\right)\left(1 - e^{-\eta^2}\right)$$
$$+ \left(\frac{1}{2} - \frac{2}{3\pi}\right)\eta erfc(\eta) - \frac{2}{3\pi^{1/2}} erf(\eta) + \left(\frac{1}{\pi^{1/2}} + \frac{4}{9\pi^{3/2}}\right)\eta^2 e^{-\eta^2} . \qquad (5.57)$$

It has been already pointed out that the derivatives of f_{01} and f_{12} are the same as the first-order and second-order solution functions, respectively, in Blasius's solution (Schlichting 1979).

$O[\epsilon^1]$:

Let

$$\psi_1 = \sum_{p=0}^{\infty} t^p \phi_p^1(x, \eta, t) \ . \qquad (5.58)$$

Then the first two terms

$$\psi_1 = U_1 g_{01} + t\left(\frac{\partial U_1}{\partial t} g_{11} + U_o \frac{\partial U_1}{\partial x} g_{12} + U_1 \frac{\partial U_o}{\partial x} g_{13}\right) + O[t^2] \qquad (5.59)$$

are gotten by substituting Eqn. (5.59) into Eqn. (5.32), with boundary conditions Eqns. (5.33), (5.34) and (5.38) and pressure gradient condition Eqn. (5.43). The following relations are thus obtained, for different orders, of t

$O[t^o]$:

$$g_{01}''' + 2\eta g_{01}'' - 2g_{01}' = -2 \, , \qquad (5.60)$$

subject to

$$g_{01}(0) = g_{01}'(0) = 0 \, , \qquad (5.61)$$

and

$$g_{01}'(\infty) = 1 \, , \qquad (5.62)$$

$O[t^1]$:

$$g_{11}''' + 2\eta\, g_{11}'' - 6g_{11}' = -4 + 4g_{01}' \,, \tag{5.63}$$

subject to:

$$g_{11}(0) = g_{11}'(0) = 0 \,, \tag{5.64}$$

and

$$g_{11}'(\infty) = 0 \,, \tag{5.65}$$

along with

$$g_{12}''' + 2\eta g_{12}'' - 6g_{12}' = -4 + 4f_{01}'g_{01}' \,, \tag{5.66}$$

subject to:

$$g_{12}(0) = g_{12}'(0) = 0 \,, \tag{5.67}$$

$$g_{12}'(\infty) = 0 \,, \tag{5.68}$$

and

$$g_{13}''' + 2\eta\, g_{13}' - 6g_{13} = -4 + 4f_{01}'g_{01}' - 4f_{01}g_{01}'' \tag{5.69}$$

subject to:

$$g_{13}(0) = g_{13}'(0) = 0 \,, \tag{5.70}$$

and

$$g_{13}'(\infty) = 0 \,. \tag{5.71}$$

The solutions for g_{01}, g_{11}, g_{12} and g_{13} are given as:

$$g_{01} = \eta + \frac{1}{2}\pi^{1/2}\eta^2 erfc(\eta) - \frac{1}{2}\eta e^{-\eta^2} - \frac{1}{4}\pi^{1/2} erf(\eta)\,, \tag{5.72}$$

$$g_{11} = \frac{\pi^{1/2}}{4}(\eta^3 + \eta^4) erfc(\eta) + \frac{1}{2}\int_o^\eta (-\eta^2 + \eta^4) e^{-\eta^2} d\eta\,, \tag{5.73}$$

$$\begin{aligned} g_{12} = \int_0^\eta \Bigg\{ & \frac{7}{4}\pi^{1/2}\left(\eta + \frac{2}{3}\eta^3\right) - \frac{\pi^{1/2}}{4}\left[\left(\eta + \frac{2}{3}\eta^3\right) erf(\eta) + \frac{2}{3\pi^{1/2}}(1+\eta^2)e^{-\eta^2}\right] \\ & + \pi^{1/2}\left(-\frac{1}{2}\eta - \eta^3\right)(erf(\eta))^2 + \left(-\frac{1}{2} - 2\eta^2\right) e^{-\eta^2} erf(\eta) - \frac{1}{8}\eta e^{-2\eta^2} \\ & - \pi^{1/2}\eta\, erf(\eta) - \frac{2}{3} erf(\eta) + \frac{2}{3} - \frac{1}{2}e^{-\eta^2}\Bigg\} d\eta\,, \end{aligned} \tag{5.74}$$

and

$$g_{13} = \frac{3}{8}\pi^{1/2}\left(\eta^2 + \frac{1}{3}\eta^4\right) erfc(\eta) + \frac{1}{2}\int_0^\eta \left(\eta^2 + \frac{1}{3}\eta^4\right) e^{-\eta^2} d\eta\,. \tag{5.75}$$

The above functions (f_{01}, f_{11}, f_{12}, g_{01}, g_{11}, g_{12}, and g_{13}) are plotted in Figures 5.1 and 5.2.

It is noted that $U_0(x,t)$ and $U_1(x,t)$ are the outer flow representations of the vortices along the ground plane ($y = 0$). These solutions are restricted to small times and U_0 is given by potential theory as

$$U_0(x,t) = \frac{4}{\pi}\frac{x_0 y_0 x}{\left[(x-x_0)^2 + y_0^2\right]\left[(x+x_0)^2 + y_0^2\right]}\,, \tag{5.76}$$

while U_1 is gotten by solving the Laplacian, Eqn. (5.22), using Green's functions, where

$$U_1(x,t) = \frac{2}{\pi^{3/2}}\int_0^\infty \left.\frac{\partial U_0}{\partial x}\right|_{x=\xi} \frac{d\xi}{x-\xi}\,, \tag{5.77}$$

which are the same outer velocity forms as used by Peace and Riley (1983).

5.2.5 Specification of Asymptotic Time Limits

Utilization of the asymptotic series permits the vortex system velocity field to evolve from the non-physical discontinuities produced by the initiation of a pair of point vortices approaching an inviscid wall boundary into a more physical, unsteady, fully viscous system. Since this study (Section 5.1) has shown that the viscous zones in the vortex cores can be represented initially by Oseen vortices acting independently, the wall boundary layer region is the only viscous zone which demands special care.

The initial velocity field, provided as starting conditions for the Navier-Stokes numerical simulation, corresponds to the maximum time allowed for the asymptotic expansion representation. By choosing small values for the upper asymptotic time limit — say t_{max} — the expansions are very accurate representations of an Navier-Stokes exact solution. However, that accuracy is lost if the viscous boundary layer, at t_{max}, is so thin that it spans only one or two vertical grid points in the finite difference mesh used subsequently to compute the numerical simulation for extended times. Consequently, a suitable compromise was made between minimizing round off errors in the asymptotic representations and maximizing the evolution time of the viscous boundary layer zone represented by the expansions. This study has shown (in Chapter 4) that viscous zones on the order of ten percent of the vortex core radius (corresponding to a dimensionless height of 0.02) can be resolved adequately by the numerical grid. That was the primary motivation for developing the asymptotic solutions.

Selection of t_{max} is similar to establishing an infimum for the asymptotic solution which is simultaneously a supremum for the initial time representation of the numerical simulation. The minimum time required in the asymptotic solution can be estimated in

terms of the desired initial boundary layer thickness for the numerical problem. If y^* is a measure of the boundary layer thickness when the asymptotic solution is terminated, and the numerical computation is initiated, then in order to allow the computational grid to resolve the ground boundary region, y^* must satisfy

$$10^{-1} r_c \leq y^* = \epsilon \eta^* = \sqrt{t/Re}\, \eta^* \ , \tag{5.78}$$

where η^* is the inner parameter at the edge of the ground boundary layer.

While Eqn. (5.78) gives the lower bound for t required by the numerical solution, the upper bound on time is required from the truncation error limits on the asymptotic expansions. Since larger Reynolds numbers in this problem allow the expansion in terms of ϵ to contain smaller truncation errors (at the same time level), the limitation is imposed on the time-series expansions. Hence, dimensionless time must satisfy

$$t \ll 1 \, , \tag{5.79}$$

to assure accuracy in the time-series expansions.

Combining the above two conditions bounds t by:

$$\left(10^{-1} r_c / \eta^*\right)^2 Re \leq t \ll 1 \, . \tag{5.80}$$

Because the first order vorticity field is a function of $exp(-\eta)$, $\eta^* \sim 10$ can be the nominal edge of the boundary layer, where the vorticity is zero to within computational accuracy. With $r_c = 0.2$, the numerics require

$$t \geq O\left(10^{-6} Re\right) , \tag{5.81}$$

which means that because large Reynolds numbers correspond to thin boundary layers, the required minimum asymptotic time must be larger to enable the viscous flow to develop

far enough for a "thick" boundary layer to exist prior to applying numerics. Since t must be much smaller than 1, the method can only accommodate Reynolds numbers on the order of 10^5.

The fact that higher Reynolds number flows need finer grid resolution is also shown in Eqn. (5.81). For example, if the grid resolution can accommodate $10^{-2}r_c$ near the ground, Eqn. (5.81) becomes

$$t \geq O(10^{-7}Re)\,, \tag{5.82}$$

and then the asymptotic solution can be used for the case of Reynolds number as high as 10^6. Therefore, as is always the case, the finer the grid, the higher the allowable Reynolds number. While this statement may sound trite, it is noted that a 10 fold increase in grid resolution in both directions would permit a 10 fold increase simulation Reynolds number. A B-747 simulation, which has a circulation Reynolds number at the order of 10^7, would require a 15,000×30,000 grid if the current type of grid was used.

It is also important to realize that the asymptotic analysis can be used to start a turbulent (high Reynolds number) vortex system since the boundary layer region evolves very quickly through a laminar stage before becoming turbulent.

To summarize, the asymptotically generated velocity field which constitutes the initial velocity distribution in the numerical scheme is a combination of solutions (5.2), (5.3), (5.4), (5.6) and (5.9), where term by term functional solutions to the various series expansions have been developed in this chapter. Small values of time, compared with the time scale of the problem, have been employed to permit truncation of the series. The

asymptotic solution time level, selected to generate the initial numerical velocity field, depended on the circulation Reynolds number, but it was restricted to the maximum time allowable by the finite term approximations to the infinite series expansions. The asymptotic solutions were thus used to produce an initial velocity field whose local gradients could be accommodated by the numerical grid, but those series representations did not require a significant amount of computational overhead. Hence, the approach has enabled substantially higher Reynolds number flows to be investigated without employing the ultra-fine grids that would be required normally for flow initialization.

In order to show the behavior of the initial solutions developed in this chapter, line contours of the vorticity field near the ground plane have been plotted in Figures 5.3–5.5. The calculations for both the analytical solutions and the first numerical step solutions were performed on the 150×300 grid developed in Chapter 4. Since the purpose of the asymptotic solutions is to provide an acceptable initial flow field for the numerical solutions of the vortex system, the outer vertical length scale was used as the y-direction variable in these figures. The circulation Reynolds number, $Re = 1,000$ and the initial vortex position $x_0 = 1$, $y_0 = 2$ (with the symmetry plane at $x = 0$) were used in these cases.

The vorticity contours produced from the asymptotic solution are shown after an initial dimensionless time of t=0.01 in Figure 5.3 and t=0.1 in Figure 5.4. It can be seen that at t=0.01, a strong but very thin ground boundary layer has been developed. That means that during the small time interval, the ground boundary layer has very strong velocity gradients within a thin layer. This illuminates the difficulty for a numerical grid in resolving the initial flow field numerically if the evolution time of the asymptotic

solution is not long enough to produce a resolvable ground boundary layer. At the later time of t=0.1, the strength of the vorticity field has decreased and the thickness of the boundary layer has increased. With the current grid (150×300), there are about ten grid points included in the ground boundary layer at t=0.1. Only two to three vertical grid points are included in the boundary layer at t=0.01, which is insufficient for the resolution by the numerical scheme near the ground. Numerical results, produced after terminating the asymptotic solution at t=0.1 (then providing those results as the initial conditions) and marching one dimensionless time step with $\Delta t = 0.01$, are shown in Figure 5.5, where no abrupt change can be seen in comparison with Figure 5.4. That shows that the numerical scheme can be implemented after the initial ground boundary layer has become thick enough for resolution by the numerical grid.

The velocity profiles at different lateral positions, produced by the asymptotic solutions at t=0.1, are shown in Figure 5.6 to check the flow field matching between the inner solutions and the outer solutions, with the same flow case and the grid as in Figure 5.4. The composite velocity solutions for the ground boundary layer are switched to the outer solution at a vertical distance of $y = 0.13$, where $\eta = 6.5$ for this flow case. Very smooth matching is shown in Figure 5.6.

It is also noted that in the asymptotic solution predictions, the separation point, where the ground vorticity $\zeta = 0$, can only occur as the lateral distance $x \rightarrow \infty$. Since the asymptotic expansion technique cannot predict direct viscous interaction between the ground boundary and the vortex system, the separation phenomenon causing vortex rebound (which will be discussed in Chapter 7) cannot be predicted by this method.

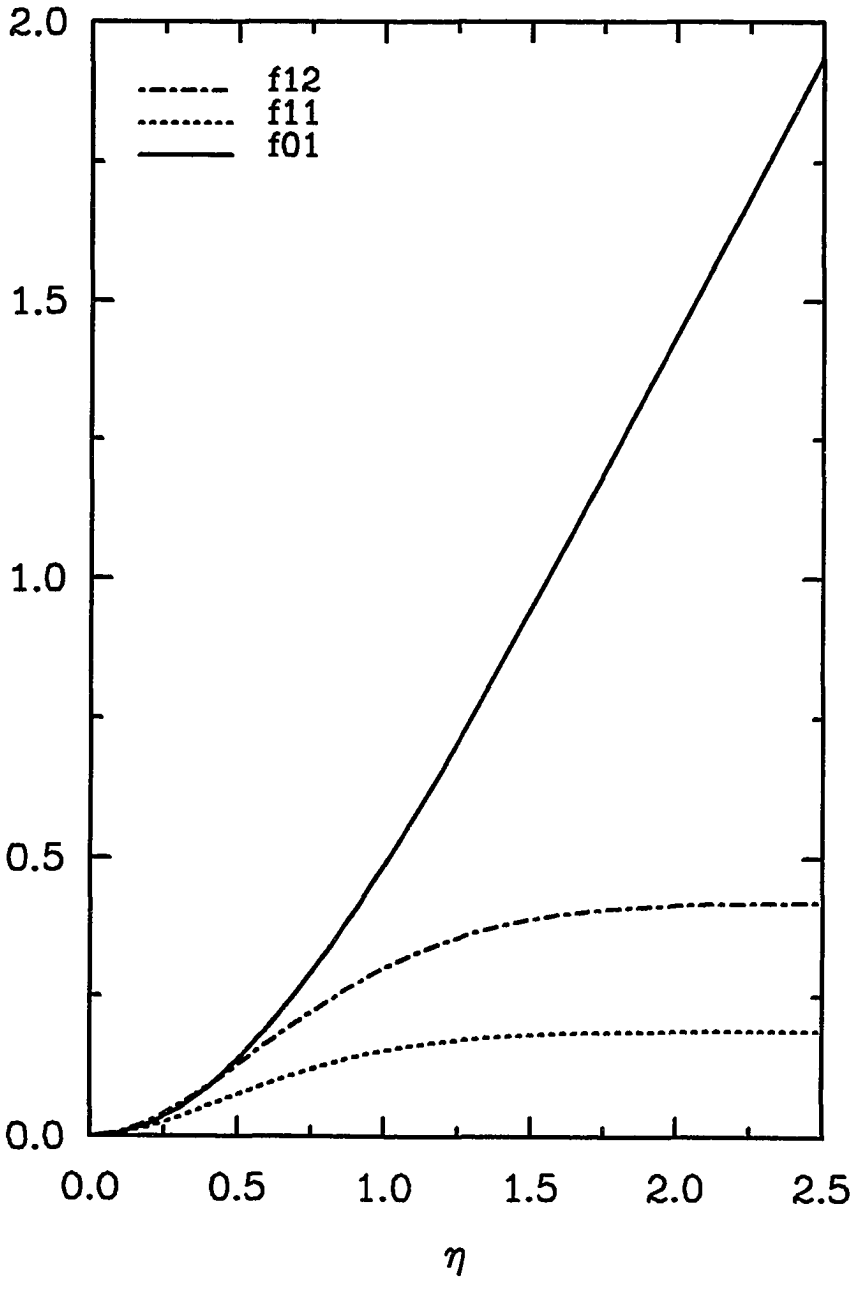

Figure 5.1 Behavior of the first order similarity functions

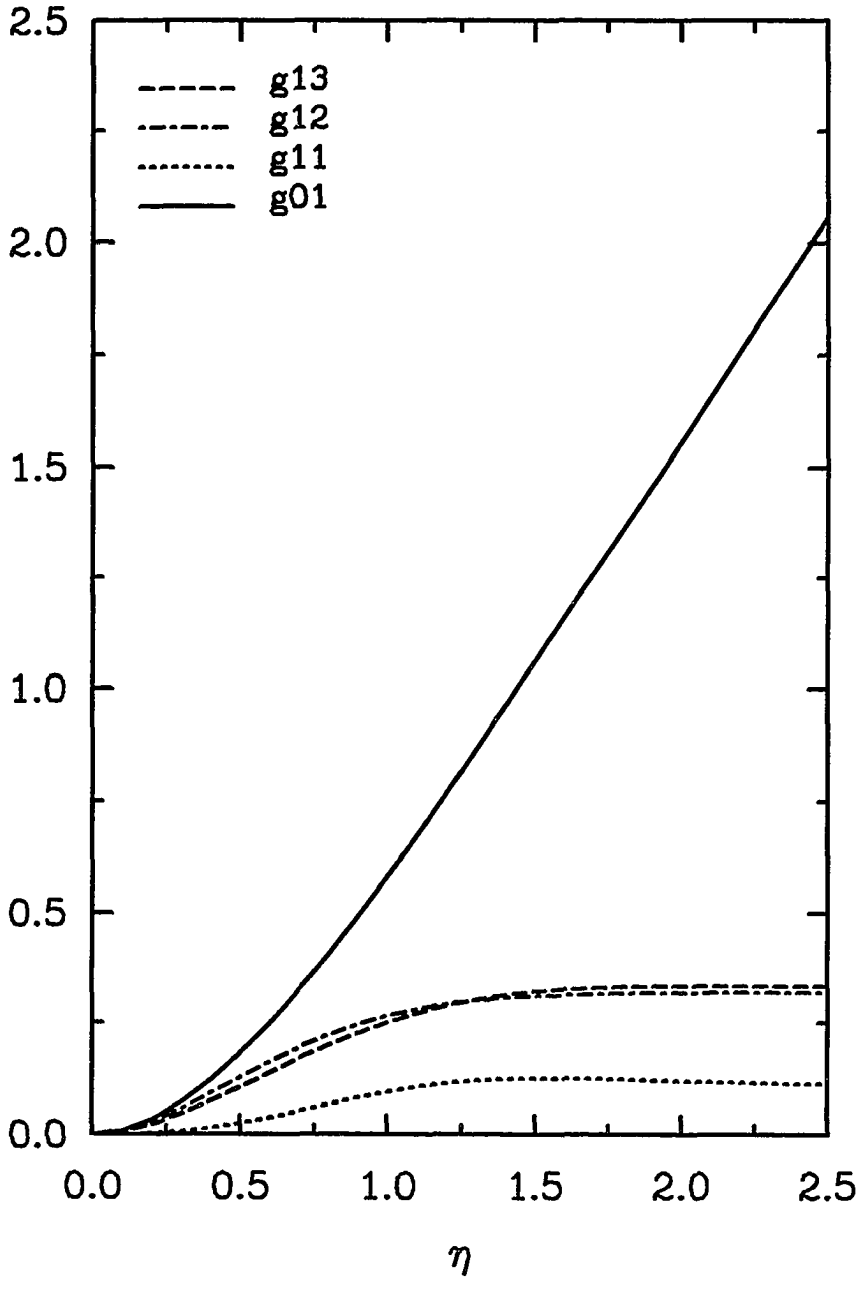

Figure 5.2 Behavior of the second order similarity functions

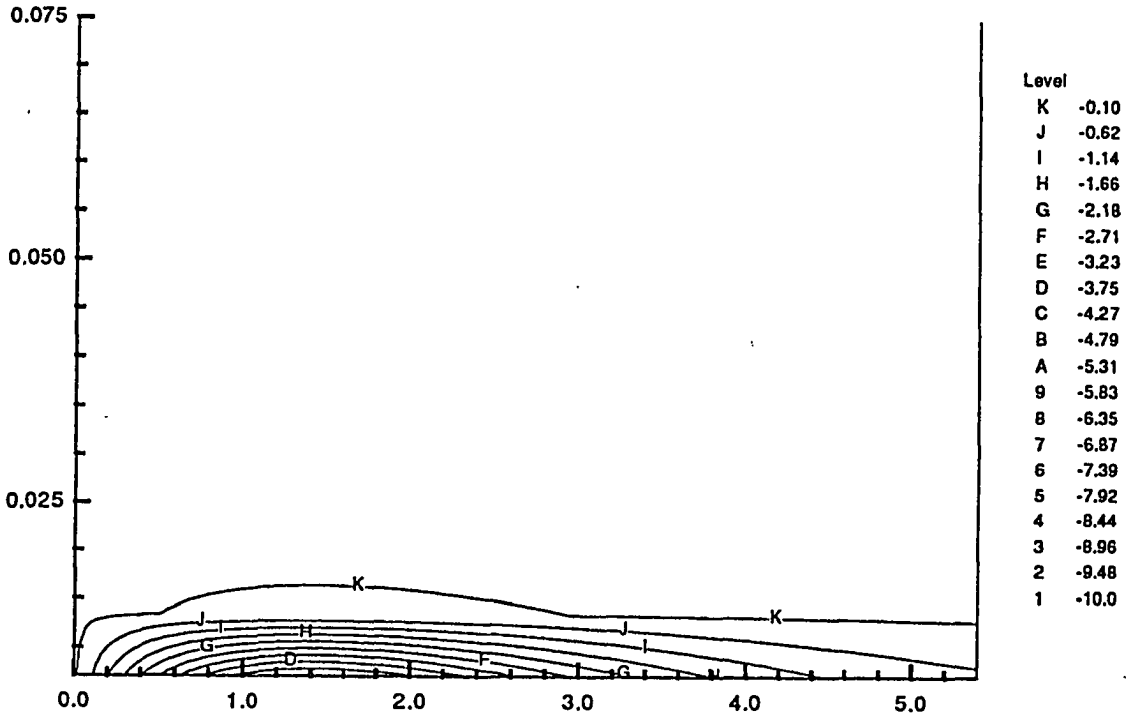

Figure 5.3 Vorticity contours of the asymptotic solutions near the ground boundary layer at t=0.01, with Re=1,000

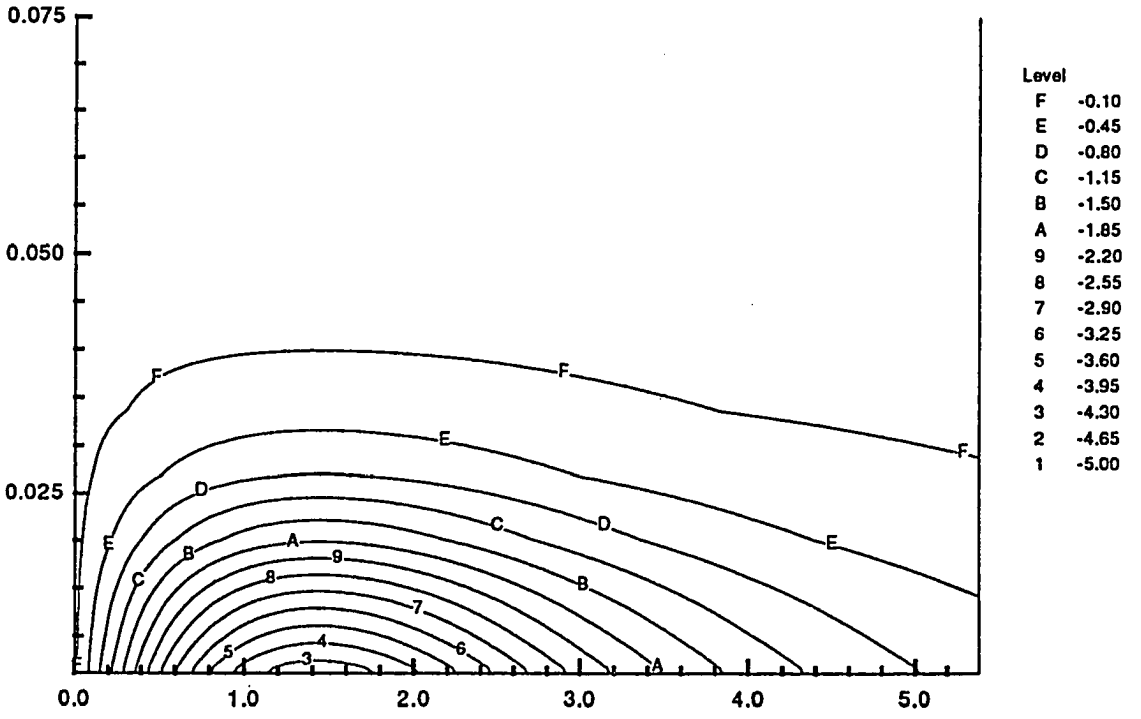

Figure 5.4 Vorticity contours of the asymptotic solutions near the ground boundary layer at t=0.1, with *Re*=1,000

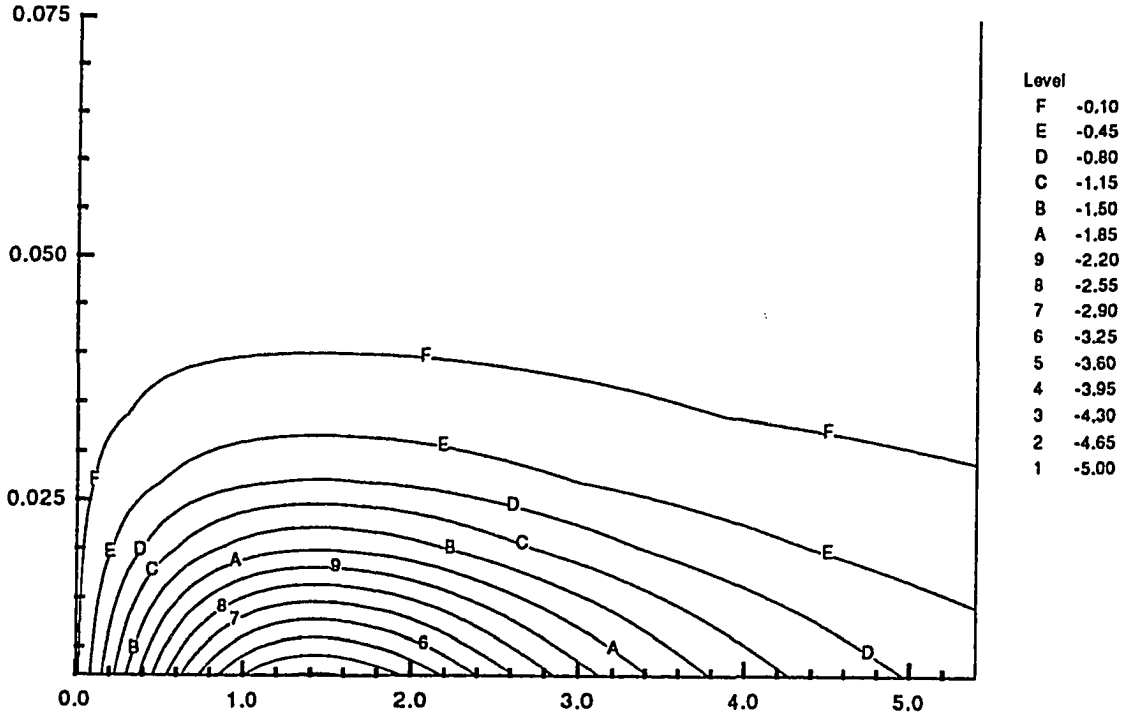

Figure 5.5 Vorticity contours produced by the N-S numerical computation near the ground boundary layer after one time-step Δt=0.01, based upon the asymptotic initial flow field at t=0.1, with *Re*=1,000

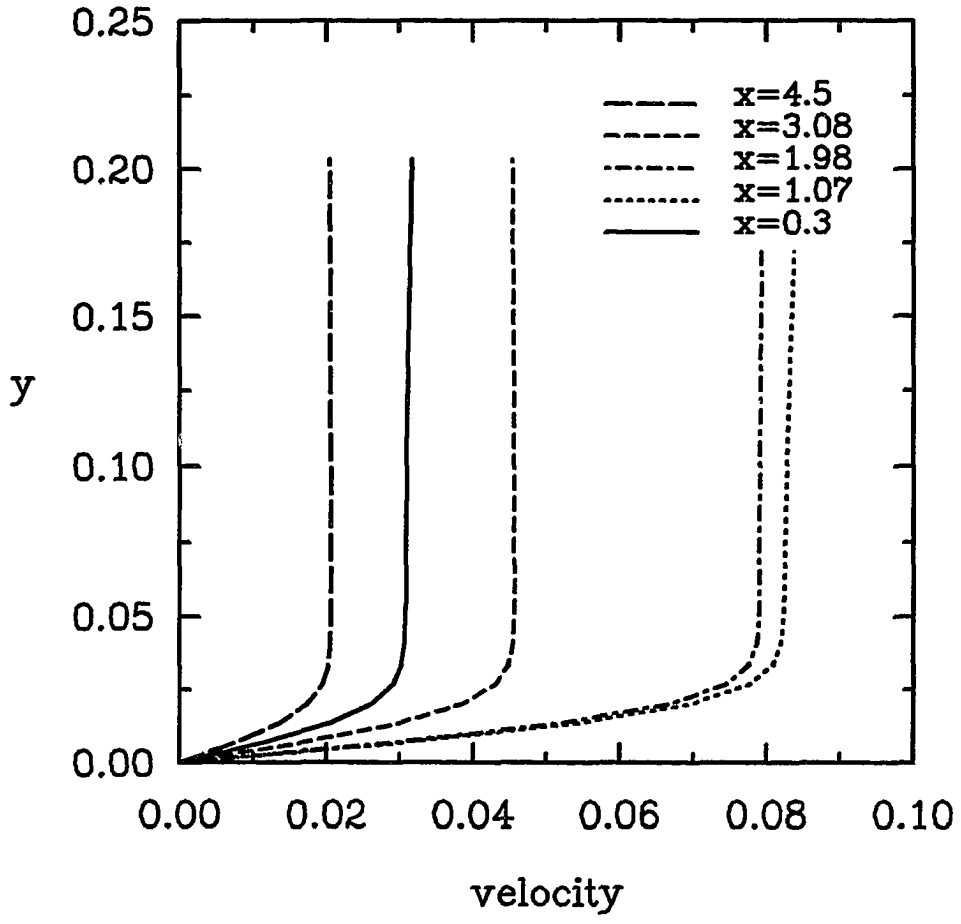

Figure 5.6 Velocity profiles of the asymptotic solutions near the ground boundary at different lateral positions for t=0.1, *Re*=1,000

Chapter 6 Validation of Turbulence Models for Turbulent Vortex Predictions

In this chapter, the utility of different turbulence models for simulating vortex dominated flows is investigated. Eddy viscosity and full Reynolds stress closure turbulence models in cylindrical coordinates have been tested. Studies have focused on the non-physical problem of an isolated vortex in an infinite medium for which the mean axial and radial velocities are zero and the mean tangential velocity distribution is assumed to vary with radius and time. As expected, this study has shown that neither algebraic nor k-ϵ models are capable of handling the curvature effects and turbulent-non-turbulent interfaces associated with vortex cores. In addition, the study has shown that the Reynolds stress model results are in good agreement with the predictions of Donaldson (1972a) and the experimental results of Hoffmann and Joubert (1963). Therefore, the Reynolds stress closure model has been implemented for the present vortex/ground-plane interaction studies.

In the computations of all the turbulence model cases, the two-dimensional, axisymmetric problems were discretized using an implicit, forward-temporal difference, central-spatial difference scheme. A numerical grid was developed using the same exponential transformation in the radial direction to get clustered grid inside the vortex core and stretched the grid to infinity in the physical domain. After the multigrid test, 100 grid points were used in the radial direction with 40 grid points inside the vortex core.

The non-dimensional time marching step was chosen as 0.01. In all the test cases, the Reynolds number, based on the initial maximum swirling velocity and the core radius, was 10,000.

6.1 Description of the Test Problem

Donaldson (1972a) studied the decay of an isolated turbulent vortex in an infinite medium to evaluate his Reynolds stress transport turbulence model. That problem was used also in this study, because it required a minimum amount of computer resources while incorporating streamline curvature and core relaminarization effects. The test problem was run in cylindrical coordinates, even though the ground-plane interaction problem is not amenable to a cylindrical coordinate formulation.

Assuming the mean velocity components are U=W=0, and V=V(r,t), where U and W are the radial and axial mean velocity components and V is the azimuthal velocity, the azimuthal component of the Navier-Stokes equations for an incompressible, isothermal turbulent flow reduces to:

$$\frac{\partial V}{\partial t} = \frac{\nu}{r}\frac{\partial}{\partial r}\left[r^3\frac{\partial(V/r)}{\partial r}\right] - \frac{1}{r^2}\frac{\partial}{\partial r}\left(r^2\,\overline{uv}\right), \tag{6.1}$$

where u,v,w are the fluctuating velocity components in the corresponding coordinate directions and $\overline{uv}$ is a time averaged Reynolds stress. Hence, the prototype turbulent vortex decay problem reduces to finding V=V(r,t) and $\overline{uv} = \overline{uv}\,(r,t)$, subject to initial conditions:

$$V\,(r,0) = V(r), \tag{6.2}$$

and

$$\overline{uv}\,(r,0) = f(r) \tag{6.3}$$

with boundary conditions

$$\lim_{r \to 0} |V(r,t)/r| = \text{ constant} \tag{6.4}$$

$$\lim_{r \to 0} \overline{uv}(r,t) = 0, \tag{6.5}$$

and

$$\lim_{r \to \infty} V(r,t) = 0, \tag{6.6}$$

with

$$\lim_{r \to \infty} \overline{uv}(r,t) = 0. \tag{6.7}$$

Depending on the turbulence model, the Reynolds stress initial and boundary conditions can be trivial. The initial mean velocity distribution, chosen for this study, was the laminar profile developed by Oseen (1911), which can be written for some arbitrary time $t = r_c^2/4\nu$, as

$$V(r, t = r_c^2/4\nu) \equiv V(r,0) = \frac{\Gamma_\infty}{2\pi r}\left[1 - e^{-(r/r_c)^2}\right], \tag{6.8}$$

which is an instantaneous solution to the Navier-Stokes equations, when $\overline{uv} = 0$. That solution includes a rigid rotating core, with a far-field circulation level of Γ_∞. If the vortex core radius, $r^*(t)$, is defined by:

$$V(r^*, t) = V_{max}(t), \tag{6.9}$$

the initial vortex core radius, r_o, is imposed from Eqn. (6.8) as $r_o/r_c \equiv \gamma$, where γ is a solution to the transcendental equation:

$$1 + 2\gamma^2 = e^{\gamma^2}, \tag{6.10}$$

and is approximately 1.122. The maximum initial velocity was designated V_o $(= V_{max}(0))$.

Since the simulation has been initialized with a laminar velocity profile, it was assumed that the initial Reynolds stress distribution was zero. When required, initial time averaged turbulent kinetic energy components were not set equal to zero. The assumed initial kinetic energy components were taken from Donaldson and Sullivan (1971) and were:

$$\overline{u^2}\,(r,0) = h(\hat{r})\left(1 - e^{-\gamma^2\hat{r}^2}\right)/(\gamma^2\,\hat{r}^2)\,, \tag{6.11}$$

$$\overline{v^2}\,(r,0) = h(\hat{r})\,e^{-\gamma^2\hat{r}^2}, \tag{6.12}$$

and $$\overline{w^2}\,(r,0) = \left[\overline{u^2}(r,0) + \overline{v^2}(r,0)\right]/2, \tag{6.13}$$

where $h(\hat{r})$ is a function of dimensionless coordinate $\hat{r}$ $(= r/r_o)$ which must be specified. They assumed $h(\hat{r})$ was in the form $c\exp(-\gamma^2\hat{r}^2)$ which causes the initial maximum kinetic energy to occur along the vortex axis. A slightly different form has been chosen in this study:

$$h(\hat{r}) = c\,\hat{r}^2 e^{-\gamma^2\hat{r}^2}\,, \tag{6.14}$$

which causes the initial kinetic energy maximum to occur near the vortex core boundary $(\hat{r} = 1)$. Therefore, the initial kinetic energy distribution was assumed to be:

$$k\,(r,0) = \frac{3}{4}\,c\,e^{-\gamma^2\hat{r}^2}\left[\frac{1 - e^{-\gamma^2\hat{r}^2}}{\gamma^2} + \hat{r}^2 e^{-\gamma^2\hat{r}^2}\right]. \tag{6.15}$$

All other initial conditions were for non-physical turbulence quantities and will be discussed when they are required by the particular turbulence model.

Now the evolution of the initial laminar mean velocity profile into a turbulent profile is not physical — even using the Reynolds stress transport model. Furthermore, the

vortex-ground plane problem required a similar transition to turbulence, and the possibility was concerned that different prescribed initial turbulent kinetic energy distributions might produce different evolved mean velocity profiles. Tests were conducted with the Reynolds stress transport model for the isolated vortex to see if initial locations of the kinetic energy maximum (holding the maximum kinetic energy level at 0.26 percent) altered the evolved velocity profile. Tests were run with the initial kinetic energy peak located at $\hat{r} = 0, 1, 2$ and 3. As shown in Figure 6.1, those tests showed that both the mean velocity and Reynolds stress quantities were nearly identical after dimensionless times of 100 (100 r_o/V_o). That time interval was also the typical time required for start-up transients to disappear, in agreement with Donaldson (1972a).

The insensitivity of the evolved turbulent distributions is due primarily to the low levels of initial turbulent energy quantities, in comparison with the mean flow. Even though changes in the mean velocity profiles were observable as time increased, those changes were due more to extraction of energy from the initial mean profiles than to variations in the initial distributions of turbulent quantities.

The discussion which follows is intended to summarize briefly the forms of the various turbulence models tested in this study. The formulation and, in some cases, optimization of turbulent model constants was not part of the study.

6.2 Zero-Equation Eddy Viscosity Model

The simplest turbulence model was to use *ad hoc* assumptions consistent with Prandtl's original mixing length theory, so that

$$-\overline{uv} \approx \nu_t \left(\frac{\partial V}{\partial r} - \frac{V}{r} \right) = \nu_t \dot{\epsilon}_{r\theta} \, , \tag{6.16}$$

where ν_t is an eddy viscosity, and $\dot{\epsilon}_{r\theta}$ is the mean strain rate component. The eddy viscosity was assumed related to a mixing length, l, through

$$\nu_t = l^2 \, |\dot{\epsilon}_{r\theta}| . \tag{6.17}$$

Ragsdale (1961) used both Prandtl functions and von Karman similarity functions to model turbulence vortex systems with zero-equation models, but his predictions did not agree well with experiments. Here, it has been assumed that mixing length was a constant, related directly to the initial vortex core radius, i.e.

$$l = \eta \, r_o \, , \tag{6.18}$$

with η = 0.1. Thus, it has been decided to take the trivial step of approximating a turbulent vortex as a more viscous laminar vortex. Later, a comparison of turbulent results with the prediction of a laminar vortex system in ground effect has shown that a simple algebraic eddy viscosity approximation, though obviously restrictive, may be as good as some of the more complicated eddy viscosity models.

6.3 One-Equation Eddy Viscosity Model

The turbulent kinetic energy equation can be derived by taking the inner product of the fluctuating momentum equations with the fluctuating velocity vector and averaging over a suitable time. For the present system, that equation can be simplified to:

$$\frac{\partial k}{\partial t} = \frac{\nu}{r}\frac{\partial}{\partial r}\left(r\frac{\partial k}{\partial r}\right) - \frac{1}{r}\frac{\partial}{\partial r}\left[\frac{\overline{rup}}{\rho} + \overline{ruk}\right] - \epsilon \tag{6.19}$$

where $k = \frac{1}{2}\overline{u_i u_i}$, and ϵ is the isotropic, turbulent dissipation and is the cylindrical coordinate representation of the Cartesian tensor contraction $\epsilon = \overline{\left(\frac{\partial u_i}{\partial x_i}\right)^2}$. Here, the

kinetic energy transport equation has been modeled as

$$\frac{\partial k}{\partial t} = \frac{1}{r}\frac{\partial}{\partial r}\left[\left(\nu + \frac{\nu_t}{\sigma_k}\right) r \frac{\partial k}{\partial r}\right] + \nu_t r^2 \left[\frac{\partial (V/r)}{\partial r}\right]^2 - \epsilon\,, \tag{6.20}$$

where the turbulent dissipation was approximated by

$$\epsilon = c_D \frac{k^{3/2}}{r_o}, \tag{6.21}$$

and σ_k is a turbulent kinetic energy Prandtl number, taken to be unity. It has been assumed that the eddy viscosity is given by:

$$\nu_t = c_k \, l \, k^{1/2} \tag{6.22}$$

with l still approximated from Eqn. (6.16), and constants c_D and c_k both taken to be unity.

6.4 Two-Equation Eddy Viscosity Model

Using the standard k-ϵ model of Launder and Spalding (1974), the governing equation for isotropic turbulent dissipation, ϵ, simplifies to:

$$\frac{\partial \epsilon}{\partial t} = \frac{\epsilon}{k} c_1 \nu_t r^2 \left[\frac{\partial}{\partial r}(V/r)\right]^2 + \frac{1}{r}\frac{\partial}{\partial r}\left[r\left(\nu + \frac{\nu_t}{\sigma_\epsilon}\right)\frac{\partial \epsilon}{\partial r}\right] - c_2 \frac{\epsilon^2}{k} \tag{6.23}$$

where constants c_1 and c_2 were taken to be Launder and Spalding's values of 1.44 and 1.92, respectively and the dissipation Prandtl number, σ_ϵ, was assigned their value of 1.3. In this case, the eddy viscosity was assumed given by

$$\nu_t = c_\mu \, k^2/\epsilon\,, \tag{6.24}$$

with c_μ=0.09.

6.5 Reynolds Stress Transport Equations

The Cartesian tensor form of the Reynolds stress transport equations can be written employing index notation, utilizing the summation convention as:

$$\frac{D\overline{u_i u_j}}{Dt} = -\overline{u_k u_i}\frac{\partial U_k}{\partial_{xj}} - \overline{u_k u_j}\frac{\partial U_i}{\partial x_k} - \frac{\partial}{\partial x_k}\overline{u_i u_j u_k} - \frac{1}{\rho}\left[\frac{\partial \overline{pu_j}}{\partial x_i} + \frac{\partial \overline{pu_i}}{\partial x_j}\right] + \frac{1}{\rho}\overline{p\left(\frac{\partial u_i}{\partial x_j} + \frac{\partial u_j}{\partial x_i}\right)} + \nu\frac{\partial^2}{\partial x_k^2}\overline{u_i u_j} - 2\nu\overline{\frac{\partial u_i}{\partial x_k}\frac{\partial u_j}{\partial x_k}} \quad . \tag{6.25}$$

Donaldson (1972a) has used invariant modeling to model the terms in the six equations, represented by Eqn. (6.24), for Reynolds stresses in cylindrical coordinates. The cylindrical coordinate representations of the modeled Reynolds stress transport equations are long and can be found in Donaldson's article.

Assuming length scale, $\Lambda(t)$, varies with instantaneous vortex core radius, $r^*(t)$, defined in Eqn. (6.9), it was assumed that

$$\Lambda = 0.16\, r^*(t)\,, \tag{6.26}$$

and Donaldson's scale factor M was defined by:

$$M = \Lambda\left(\overline{u^2} + \overline{v^2} + \overline{w^2}\right)^{1/2}, \tag{6.27}$$

so that the following terms were modeled:

$$\overline{u^3} = -3M\frac{\partial \overline{u^2}}{\partial r} \tag{6.28}$$

$$\overline{v^3} = -6M\frac{\overline{uv}}{r}\,, \tag{6.29}$$

$$\overline{u^2 v} = -2M\left[\frac{\partial \overline{uv}}{\partial r} - \frac{\overline{uv}}{r}\right]\,, \tag{6.30}$$

$$\overline{uv^2} = -M\left[\frac{\partial \overline{v^2}}{\partial r} + \frac{2}{r}\left(\overline{u^2} - \overline{v^2}\right)\right]\,, \tag{6.31}$$

$$\overline{uw^2} = -M\frac{\partial \overline{w^2}}{\partial r} \ , \tag{6.32}$$

$$\overline{pu} = -\rho M\left[\frac{\partial \overline{u^2}}{\partial r} + \frac{\overline{u^2} - \overline{v^2}}{r}\right] , \tag{6.33}$$

$$\overline{pv} = -\frac{\rho M}{r^2}\frac{\partial r^2 \overline{uv}}{\partial r} \ , \tag{6.34}$$

$$\overline{p\frac{\partial u}{\partial r}} = -\rho M\frac{2\overline{u^2} - \overline{v^2} - \overline{w^2}}{6\Lambda^2} \ , \tag{6.35}$$

$$\overline{p\frac{\partial v}{\partial \theta}} = \rho M\left[\frac{\partial \overline{u^2}}{\partial r} + \frac{\overline{u^2} - \overline{v^2}}{r} - \frac{2\overline{v^2} - \overline{u^2} - \overline{w^2}}{6\Lambda^2} r\right] , \tag{6.36}$$

$$\overline{p\frac{\partial w}{\partial z}} = -\rho M\frac{2\overline{w^2} - \overline{u^2} - \overline{v^2}}{6\Lambda^2} \ , \tag{6.37}$$

$$\overline{\left(\frac{\partial u}{\partial r}\right)^2} + \frac{1}{r^2}\overline{\left(\frac{\partial u}{\partial \theta}\right)^2} + \overline{\left(\frac{\partial u}{\partial z}\right)^2} + 2\overline{\frac{u}{r^2}\frac{\partial v}{\partial \theta}} + \frac{\overline{u^2}}{r^2} = -\frac{\overline{u^2}}{\lambda^2} + \frac{\overline{u^2} + \overline{v^2}}{r^2} \ , \tag{6.38}$$

$$\overline{\left(\frac{\partial v}{\partial r}\right)^2} + \frac{1}{r^2}\overline{\left(\frac{\partial v}{\partial \theta}\right)^2} + \overline{\left(\frac{\partial v}{\partial z}\right)^2} + \frac{\overline{v^2}}{r} - \frac{2}{r}\overline{v\frac{\partial u}{\partial \theta}} = \frac{\overline{v^2}}{\lambda^2} + \frac{\overline{v^2} - \overline{u^2}}{r^2} \ , \tag{6.39}$$

$$\overline{\left(\frac{\partial w}{\partial r}\right)^2} + \frac{1}{r^2}\overline{\left(\frac{\partial w}{\partial \theta}\right)^2} + \overline{\left(\frac{\partial w}{\partial z}\right)^2} = \frac{w^2}{\lambda^2} \ , \tag{6.40}$$

and $$\overline{\frac{\partial u}{\partial r}\frac{\partial v}{\partial r}} + \frac{1}{r^2}\overline{\frac{\partial u}{\partial \theta}\frac{\partial v}{\partial \theta}} + \overline{\frac{\partial u}{\partial z}\frac{\partial v}{\partial z}} + \frac{\overline{uv}}{r^2} = \frac{\overline{uv}}{\lambda^2} + 2\frac{\overline{uv}}{r^2} \ , \tag{6.41}$$

where

$$\lambda \equiv \Lambda/\left(C_\alpha + C_\beta R_{e_\Lambda}\right)^{1/2} \tag{6.42}$$

with

$$Re_\Lambda \equiv \frac{(2k)^{1/2}\Lambda}{\nu} \ . \tag{6.43}$$

Constants C_α and C_β were assigned values of 2.5 and 0.125, respectively.

6.6 Test Problem Results

Mean velocity profiles for the three eddy viscosity models and the Reynolds transport model are shown in Figure 6.2 for isolated vortex decay after time intervals of (a) 100 r_o/V_o and (b) 200 r_o/V_o, where V_o was the initial maximum vortex core velocity. The Reynolds number for this problem was defined as the initial core Reynolds number, $R_e=V_o r_o/\nu=10{,}000$. The Reynolds stress transport calculations agree with Donaldson (1972a), and with the experimental results of Hoffmann and Joubert (1963) for time equal to 200 r_o/V_o (Figure 6.3). Hence, the simulation is relatively insensitive to the initial kinetic energy distribution, as mentioned previously.

While the test vortex cannot be produced in a laboratory, it is expected that the mean velocity profile history will be similar to physically realizable turbulent vortices. Two interrelated aspects of the velocity history are considered to be very important attributes, required from a successful turbulence model. The maximum swirl velocity should decrease more slowly with time than a laminar vortex with increased viscosity and the vortex core should dilate more slowly. Since rapid core dilation must be accompanied by a corresponding decrease in maximum swirl velocity to conserve angular momentum, failure to capture those effects will result in overly optimistic predictions for the rate of vortex decay. As can be seen in Figure 6.2, the eddy viscosity models have all predicted mean velocity histories which are considered to have excessive viscous diffusion. While these results were not surprising, it is worth noting that the zero-equation model performed about as well as all of the other non-Reynolds stress transport models. However, it was determined that a Reynolds stress transport model was necessary for simulating the

aircraft wake-ground plane interaction problem, since excessive dissipation would result in underestimation of the importance of wake vortices near airports.

Some other interesting properties of the Reynolds stress transport model can be seen in Figure 6.3. Since there was a wake type axial flow in Hoffman and Joubert's experiment (1963) and the computational prediction agrees with their experimental data so well, the agreement means means that at least for turbulent diffusion processes, the axial flow may not exert a significant influence. This may legitimize using two-dimensional models to calculate vortex wake decay, as long as three-dimensional effects, such as vortex breakdown and Crow (1970) instability, are not important. When compared with the laminar velocity profile, the Reynolds stress transport predictions show that inside the vortex core, the results are almost the same as the laminar case and the turbulent behavior appears in the shear layer, outside of the vortex core. The relaminarization inside the vortex core is thus exhibited using the Reynolds stress transport model prediction.

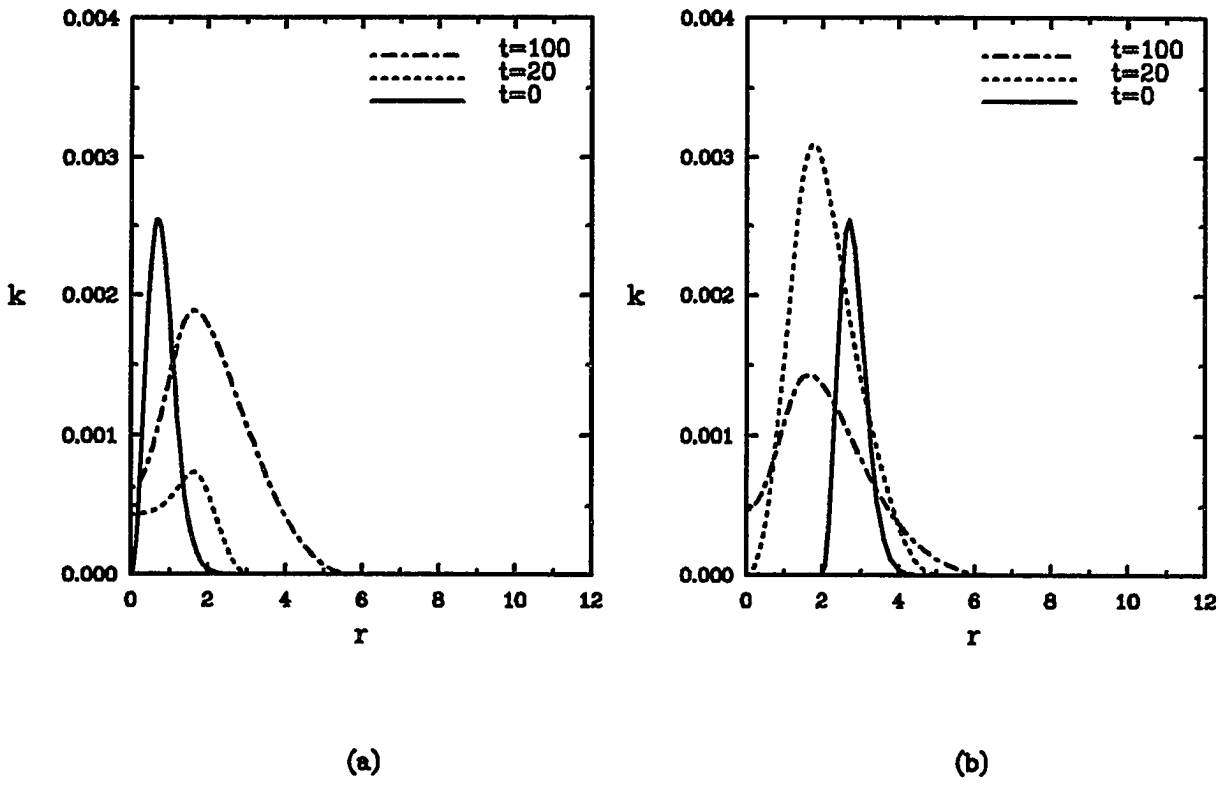

Figure 6.1 Influence of initial kinetic energy distribution on the evolution of kinetic energy (a) $\hat{r} = 1$, (b) $\hat{r} = 3$, ($k_{max} = 0.0026$)

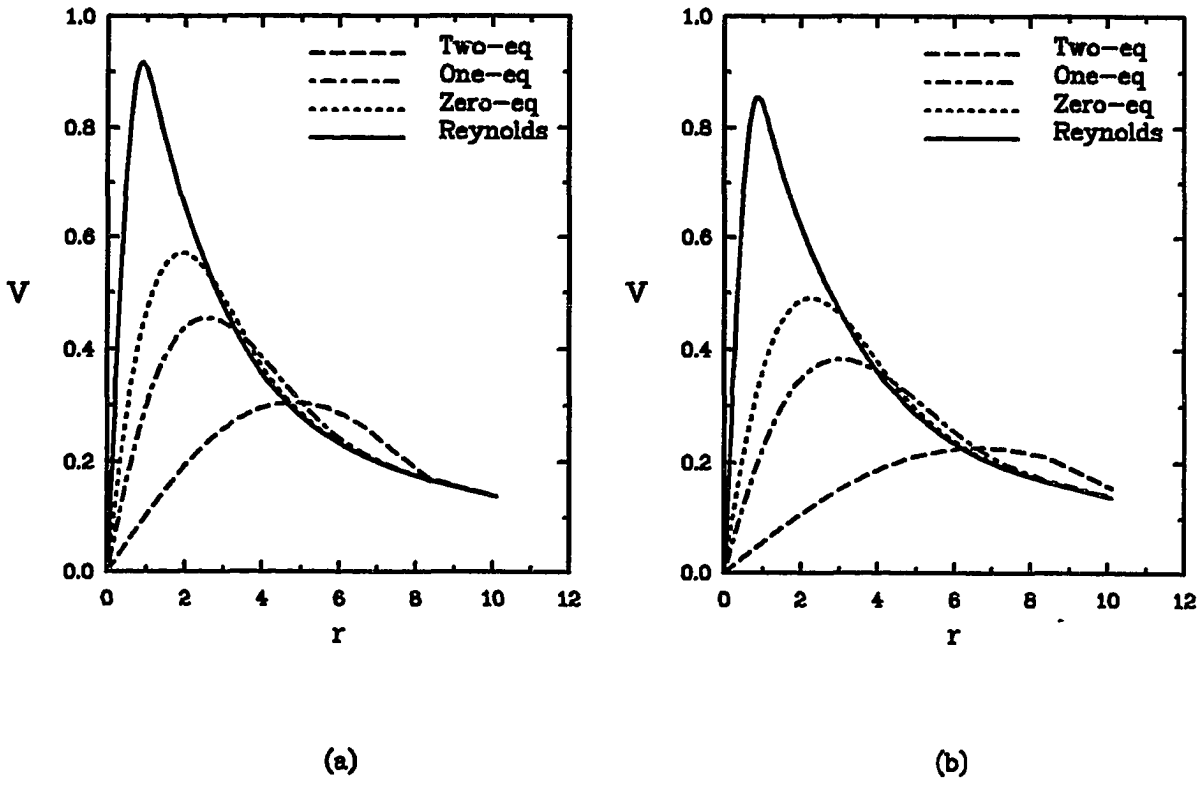

Figure 6.2 Comparison of predicted mean velocity profiles using different turbulence models (a) t=100, (b) t=200

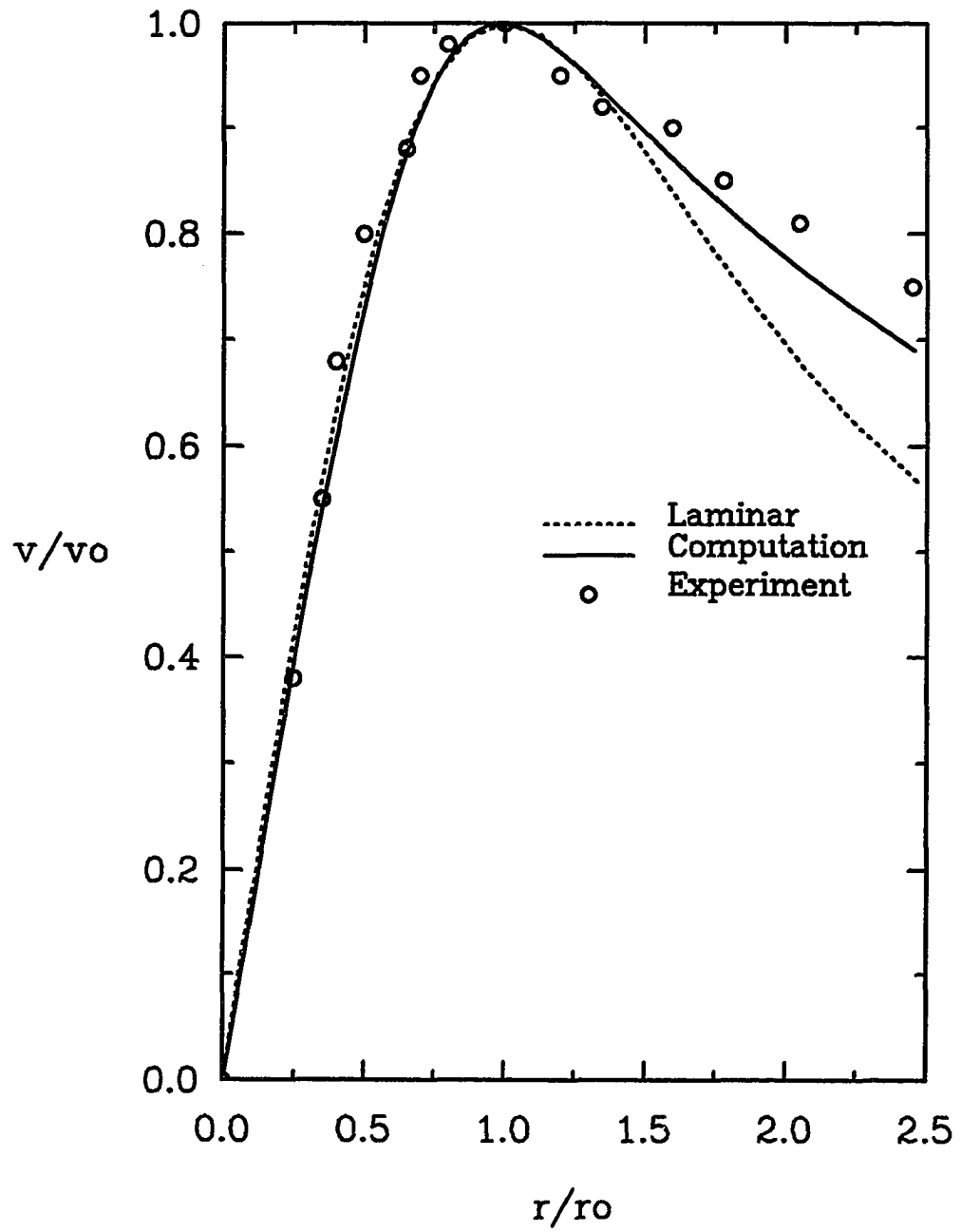

Figure 6.3 Comparison of predicted turbulent vortex mean velocity profile with experimental measurements of Hoffmann and Joubert (1963), along with laminar velocity profile, at t=200, Re=10,000

Chapter 7 Influence of Reynolds Number

The unstratified, laminar and turbulent flow cases have been simulated over a range of circulation Reynolds numbers, to assess the influence of viscous effects on vortex trajectories and strengths near the ground. Invoking symmetry of the vortex pair (without cross wind) permits the computations to be restricted to the first quadrant ($0 \leq x < \infty$, $0 \leq y < \infty$). Equations (3.41)-(3.44) for the laminar cases and equations (3.64)-(3.73) for the turbulent cases, with all the density departure terms set to zero, were used in the study reported in this chapter. The laminar cases also served as a validation for the Cartesian version of the computer code, beyond the cylindrical test problem, and good agreement was obtained. Ground rebound mechanisms were revealed by the "snapshots" of the vorticity contours from the computational simulations, which confirmed the scenario suggested by Harvey and Perry (1971). Problems with vortex hazard assessment have been addressed as well.

The upwind-flux-spliting, ADI scheme was used on the 150×300 grid, which was discussed in Chapter 4, with the non-dimensional time marching step Δt=0.01, for all the cases. The calculations were terminated at dimensionless time t=60, when the strengths of the vortex system were small compared with the original vortex system and the vortex cores had started to move out of the fine resolution grid region. For a typical B-747, this time interval is equivalent to one or two minutes.

7.1 Laminar Results and Comparison of Trajectories with Experimental Results

Limited experimental data are available for numerical validation studies. The experiments of Liu and Srnsky (1990) have been used as the principle test case for the behavior of a wake vortex system near the ground. Their vortex flows were produced by towing an NACA 0012 wing model in a water tank and the estimated circulation based Reynolds number (Γ_0/ν) for their most documented flow experiment was 7,650. Their experiments did not investigate stratification and turbulence effects near a ground plane.

The same circulation Reynolds number was used in the present calculations for an unstratified validation test. Figure 7.1(a) represents the vortex trajectories ($x(t)$, $y(t)$) of the numerical simulation, along with the measured trajectory of Liu and Srnsky (1990). The horizontal and vertical time histories, $x(t)$ and $y(t)$, are shown in Figures 7.1(b) and (c), respectively. The agreement between the numerical simulation and the experiment for Re=7,650 is quite good.

In order to study Reynolds number effects on wake vortices near the ground, circulation Reynolds numbers of 1000 and 75,000 were also simulated (as laminar cases). Figure 7.2 shows the predicted trajectories, along with the horizontal and vertical motion histories of the primary vortex for these two cases. Time markers have been placed on the trajectory plots to facilitate comparison.

The higher Reynolds number vortex system traverses a longer path within the same computational time interval, when compared to the Reynolds number path. For the low Reynolds number cases, viscous effects weaken the main vortex system more rapidly, resulting in slower vortex motion in both the lateral and vertical directions. While the

overall motion of the low Reynolds number case is more confined than that for the high Reynolds number case, the vortex rebound near the ground plane occurs earlier for low Reynolds numbers, because the thicker boundary layers, produced at the lower Reynolds numbers, create more extensive separation zones.

7.2 The Vortex Rebound Mechanism

The rebound mechanism can be explained using the instantaneous vorticity contours in Figures 7.3 (a) and (b). The separation point in the ground-plane boundary-layer can be seen clearly in Figure 7.3, at the location where $\zeta = 0$. That separation causes opposite sign vorticity to be induced by the main vortex on the ground, thus forming a secondary vortex. This secondary vortex creates upward motion of the main vortex. Compared with the experimental observations (Figure 2.3), the rebound scenario shown here agrees with the experimental observations of Harvey and Perry (1971), which are becoming widely accepted. The complicated viscous process which occurs during vortex rebound disqualifies the inviscid explanations employed previously to explain the phenomenon. Moreover, it can be seen in the contours that, at least within the circulation Reynolds numbers of this study, neither the effect of finite vortex core size (Barker and Crow, 1977) nor the viscous displacement effect of the no-slip ground boundary (Peace and Riley, 1983) are major factors during vortex rebound. In order to determine whether separation occurs at the low Reynolds number cases, which was a point of contention in Peace and Riley's work (1983), a vortex Reynolds number case of 100 was tested. Even at that Reynolds number, ground boundary separation was found to occur, but the separation zone was very small. Since these very low Reynolds number flows are not relevant to the vortex hazard problem, those results have not been presented here.

Details of this rebound mechanism cannot be resolved when a coarse grid is used at the early stage of the simulation. In addition, the accuracy of the streamfunction solver also influences resolution of the boundary layer separation zone. This may explain why an *ad hoc* ground boundary condition was used by Delisi, Robins and Fraser (1987) to get a proper vortex rebound, while Peace and Riley (1983) did not predict separation in some of their flow cases.

In the discussion here, only the vorticity contours for a circulation Reynolds number of 1000 have been shown. The reason for using this relatively low Reynolds number case as an example is because the higher Reynolds number cases have a very thin ground boundary layer and the separation zone detail cannot be seen clearly on the contour plots. It is also noted that the left hand side of the vorticity color contours were produced by reflecting the right hand plane color image into the left hand plane. That reflection reverses the sign of the vorticity contours represented in the left hand plane, but maitains an accurate shape representation using minimum computer resources.

7.3 The Vortex Hazard Assessment

In order to assess the vortex hazard, some measure of hazard strength was required. However, since the computational domain is an unbounded quadrant, overall or global measures of circulation or velocity levels are of little value. It was decided finally that circulation and kinetic energy histories in the aircraft *approach zone* would be meaningful. The approach zone was defined somewhat arbitrarily as the area bounded by $-2 < x < 2$ and $0 < y < 3$. Since the coordinates have been made dimensionless by the vortex half-span, an horizontal distance of four units is on the order of a runway width, and a three unit height is slightly larger than an airplane wing span. That cross

section was considered to approximate the span of a typical runway entrance. The velocity components and vorticity were thus computed at each grid point within the right half of that area ($0 < x < 2,\ 0 < y < 3$) at each time level. Subsequently, zonal circulation, $\Gamma(2\times3)$, was calculated by integrating the vorticity over that half-area and the instantaneous kinetic energy within the zone, E(2×3), was computed by a similar integration of $\frac{(u^2+v^2)}{2}$. Those histories are shown in Figure 7.4 for the extreme Reynolds number cases (Re=1000 and 75,000). The experiments of Liu and Srnsky (1990) did not report circulation and energy history data, precluding any comparison with experiments.

Figure 7.4 shows that the circulation history for a Reynolds number case of 75,000 decays initially more slowly than the 1,000 Reynolds number case, then its decay rate exceeds the low Reynolds number case at later times. Although slower decay rates for higher Reynolds number cases are expected, the fact that the vortex moves out of the (2×3) rectangular domain causes the higher Reynolds number vortex to exhibit more rapid decay at the later time levels. The kinetic energy history in the region shows the same trend.

These "hazard history" results in the (2×3) region show how hypothetical and somewhat arbitrary methods for addressing the vortex hazard near a single runway become difficult to interpret and use. Since the encountering aircraft type most surely influences the hazard, neither a measure of the total strength of vortex wakes, nor a rational way to interpret vortex hazard exists in that regard.

7.4 Turbulent Vortex Cases

The length scale, given by Eqn. (6.25), must be altered for the vortex-pair/ground-plane interaction problem, because only turbulent regions near the vortex core were considered in Eqn. (6.25). Turbulence regions near the ground must be included here as well and the logic used to introduce boundary layer length scales follows.

Near the ground, von Karman's constant, κ, can be used, where

$$\lim_{y \to 0} \Lambda\,(y,t) = \kappa y\ . \tag{7.1}$$

This form is the limiting viscous layer length scale at the no-slip surface. In the zone containing the vortex pair, it is assumed that

$$\Lambda\,(Y,t) = C_\Lambda X(t) \tag{7.2}$$

where the right-hand vortex center is located at $X(t), Y(t)$, and X is therefore a measure of the instantaneous vortex half-span. These two ideas can thus be incorporated into a continuous distribution:

$$\Lambda = C_\Lambda X[1 - \exp(-\kappa y/C_\Lambda X)]\ , \tag{7.3}$$

which was used with $C_\Lambda = 0.1$ in this study. Prior to this modification, numerical testing had shown that excessive turbulent diffusion was produced when the turbulence length scale did not decrease as the vertical distance of the flow field approached the ground plane.

The initial conditions for the mean-flow variables have been developed in Chapter 5 for vortex ground-plane simulations which avoid anomalous initial velocity gradients

near the ground. Since the unsteady boundary layer evolves through a laminar phase, the asymptotic procedures developed in that chapter apply equally to turbulent initialization.

Gaussian-type distributions were used for the initial turbulent kinetic energy profiles, with

$$k = k_o \, e^{-cr_*^2} \tag{7.62}$$

where

$$r_*^2 = \frac{(x - X_o)^2 + (y - Y_o)^2}{r_c^2} \tag{7.63}$$

and (X_o, Y_o) is the initial position of the vortex.

Since details of the initial Reynolds stress profiles would not have much influence on the mean flow, as shown in the test problem in Chapter 6, the initial Reynolds stress components have been specified as:

$$\overline{u^2} = \overline{v^2} = \overline{w^2} = \frac{2}{3} k_o \, ,$$

$$\text{and} \qquad \overline{uv} = 0 \, .$$

Computations were started at the same location of the vortex pair as the laminar cases with the same grid discussed in Chapter 5. The maximum initial (dimensionless) turbulent kinetic energy employed here was k_o=0.32.

The turbulent vorticity transport equation (3.73), for unstratified flows, was handled numerically in the same manner as the laminar study, using an alternating direction implicit (ADI) scheme with upwind flux-splitting. The additional Reynolds stress terms were treated as central differences. The Reynolds stress transport equations (3.64 to 3.67), also without the stratification effect terms, were solved using the same ADI scheme employed for vorticity transport.

The modeled Reynolds stress transport equations do not satisfy automatically the realizability restrictions discussed by Schumann (1977) and Lumley (1983). That is, small negative values of $\overline{u^2}, \overline{v^2}$, and $\overline{w^2}$ could be produced during initial time steps, which were due simply to numerical round off errors. In order to prevent those non-realizable quantities from propagating, the simple "clipping" procedure suggested by Deardorff (1973) was employed, whereby negative values of any of the $\overline{u_I^2}$ (I=1,2, or 3), were replaced with zeros.

Turbulent simulations were run at Reynolds numbers (Γ_o/ν) of 1,000 and 75,000. As expected, for the Reynolds number of 1,000, the laminar and turbulent cases produced essentially identical results. At a Reynolds number of 75,000, there are differences between the laminar and turbulent predictions, as shown in Figures 7.5 through 7.7. While there is little difference initially (since the two flow cases start with the same mean velocity profiles), there are subtle changes in the trajectories at later times. It is noted that the higher Reynolds number turbulent vortices do not rebound vertically with the same magnitude as their laminar counterparts (at the same Reynolds number). However, the lateral motion behavior of the turbulent vortex is almost the same as for the laminar flow case. That means turbulent diffusion reduces the vortex rebound momentum significantly.

The circulation Γ(2x3) and kinetic energy E(2x3) histories are shown in Figure 7.6. It is noted that there is virtually no difference between the laminar and turbulent circulation histories, which reaffirms the inviscid nature of circulation behavior. There is a small, but noticable, relative decrease in turbulent kinetic energy with time. The additional decrease is due to the increased dissipation of positive and negative vorticity in the turbulent case.

Referring to Figure 7.7, it is seen that the turbulent, mean tangential velocity profiles are attenuated more strongly after the passage of time than are their laminar counterparts.

The decreased vertical rebound momentum of the turbulent case is also shown in Figure 7.7. The vertical velocity profile at t=36 in the laminar case (Figure 7.7(a)) shows that the vortex has a strong upward motion which causes the positive peak velocity value to achieve even higher level than the maximum peak velocity at t=24, although the vorticity level is lower at t=36 than t=24. It has been noted that at t=24, the vortex core is near its motion trough, leaving the vertical motion (see Figure 7.5(c)) with a very small upward velocity component, while at t=36, the vortex has begun to rebound. This higher vertical velocity does not occur in the corresponding turbulent case (Figure 7.7(b)), where the peak value at t=36 is slightly smaller than the value at t=24.

Figure 7.8 shows that at earlier time levels, the vortex cores dilate somewhat more rapidly for the turbulent case than for the laminar predictions. At later times, after the vortex is nearer to the ground plane, the turbulent vortex starts to dilate more slowly than the laminar case. This is caused by the negative viscosity effects produced by the Reynolds stress transport model. That shows that the Reynolds transport model can avoid the excessive viscous dissipation predicted by eddy-viscosity models, which is a very important consideration in realistic wake-vortex predictions.

The contours of turbulent kinetic energy, k, at dimensionless time t=16 and 26 are shown in Figure 7.9. These contours show that after the passage of time, lowered levels of kinetic energy are predicted in the central core region, when compared to the relatively higher turbulent kinetic energy levels found in the regions where vorticity changes sign. That means that the Reynolds stress transport model is able to predict relaminarization

in the vortex core. The ground plane boundary layer separation regions can also be discerned in the contours.

In summary, it has been shown in this chapter that the numerical scheme employed here produces good results in comparison with the experimental results of Liu and Srnsky (1990). The vortex rebound phenomenon near the ground is captured by the numerical simulation and the rebound mechanism of the simulation agrees with the experimental observation of Harvey and Perry (1971). Reynolds numbers affects both the trajectories and strengths of the wake vortices near the ground. The vortex rebound momentum of turbulent vortex wakes is reduced in comparison with their laminar counterparts. Reynolds stress-transport models should be used in vortex wake calculations to avoid underestimation of wake vortex hazard. However, vortex hazard is difficult to quantify and only a hypothetical method to address the hazard is shown here.

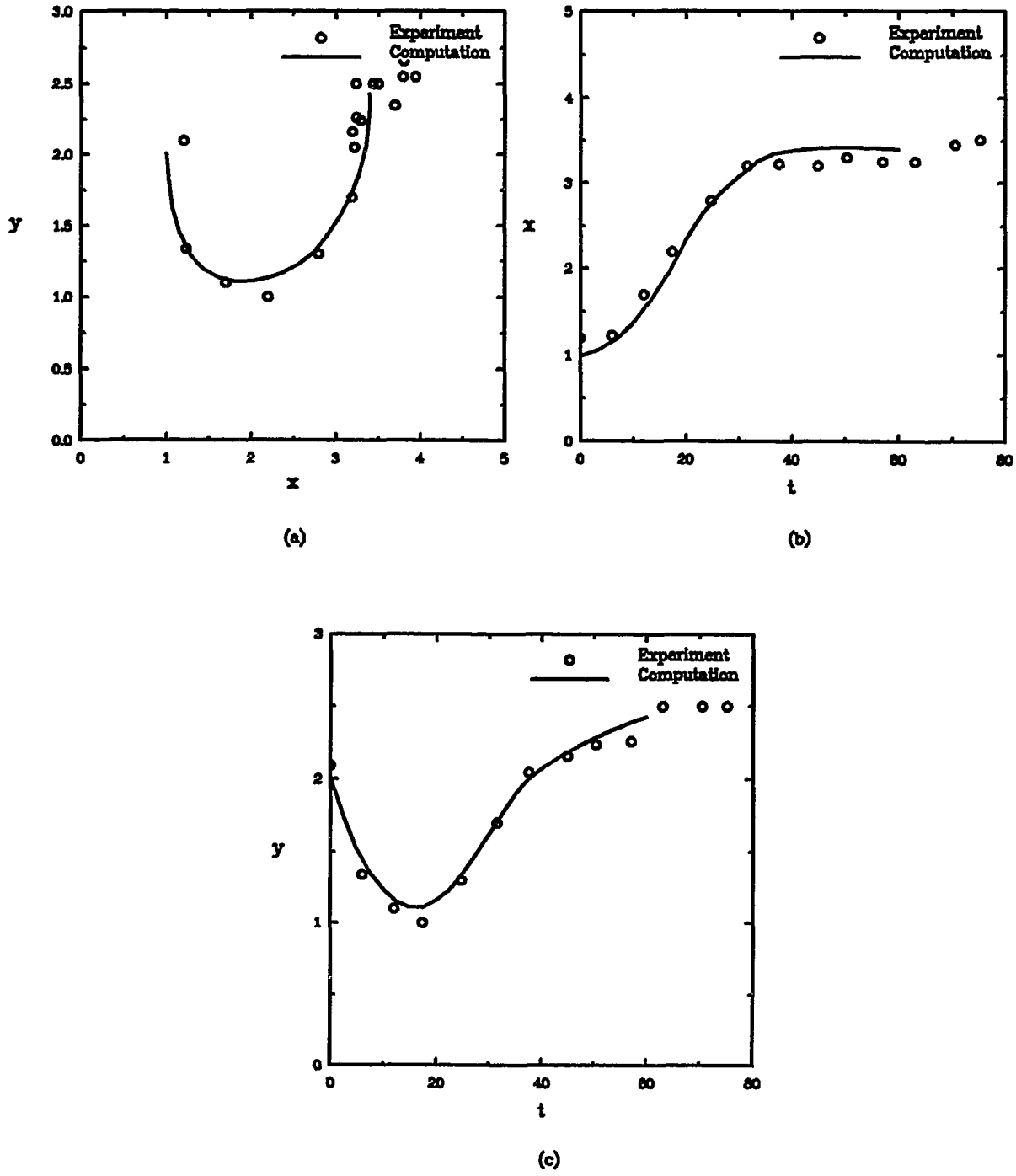

Figure 7.1 Comparison of computed vortex behavior with the experimental measurements of Liu and Srnsky (1990), (a) Vortex core trajectories, (b) Lateral vortex core position histories, (c) Vortex core elevation histories, at $Re = 7,650$

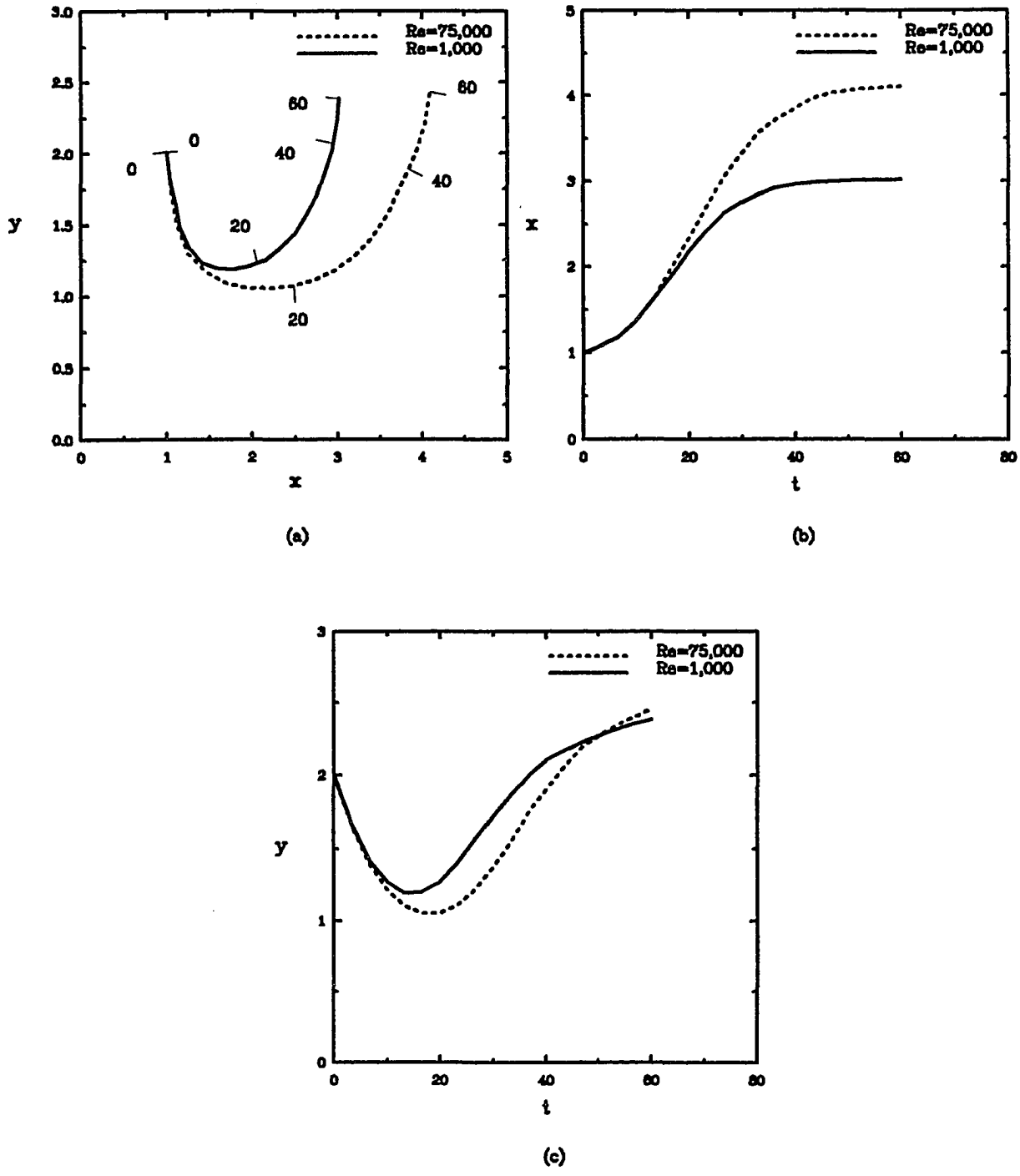

Figure 7.2 Influence of Reynolds number on vortex behavior: (a) Vortex core trajectories, (b) Lateral core vortex position histories, (c) Vortex core elevation histories

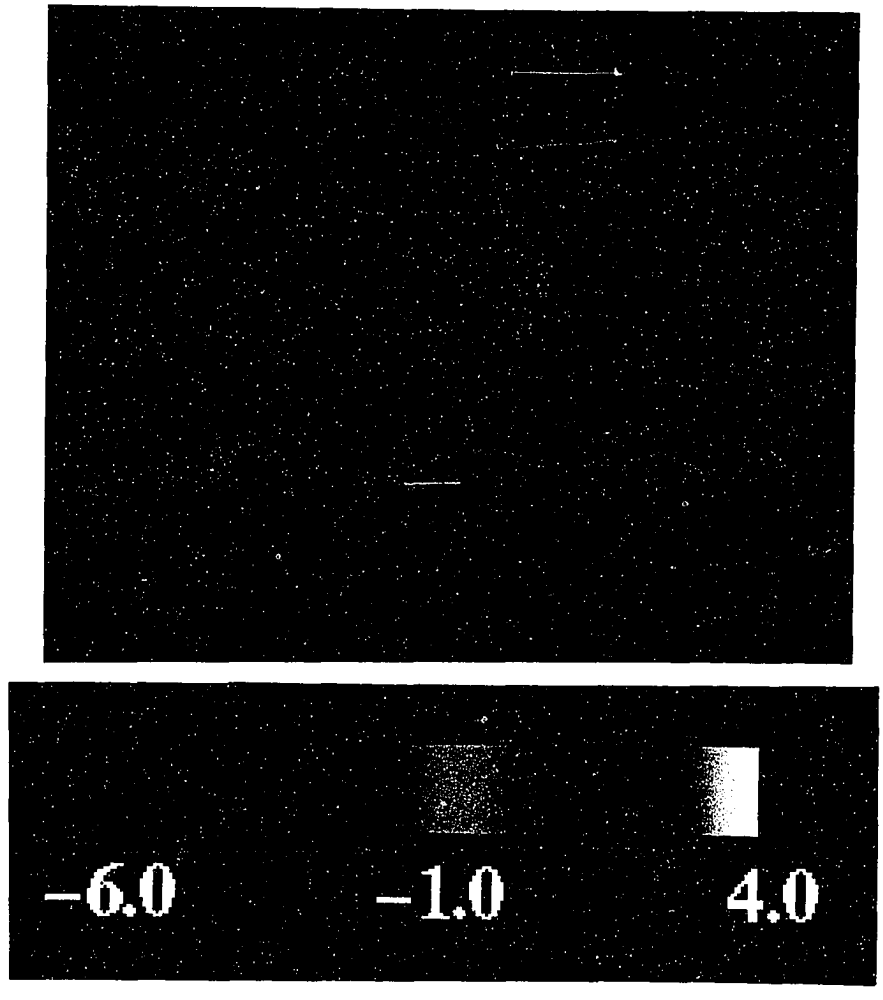

(a) Vorticity field at t=16

Figure 7.3 Color contours of vorticity field with *Re*=1,000, (a) t=16, (b) t=26

(Notice that in this figure and in all the symmetric cases in Chapters 7 and 8, the left half of color contours of vorticity field is the mirror-reflection of the right half. The sign of the left half part should be opposite to the right half part.)

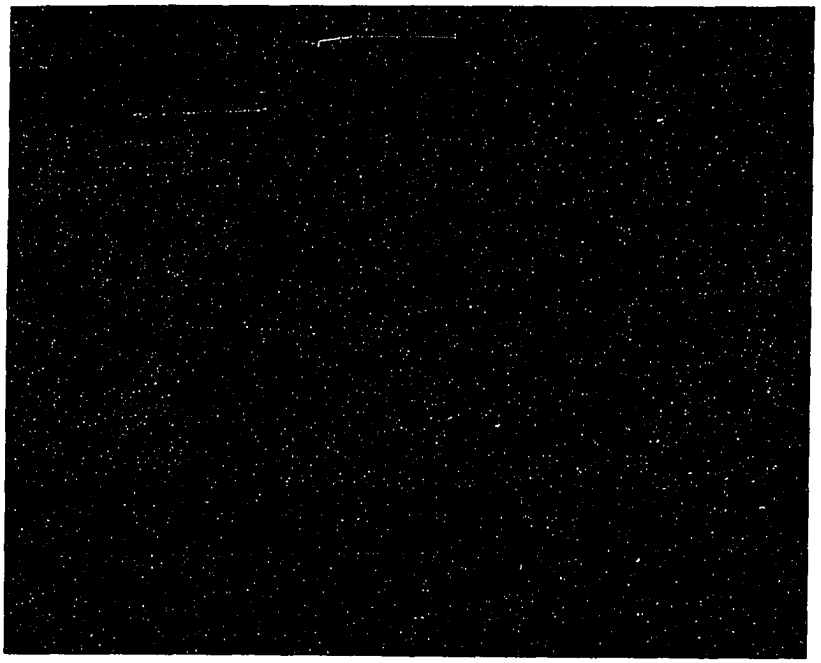

(b) Vorticity field at t =26

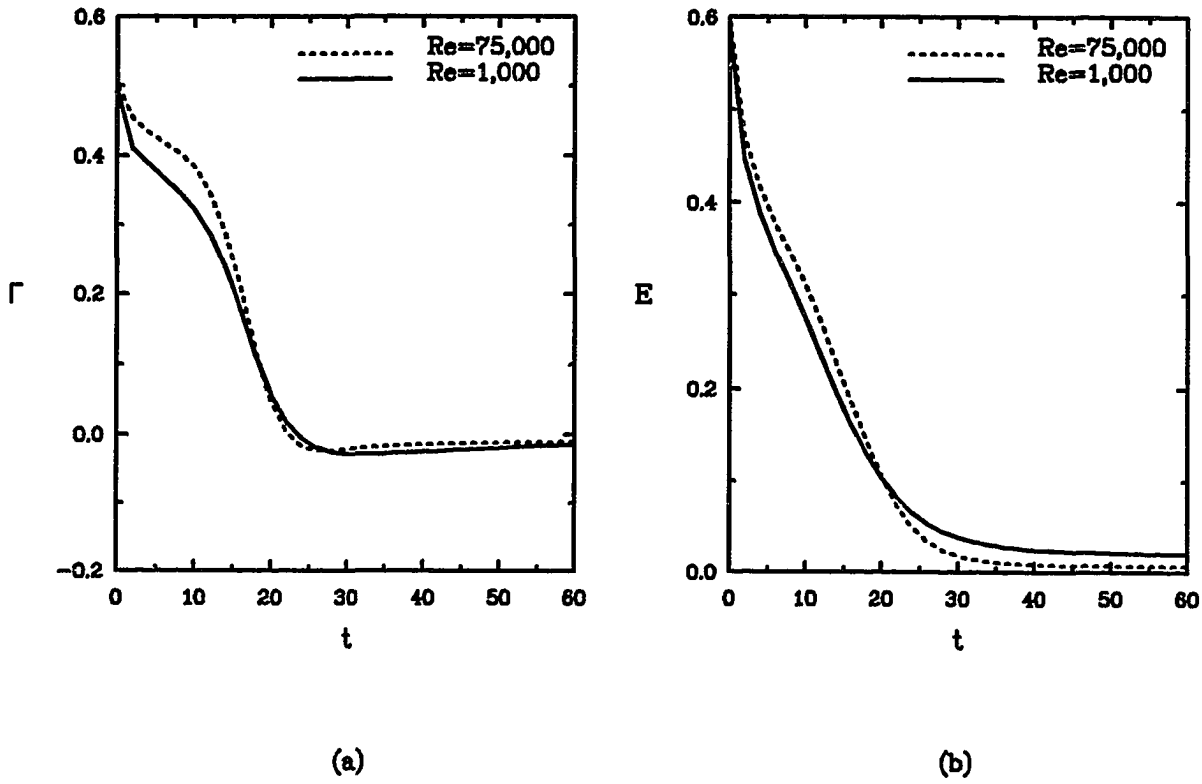

Figure 7.4 Predicted variation of (a) Circulation $\Gamma(2\times3)$,

(b) Kinetic energy $E(2\times3)$, with time for different *Re*

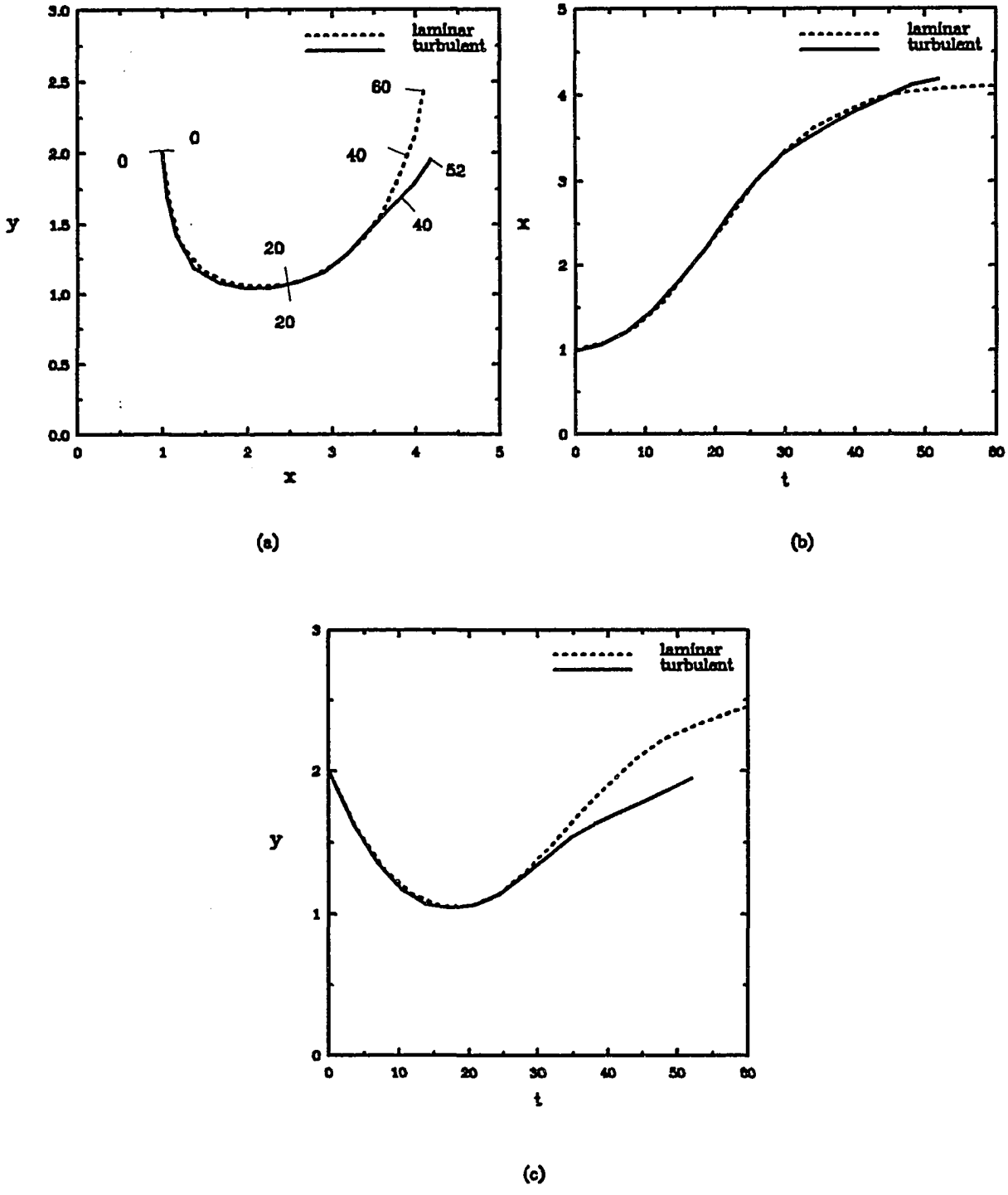

Figure 7.5 Comparison between laminar and turbulent vortex behavior near the ground (a) Vortex core trajectories, (b) Lateral vortex core position histories, (c) Vortex core elevation histories (*Re*=75,000)

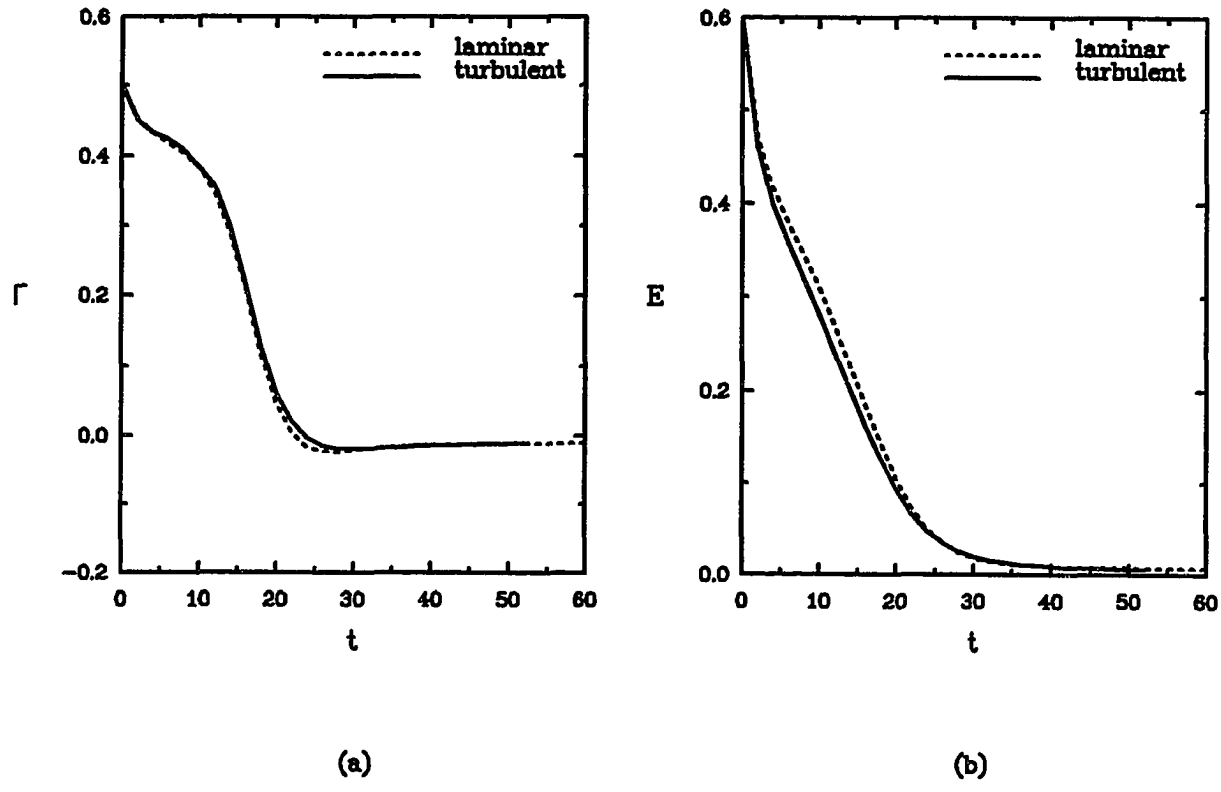

Figure 7.6 Comparison between laminar and turbulent predicted variation of (a) $\Gamma(2\times3)$, (b) $E(2\times3)$

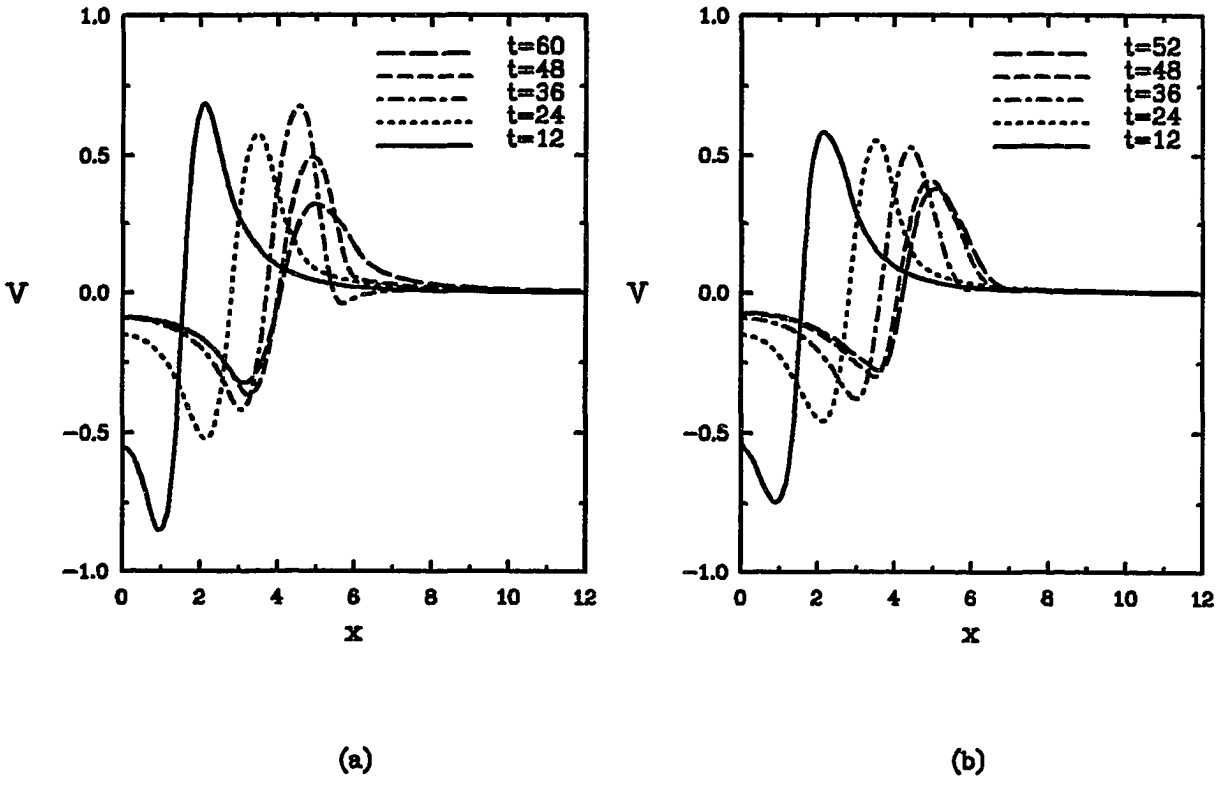

Figure 7.7 Vertical (or tangential) velocity profile histories in the plane of the primary vortex axis at different time steps for Re=75,000, (a) Laminar, (b) Turbulent (k_0=0.32)

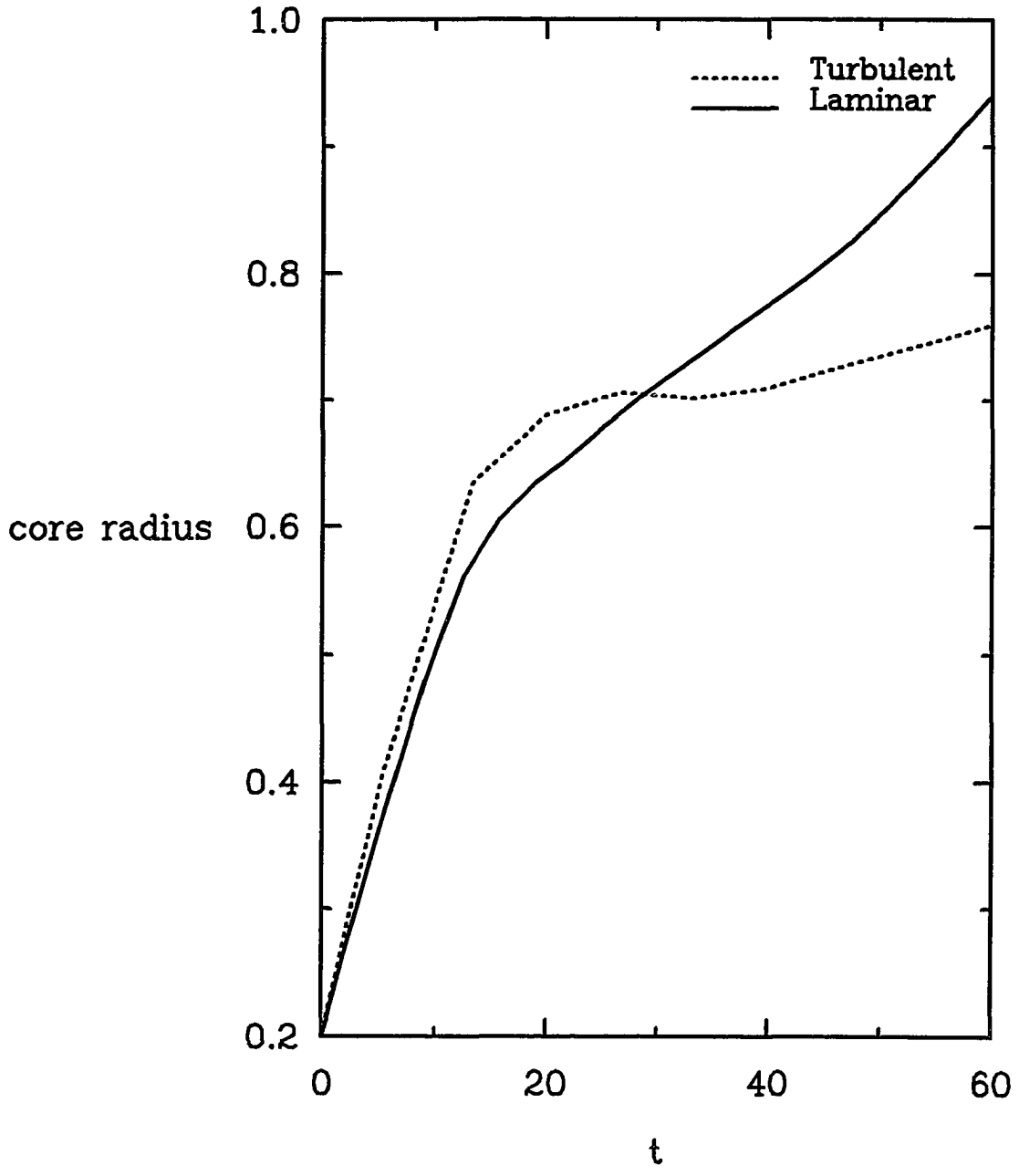

Figure 7.8 Comparison of vortex core radius histories for laminar and turbulent cases at *Re*=75,000

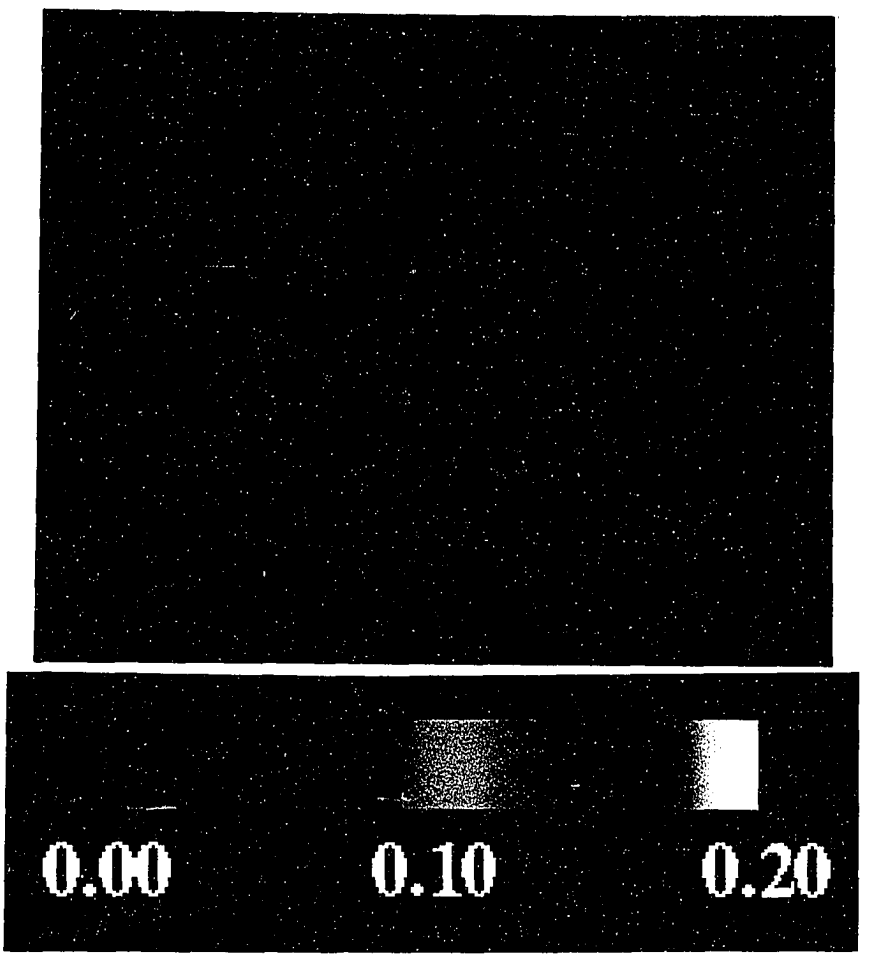

(a) The turbulent kinetic energy distribution at t=16

Figure 7.9 Color contour representation of the turbulent kinetic energy distribution at (a) t=16, (b) t=26

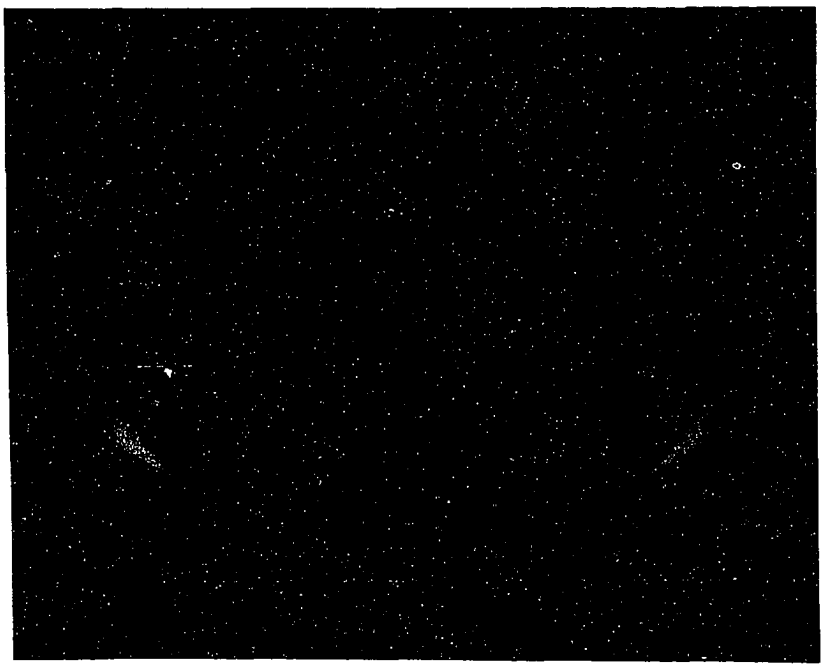

(b) The turbulent kinetic energy distribution at t =26

Chapter 8 Stratification Effects

The numerical simulation including stratification was performed using the dimensionless form of Eqns. (3.40), (3.41) and (3.43) for the laminar cases and Eqns. (3.53), (3.64)-(3.73) for the turbulent cases. The computational scheme was easily modified to include stratification since the same grid was used (where the vertical symmetry plane applies to both Chapter 7 and this chapter). The density departure equation (Eqn. 3.53), and density fluctuation equation (Eqn. 3.68), as well as density-velocity correlation equations (Eqns. 3.69 and 3.70), could be implemented using the same procedures employed for the vorticity transport equation and the Reynolds stress equations. The physical meaning and the influence of the Brunt-Väisälä frequency, which is the parameter used to quantify stratification effects, is discussed. Different levels of stratification have been simulated for both laminar and turbulent flow cases and significant effects have been found.

8.1 Brunt-Väisälä Frequency

A parameter indicative of the degree of stratification in a fluid is the buoyancy driven oscillation frequency or the Brunt-Väisälä frequency. The Brunt-Väisälä frequency is the oscillation frequency that would occur for an hypothetical inviscid fluid element which has been displaced from its equilibrium position (Turner, 1973), i.e., the natural vertical frequency of a buoyancy driven oscillation. Thus, the Brunt-Väisälä frequency, N^*, is

quantified through the vertical density gradient and the gravitational field acting on the atmosphere, and is in this study defined as

$$N^{*2} = g\frac{\beta}{T_o} . \tag{8.1}$$

It is noted that the dimensionless parameters, F_v and n, defined in Eqns. (3.78) and (3.80), respectively, are related to the Brunt-Väisälä frequency. In fact, N^* can be expressed as

$$N^{*2} = \frac{\Gamma_0^2 n^2}{s_0^4 F_v^2} , \tag{8.2}$$

if the characteristic scales introduced in Section 3.4 are used.

Stratification effects represent additional simulation difficulties because of the characteristic time introduced via Brunt-Väisälä frequency or density induced oscillations. If the dimensionless Brunt-Väisälä frequency $N \equiv s_0^2 N^*/\Gamma_0 (= \frac{n}{Fv})$ is much greater than unity, buoyancy effects are significant and the characteristic vortex motion time (s_0^2/Γ_0) is large compared with the time interval over which density induced oscillations occur. That means that if the buoyancy effects are strong, a smaller time scale, determined by the buoyancy driven oscillation, must be used as a characteristic time scale to resolve buoyancy waves. On the other hand, if $N \ll 1$, the vortex motions occur with little influence due to stratification. The complication arising from these two competing characteristic times has been examined in detail by Hirsh (1985). For more realistic physical problems, F_v is typically on the order of unity and the stratified density gradient (through n) is not large enough to result in large values of N, precluding $N \gg 1$ cases. Consequently, a limiting test case is when the two time scales are comparable ($N \approx 1$).

Simulations were run with $N = 1$, but the density effects were so large that major vortices of opposite sign were generated very rapidly and the flow quickly became unstable numerically. As a result, smaller stratification strengths were considered in this study. Based upon the study of Schilling (1992), stratification levels represented by $N > 0.59$ are not likely under realistic conditions.

8.2 Results and Discussion

8.2.1 Laminar Cases

Experimental data were not available for comparison with the simulated vortex flows in a stably stratified ambient environment with ground effect. Stratification effects were thus tested for a circulation-based Reynolds number of 1000, at dimensionless Brunt-Väisälä frequencies (n/F_v) of N = 0.05 and N = 0.3. The predicted results for this laminar flow case are displayed in Figures 8.1 and 8.2, along with the unstratified reference case (N = 0). The vortex trajectories, including lateral and vertical position histories, along with circulation strength $\Gamma(2\times3)$ and kinetic energy $E(2\times3)$ histories are displayed.

While the laminar flow simulations (Re = 1000) are less realistic, in terms of aircraft vortices, they are less ambiguous in terms of influences of turbulence models and numerical uncertainties. Furthermore, because of the thicker viscous regions at lower Reynolds numbers, the physics can be displayed more clearly for low Reynolds number simulation cases. Consequently, vortex rebound and stratification effects, derived from fundamental phenomena, can be discussed with more certainty for the low Reynolds number flow cases. To that end, stratification effects in the vicinity of the ground plane have altered vortex trajectories rather remarkably, as shown in Figure 8.1.

Referring to Figure 8.1, it can be seen that the vortex appears literally to try to "fall back down hill" in both stratified cases, even though the initial descent and rebound trajectories coincide nominally with the unstratified case. The mechanism which is responsible for that effect can best be explained by comparing the computational flow visualization results from the unstratified case (N = 0) with the stratified case (N = 0.3).

Comparison between the vorticity distributions at selected time levels for an unstratified flow (Figure 7.3) with a corresponding stratified flow (Figure 8.3) shows some significant effects. Other than the secondary vortex induced near the ground which is outboard from the main vortex, the stratified case exhibits another secondary vortex of opposite sign evolving inboard with respect to the main vortex. The latter vortex induces downward motion on the main vortex, producing the "down hill" or unwinding effect.

While the additional opposite sign vorticity reduces the circulation (see Figure 8.2), even to negative values for the later time levels, stratification does not change the maximum vorticity in the vortex core region significantly. That means the total vorticity strength is not changed by stratification effects, only the circulation zones have been redistributed.

The influence of stratification on vortex trajectories is most easily understood by looking at the density distribution histories. Figure 8.4 shows density departure contours (from Eqn. 3.40, via ρ_∞, given in Eqn. 3.6) at three different times. There, it can be seen that relatively higher density fluid is pulled from the ground plane around the primary vortex, where it tends simultaneously to compress the vortex and cause more rapid vortex deceleration due to increased inertia. While the vortex doesn't actually roll back toward the ground by reversing itself like a wheel, the density distributions show that the body

forces actually push the primary vortex back toward the ground plane and the lateral density variations even push the vortex toward the symmetry plane. The inhibition of rebound and lateral propagation of the vortex pair with inclusion of stratification effects was also shown in Delisi *et al.* (1987), where they found the more extreme results that no rebound occurred.

The creation of an inboard secondary vortex can be explained by the density departure increment in the lateral direction near the same region. As shown in the modified vorticity transport equation (Eqn. 8.1), the positive sign x-direction derivatives of density departure create negative rates of change of vorticity. Near the vortex core, these derivatives are almost zero and thus the core vorticity does not change under the influence of stratification. Clearly, strong density stratification can confine and then destroy the structural features of trailing line vortices rapidly.

8.2.2 Turbulent Cases

We have studied the influence of stratification on a vortex pair when the vortex Reynolds number was 75,000, with a peak turbulent kinetic energy level, k_o, of 0.32, which are the same Reynolds number and turbulence level as the turbulence case in the previous chapter. The comparison between the stratified laminar case and stratified turbulent case is shown in Figures 8.5 and 8.6 and the comparison between the non-stratified turbulent case and stratified turbulent case is shown in Figures 8.7 and 8.8.

The (symmetric) trajectory of the vortex for a Brunt-Väisälä frequency, N, of 0.3 is shown in Figure 8.5, along with a laminar prediction for the same case. It is noted that, although both lateral and vertical motion of the turbulent vortex system is also

confined by stratification effects (see Figure 8.7) just as it was in the laminar cases (see Figure 8.1), the turbulent lateral motion occurs at a somewhat faster velocity than the laminar case, while the vertical vortex rebound is inhibited by turbulence. That behavior is consistent with physical processes in which turbulent fluctuations reduce the kinematic communication between the vortex system and its surroundings.

Figure 8.6 shows a comparison between the laminar and turbulent vertical velocity component profile histories, taken along the axis of the primary vortex, for the same stratified flow case represented in Figure 8.5. At the earlier time levels (t=12 and t=24), the velocity profiles are almost the same as those shown in Figure 7.7 and therefore are not replotted in Figure 8.6. The somewhat stronger influence of secondary vortex flow structures at the later time levels, near the vertical symmetry plane and outside of the primary vortex region (x>5), are apparent in the turbulent velocity profiles. Comparing corresponding velocity profiles with those of the unstratified cases in Figure 7.7, it can be seen that the stronger opposite sign vorticity occurs due to stratification in both laminar and turbulent flows.

The influence of stratification alone is shown in Figure 8.7, which compares the vortex trajectories for a turbulent system (Re=75,000) without stratification (N=0) to the stratified case (N=0.3). The significant influence of stratification is apparent, with the same trend as in the laminar cases (see Figure 8.1).

Finally, the measures of the circulation and kinetic energy histories ($\Gamma(2\times3)$ and $E(2\times3)$, respectively) have been compared in the primary computational domain for the stratified and unstratified turbulent vortex cases (Figure 8.8). As has been shown in Figure 8.2 for a laminar vortex system, the circulation level changes significantly for a

stratified system, when compared with the unstratified case. However, the kinetic energy histories remain almost the same. Although not shown here, the overall vorticity content varies only slightly between the two cases.

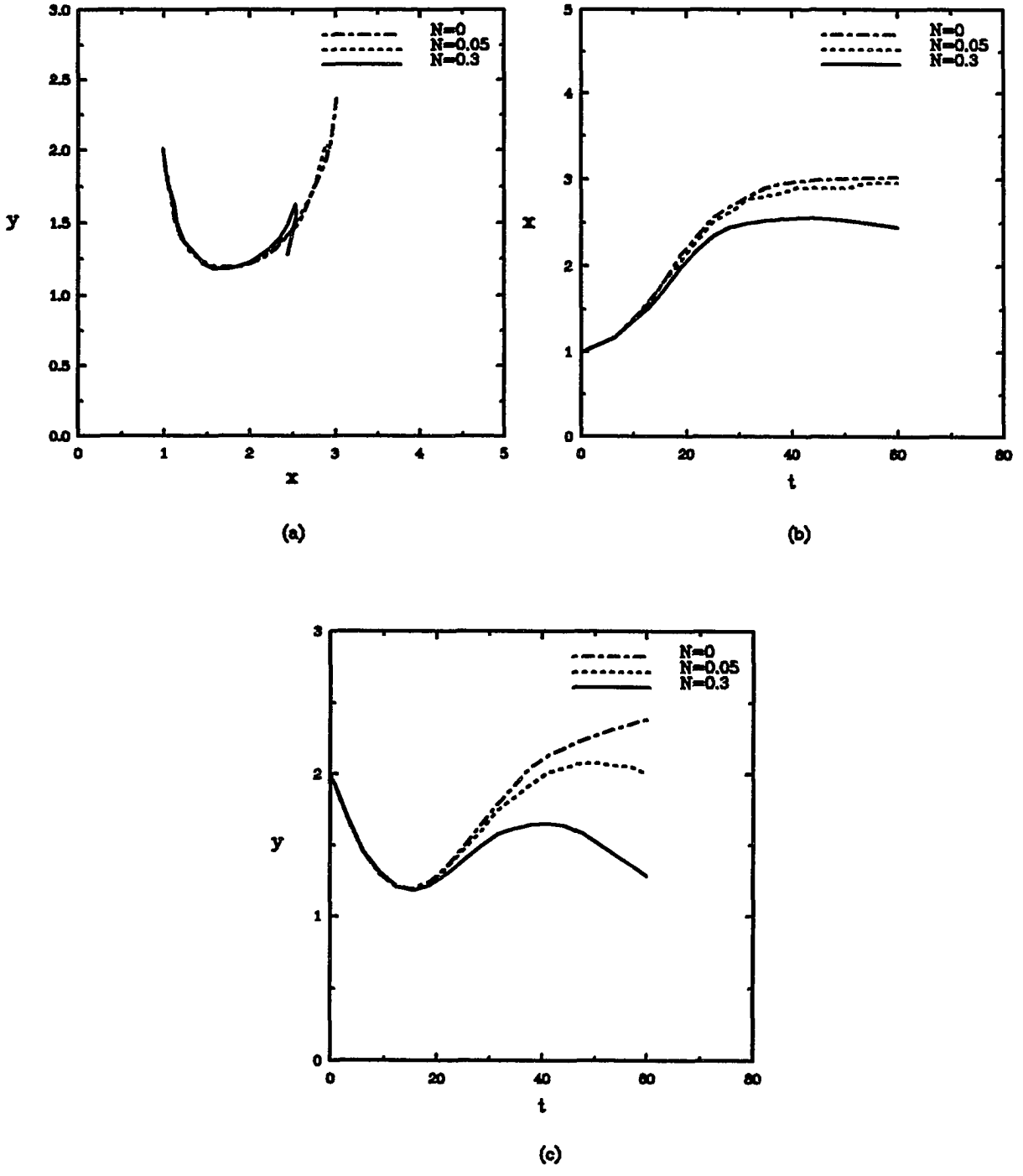

Figure 8.1 Influence of stratification on predicted (a) Vortex core trajectories, (b) Lateral vortex core position histories, and (c) Vortex core elevation histories, at *Re*=1,000

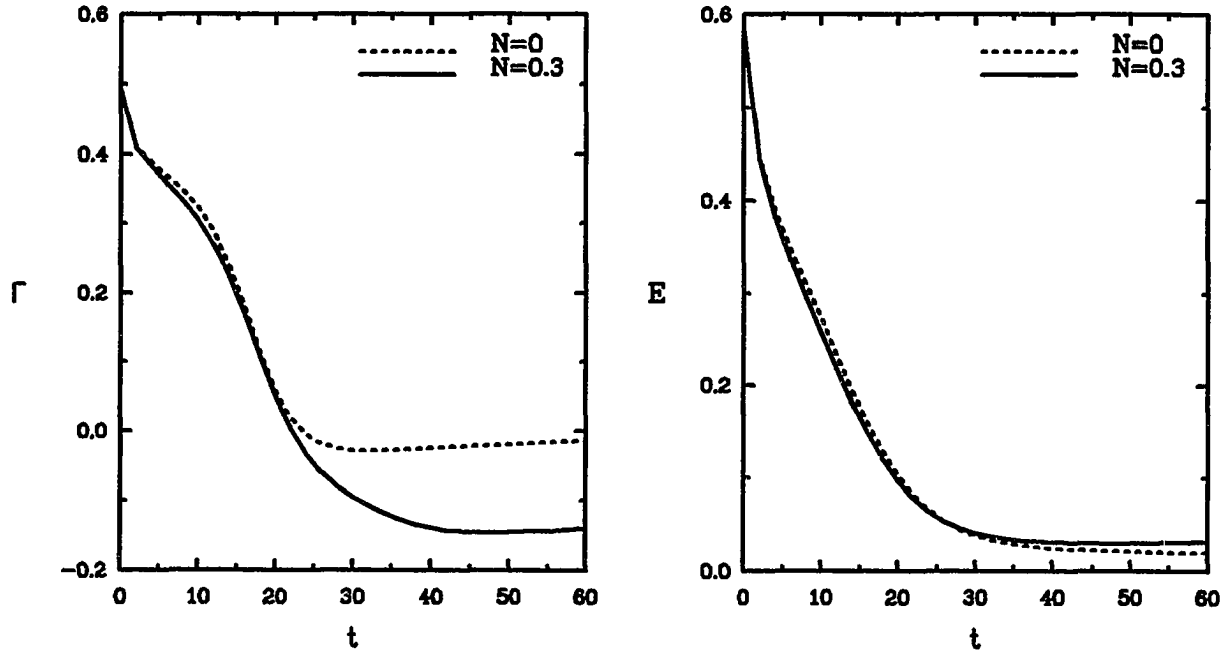

Figure 8.2 Influence of stratification on predicted variation of (a) Circulation $\Gamma(2\times3)$, (b) Kinetic energy $E(2\times3)$, with time for Re=1,000

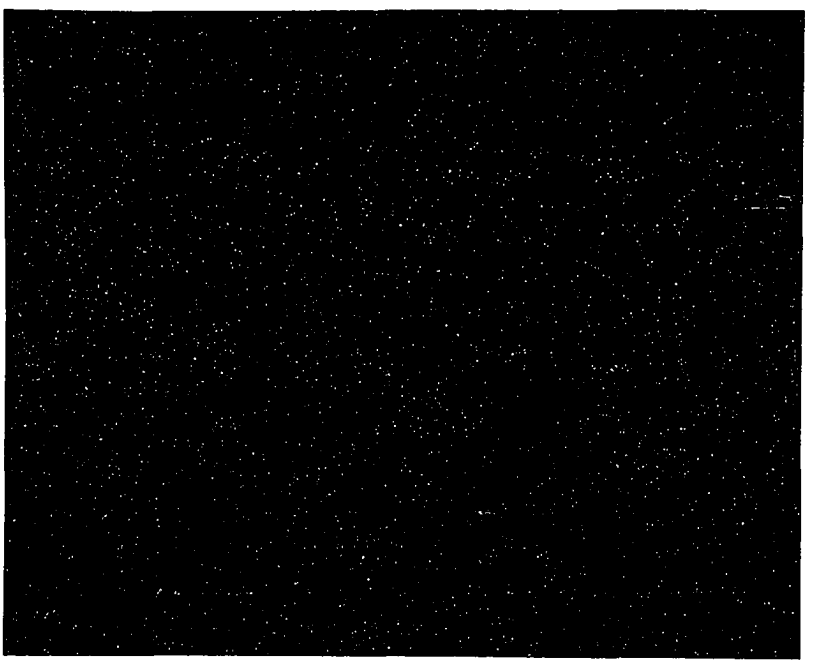

(a) Vorticity contours at t=16

Figure 8.3 Vorticity contours at (a) t=16, (b) t=50, with N=0.3, *Re*=1,000 (color map is the same as for Figure 7.3)

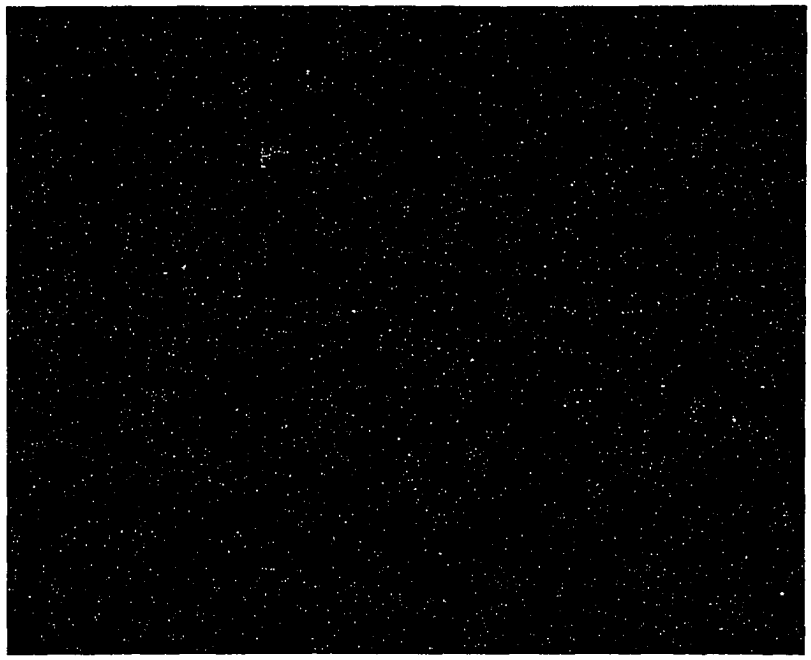

(b) Vorticity contours at t=50

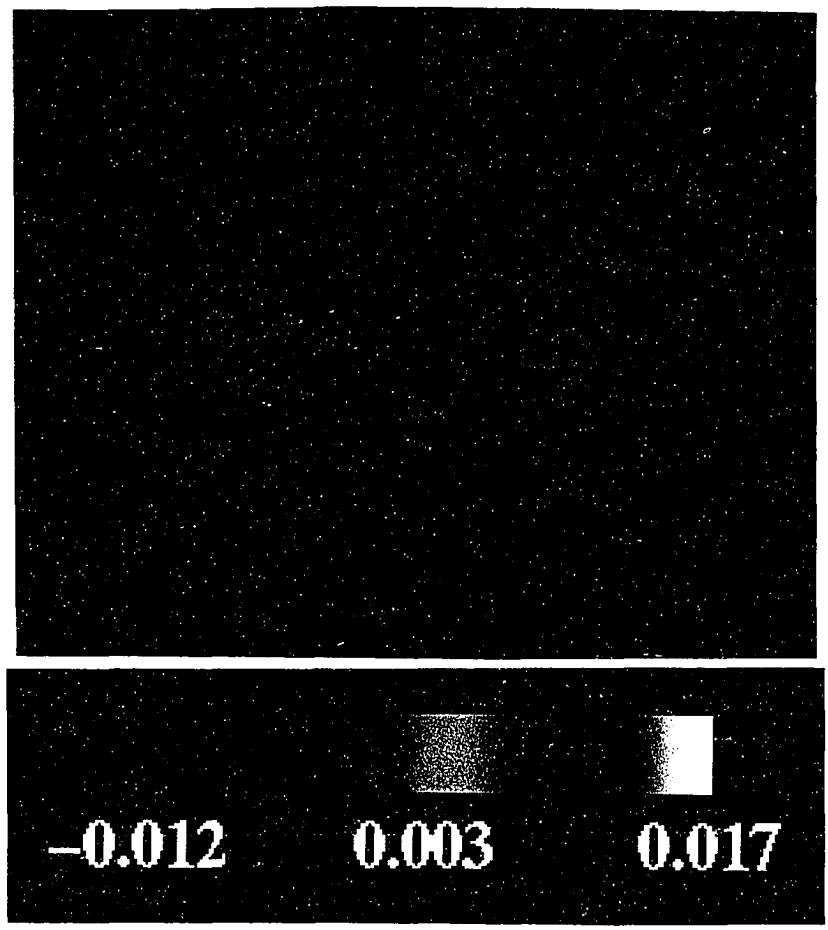

(a) Density departure contours as t=16

Figure 8.4 Density departure contours at (a) t=16, (b) t=26, (c) t=50, with N=0.3, Re=1,000

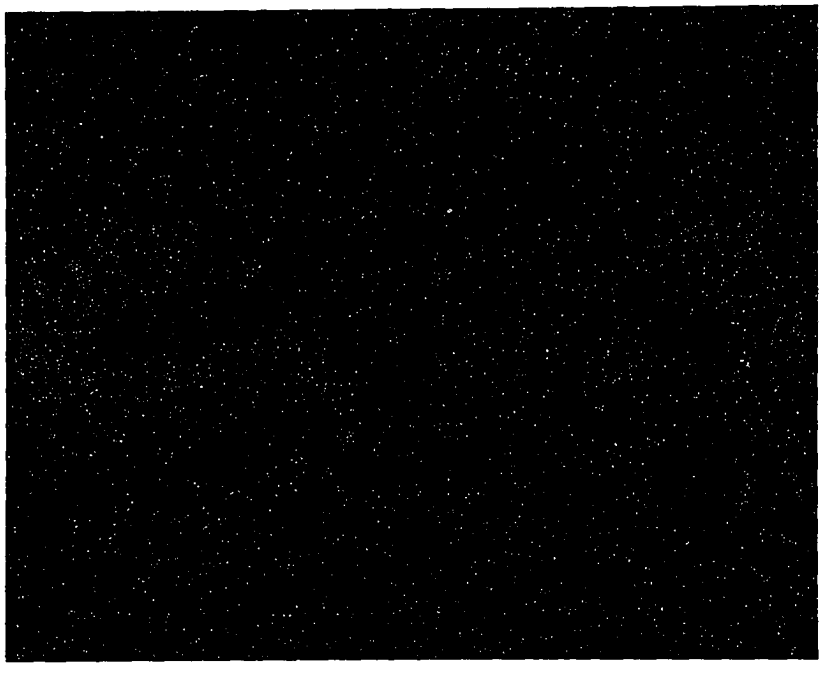

(b) Density departure contours at t=26

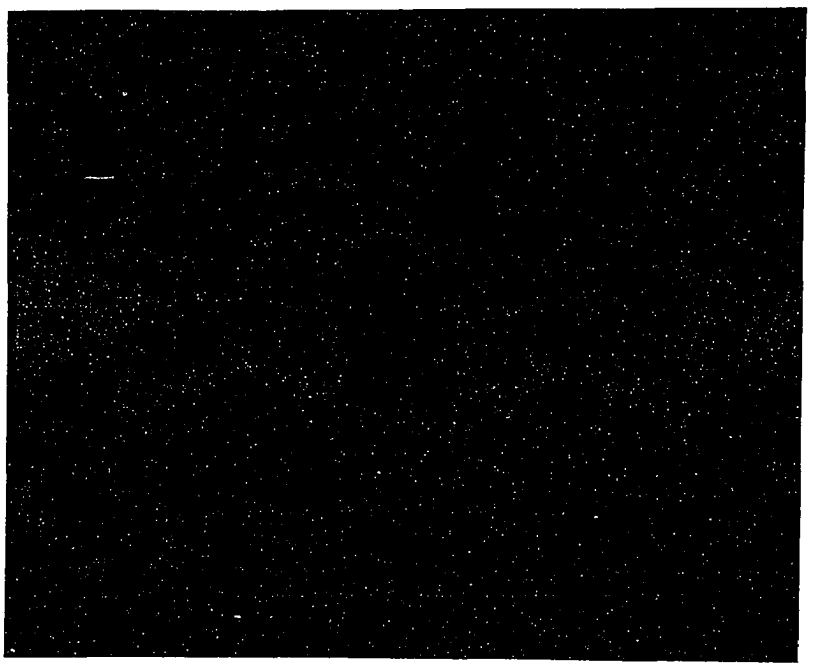

(c) Density departure contours at t=50

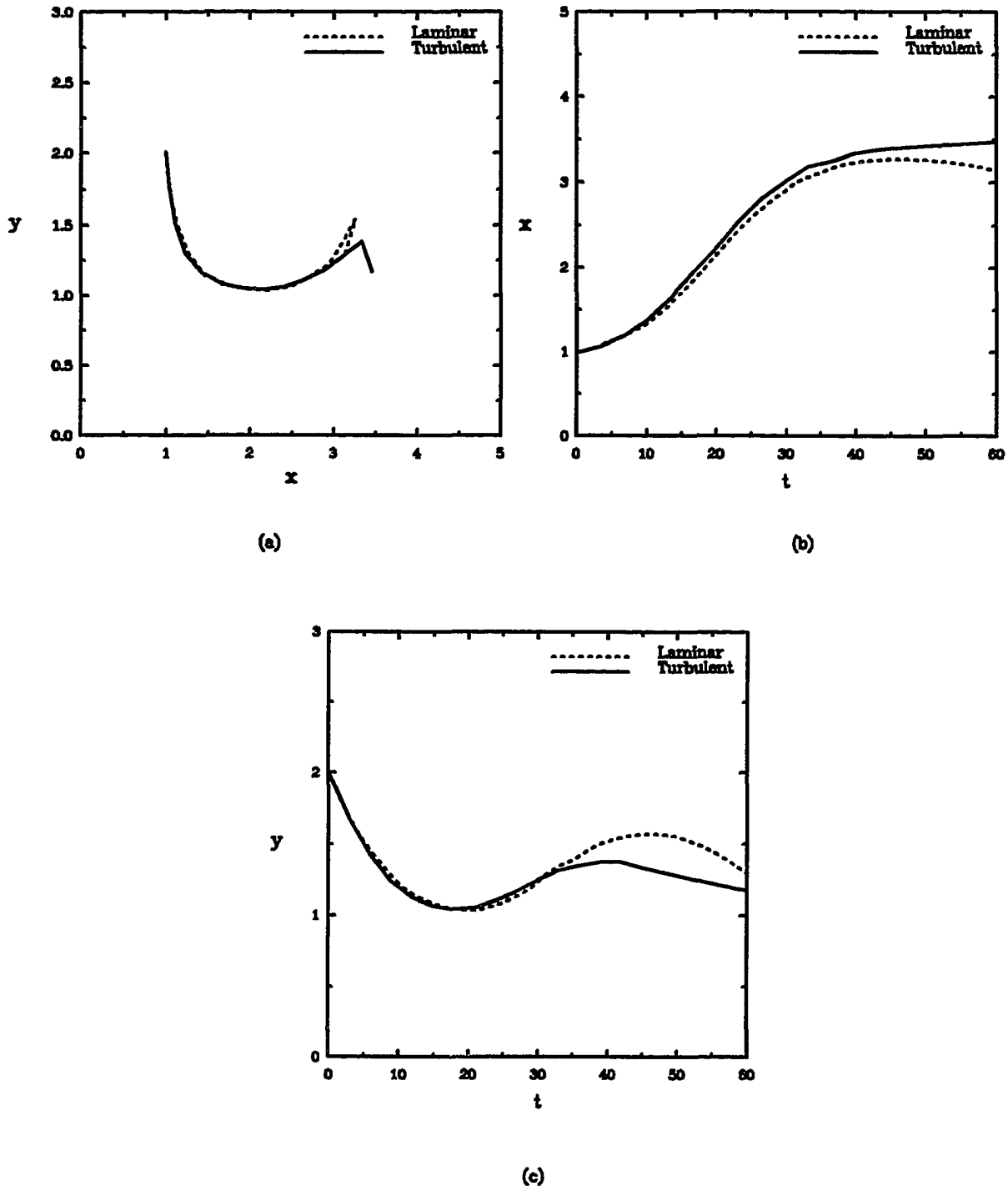

Figure 8.5 Comparison between laminar and turbulent vortex behavior near the ground (a) Vortex core trajectories, (b) Lateral vortex core position histories, and (c) Vortex core elevation histories, at N=0.3, *Re*=75,000

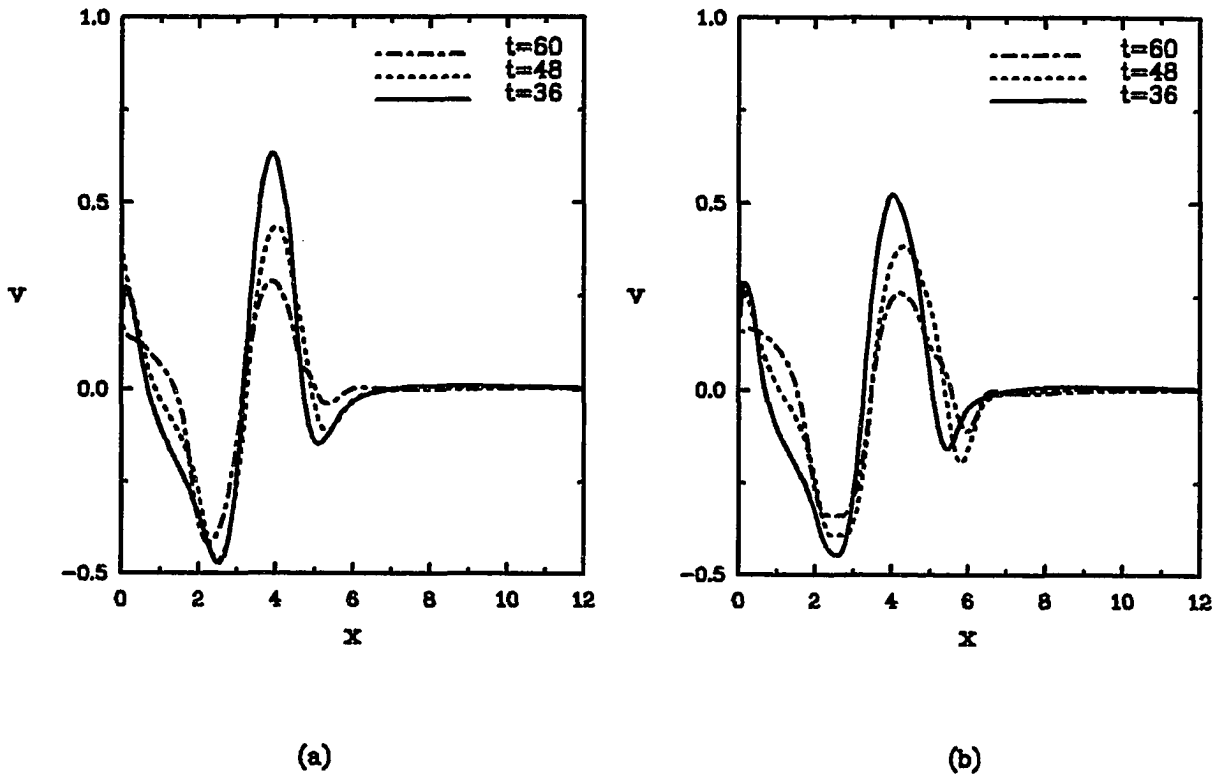

Figure 8.6 Vertical (or tangential) velocity profile histories in the plane of the primary vortex axis at different time steps for a stratified ambient environment (Re=75,000, N=0.3), (a) Laminar, (b) Turbulent (k_o=0.32)

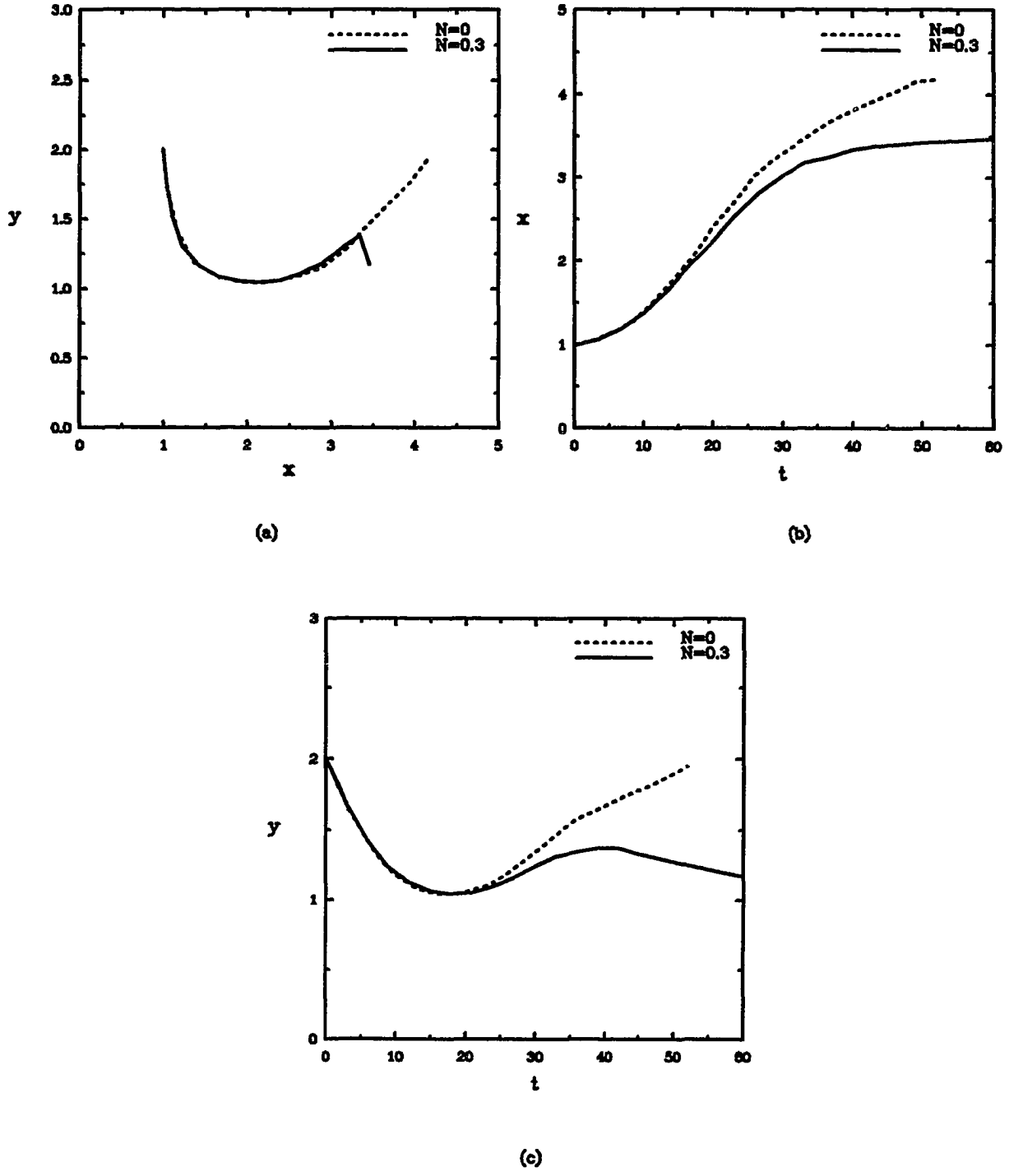

Figure 8.7 Influence of stratification on turbulent vortex behavior (a) Vortex trajectories, (b) Lateral vortex position histories, and (c) Vortex elevation histories

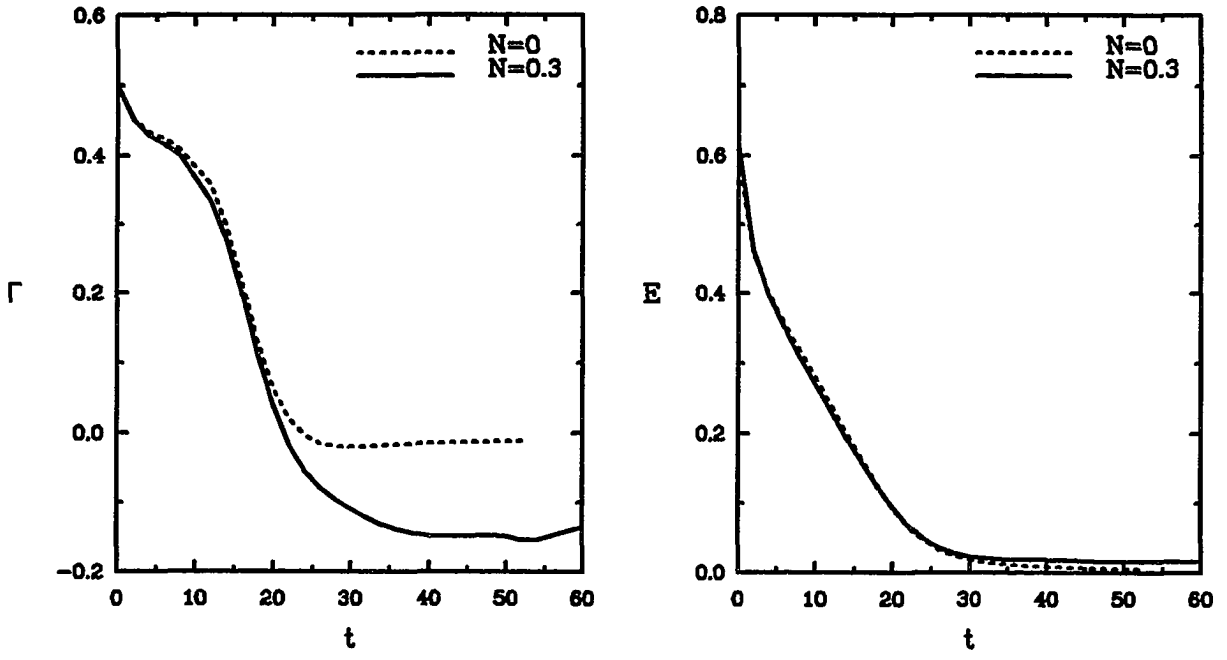

Figure 8.8 Influence of stratification on turbulent vortex strength

(a) Localized circulation $\Gamma(2\times3)$ and (b) Kinetic energy $E(2\times3)$

Chapter 9 Crosswind Effects

A preliminary study has been conducted to predict crosswind effects on vortex wake behavior near the ground. At this stage of the study, only laminar cases have been investigated. Since the number of grid points must be doubled to compensate for the loss of symmetry under crosswind conditions, turbulent cases need significantly larger amounts of storage (40M run-time memory vs. 15M for the laminar cases) and computational time (24 CPU hours on a Cray Y-MP for 6000 time steps vs. 12 hours for the laminar cases), which is beyond current resources available for this preliminary study. Rather, the asymmetric behavior of a viscous vortex wake and the computational modifications required by the cross-flow effects have been addressed in this chapter. It is important to recognize that stratification effects can be included along with crosswind effects with only moderate additional computational effort, but the resources required for these turbulent cases are formidable.

The whole upper half plane must be considered for crosswind simulations instead of using just the first quadrant because of the asymmetry brought in by cross flows. Furthermore, a moving grid must be employed to capture the vortex pair propagating with cross flow convection. In the following, a uniformly moving grid, with constant translational speed, U_∞, which is the assumed uniform velocity of the cross wind outside of the crosswind boundary layer, is used to capture the crosswind flow field. The uniformly moving grid gives proper resolution within the period of vortex sustenance

for typical atmospheric crosswind profiles. However, in Section 9.1 it can be proved that the vorticity-streamfunction formulation, under any type of time dependent translational coordinate motion, with velocity components $U_\infty(t)$ and $V_\infty(t)$, is not affected by the motion. Rather, the crosswind effects are included in the boundary conditions, as explained in Section 9.2.

A reflection mapping of the 150×300 grid from the right-half of the computational domain, which was employed in Chapters 7 and 8, has been used to extend the computational domain into the whole upper-half space, resulting in a 300×300 grid. The same computational scheme has been used as the one in the symmetric cases, removing the symmetry boundary conditions on the center line of the grid. All of the cases included in the present study have been tested at a circulation Reynolds number of Re=1,000.

9.1 Formulation in Moving Coordinates

Appending the variables in the space-fixed coordinate system with a subscript, f, the following expressions relate the moving coordinate derivatives to their fixed coordinate counterparts:

$$\frac{\partial}{\partial x_f} = \frac{\partial}{\partial x}, \tag{9.1}$$

$$\frac{\partial}{\partial y_f} = \frac{\partial}{\partial y}, \tag{9.2}$$

$$\frac{\partial}{\partial t_f} = \frac{\partial}{\partial t} - U_\infty(t)\frac{\partial}{\partial x} - V_\infty(t)\frac{\partial}{\partial y}. \tag{9.3}$$

Hence, Eqn. (4.1) becomes

$$\frac{\partial \zeta}{\partial t} + (u_f - U_\infty)\frac{\partial \zeta}{\partial x} + (v_f - V_\infty)\frac{\partial \zeta}{\partial y} = \frac{1}{Re}\nabla^2\zeta. \tag{9.4}$$

By defining the velocities in the moving coordinate system as

$$u = u_f - U_\infty \,, \tag{9.5}$$

and

$$v = v_f - V_\infty \,, \tag{9.6}$$

where u_f and v_f are the velocity components in the space-fixed coordinates, the same form of equation as Eqn. (3.76) is obtained. The streamfunction equation, Eqn. (3.43), is also retained with

$$\frac{\partial \psi}{\partial y} = u_f - U_\infty \equiv u \,, \tag{9.7}$$

and

$$\frac{\partial \psi}{\partial x} = -(v_f - V_\infty) \equiv -v \,. \tag{9.8}$$

It is noted that this transformation is not transparent for primitive variable formulations. The additional terms produced by the translational acceleration will appear in the momentum equations. A conservative form of the Navier-Stokes equations in primitive variables in a moving frame of reference can be found in Kandil and Chuang (1990). When the cross-products are taken to develop the vorticity transport equation, the translational acceleration terms, which are irrotational, become zero. The detailed derivation for arbitrary coordinate translations is presented in Appendix A.

9.2 Cross Flow Profiles and the Boundary Conditions

Crosswind profiles were approximated as boundary-layer velocity distributions over flat planes. In laminar cases, the von Karman integral representation was used (Schlichting 1979):

$$\frac{u_c}{U_\infty} = 2\frac{y}{\delta} - 2\left(\frac{y}{\delta}\right)^3 + \left(\frac{y}{\delta}\right)^4 \tag{9.9}$$

where u_c is the crosswind speed, δ is the thickness of the crosswind boundary-layer and U_∞ is the uniform velocity outside the boundary layer.

The previous section has shown that crosswind effects do not appear directly in the equations, but the boundary conditions must be altered to introduce the effects. In a coordinate system which is moving with velocity U_∞, the boundary conditions can be derived as:

At $x = \pm\infty$:

$$u = u_f - U_\infty = u_c - U_\infty \,,\; v = 0 \tag{9.10}$$

and then

$$\zeta = \begin{cases} -\frac{U_\infty}{\delta}\left[2 - 6\left(\frac{y}{\delta}\right) + 4\left(\frac{y}{\delta}\right)^3\right] & (y < \delta) \\ 0 & (y \geq \delta) \end{cases}, \tag{9.11}$$

$$\psi = \begin{cases} U_\infty y\left[\frac{y}{\delta} - \frac{1}{2}\left(\frac{y}{\delta}\right)^3 + \frac{1}{5}\left(\frac{y}{\delta}\right)^4 - 1\right] & (y < \delta) \\ -\frac{3}{10}U_\infty\delta & (y \geq \delta) \end{cases}. \tag{9.12}$$

At $y = \infty$:

$$u = u_f - U_\infty = 0 \,,\; v = 0 \,, \tag{9.13}$$

and

$$\zeta = 0\,,\ \psi = -\frac{3}{10}U_\infty \delta\,. \tag{9.14}$$

At $y = 0$:

$$u = -U_\infty\,,\ v = 0\,, \tag{9.15}$$

and

$$\zeta = -\frac{\partial^2 \psi}{\partial y^2}\bigg|_{y=0}\,,\quad \psi = 0\,. \tag{9.16}$$

Using a Taylor series expansion,

$$\psi|_{y=\Delta y} = \psi|_{y=0} + \frac{\partial \psi}{\partial y}\bigg|_{y=0} \Delta y + \frac{\partial^2 \psi}{\partial y^2}\bigg|_{y=0} (\Delta y)^2 + \cdots\,, \tag{9.17}$$

and since

$$\frac{\partial \psi}{\partial y}\bigg|_{y=0} = u = -U_\infty\,, \tag{9.18}$$

the vorticity boundary condition on the ground plane can be written as:

$$\zeta = -\frac{2}{(\Delta y)^2}\left(\psi|_{y=\Delta y} + U_\infty \Delta y\right)\,. \tag{9.19}$$

Thus, the crosswind effects are included in the boundary conditions, Eqns. (9.11), (9.12), (9.14) and (9.19).

9.3 Results and Discussion

Trajectories of both the left and right hand vortices are shown in Figure 9.1, for Re=1,000, δ=10, U_∞=0.1 (blowing from left to right in x-direction). That figure shows that the left (upstream) vortex motion is confined by crosswind effects. Its lateral shift, due to ground effect, is compensated by advecting with the cross wind so that the left vortex appears to have little lateral motion (and thus would stay above the same runway). The advecting effects translate the lateral motion of the right (downstream) vortex to a (hypothetical) parallel runway. In addition, the crosswind causes the right vortex to rebound higher than the left vortex. In Figure 9.2(b), it is noted that before vortex rebound happens, the two vortices have the same vertical descent history. When vortex rebound starts, the right vortex elevation history begins to deviate from that of the left vortex. Since in Chapter 7, it was shown that vortex rebound was caused by ground boundary layer separation, from Figure 9.2(b), it can be speculated that the crosswind influences ground boundary separation and thus alters the vortex rebound behavior of the two vortices.

The counterclockwise-vortex-system tilting behavior displayed, in Figure 9.1, can be explained using vorticity contours (Figure 9.3). In Figure 9.3(a), the induced boundary layer under the left (upstream) vortex is thinned by the cross wind because this part of the boundary layer has opposite sign vorticity from the crosswind boundary layer. Simultaneously, the boundary layer under the right vortex is thickened because it has the same sign vorticity as the cross wind. Hence, at later time levels, shown in Figure 9.3(b), the secondary vortex induced by the right vortex is stronger than that by the left vortex and thus the right vortex rebounds more than the left one.

It is noted that this type of vortex tilting (the downstream vortex rebounding higher than the upstream vortex) only occurs when the crosswind shear is moderate or weak at the altitude of the vortex cores. When a stronger wind shear, with negative vorticity, is superimposed on the vortex pair, the upstream vortex (with the same sign vorticity as the crosswind) may have a higher elevation than the downstream vortex, due to the shearing rotation of the crosswind itself. Then the vortex system will tilt in the opposite sense. How the vortex system is going to tilt is case dependent. It depends on whether the crosswind effects due to the ground boundary layer separation are important or whether the wind shear effects rotating the plane of the vortex core dominate. This is a topic for future research. The work shown here addresses only the weak wind shear effects which can be found under some typical atmospheric conditions.

The influence of stratification on vortex trajectories with cross wind is shown in Figures 9.4 and 9.5, with a non-dimensional Brunt-Väisälä frequency of N=0.3 (and Re=1,000, δ=10, U_∞=0.1). Comparing those trajectories with Figures 9.1 and 9.2, it can be seen that the vortex falling back (toward the ground plane after rebound) phenomenon, caused by the body force effects, as discussed in the previous chapter, is present in this case, too. The secondary vorticity field, Figure 9.6, created by the density departure depicted in Figure 9.7, causes this downward motion of the vortex pair. The ground boundary layer under the right (downstream) vortex is still thickened by the crosswind effects in this case and thus the vortex pair tilts in the same way as the case without stratification effects. These results show that crosswind and stratification can have significant effects on the vortex wake system simultaneously.

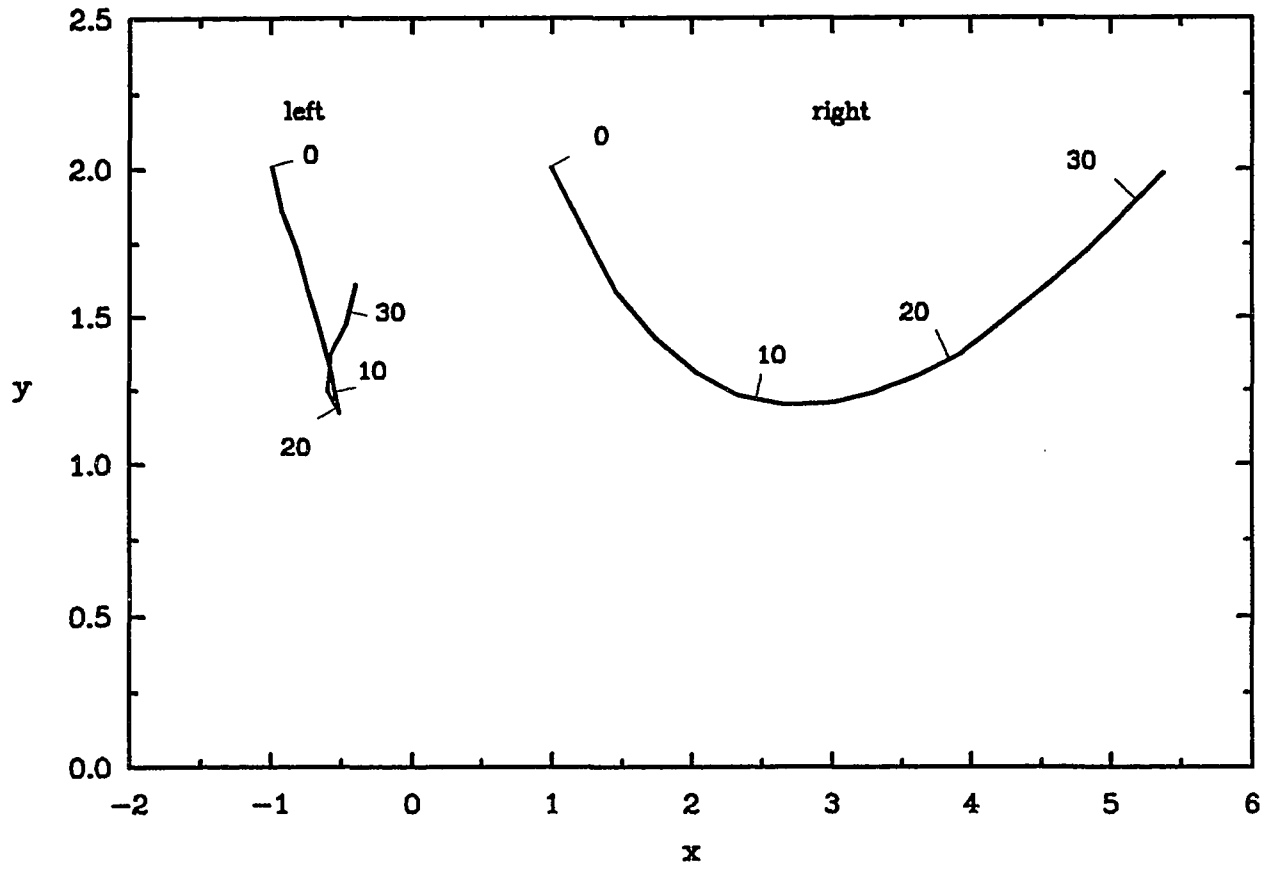

Figure 9.1 Vortex pair trajectories under crosswind effects at Re=1,000, δ=10, U_∞=0.1

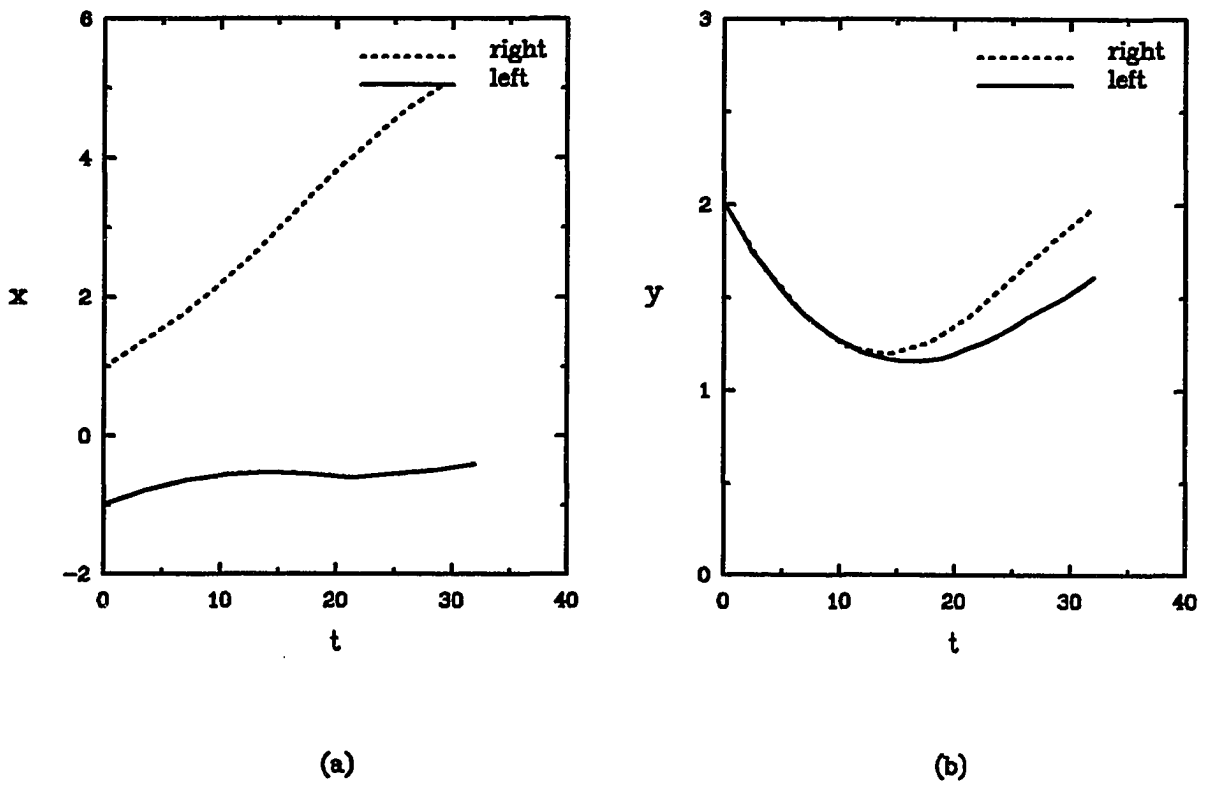

Figure 9.2 Comparison of the influence of crosswind effects on (a) Lateral vortex position histories, and (b) Elevation histories, Re=1,000, δ=10, U_∞=0.1

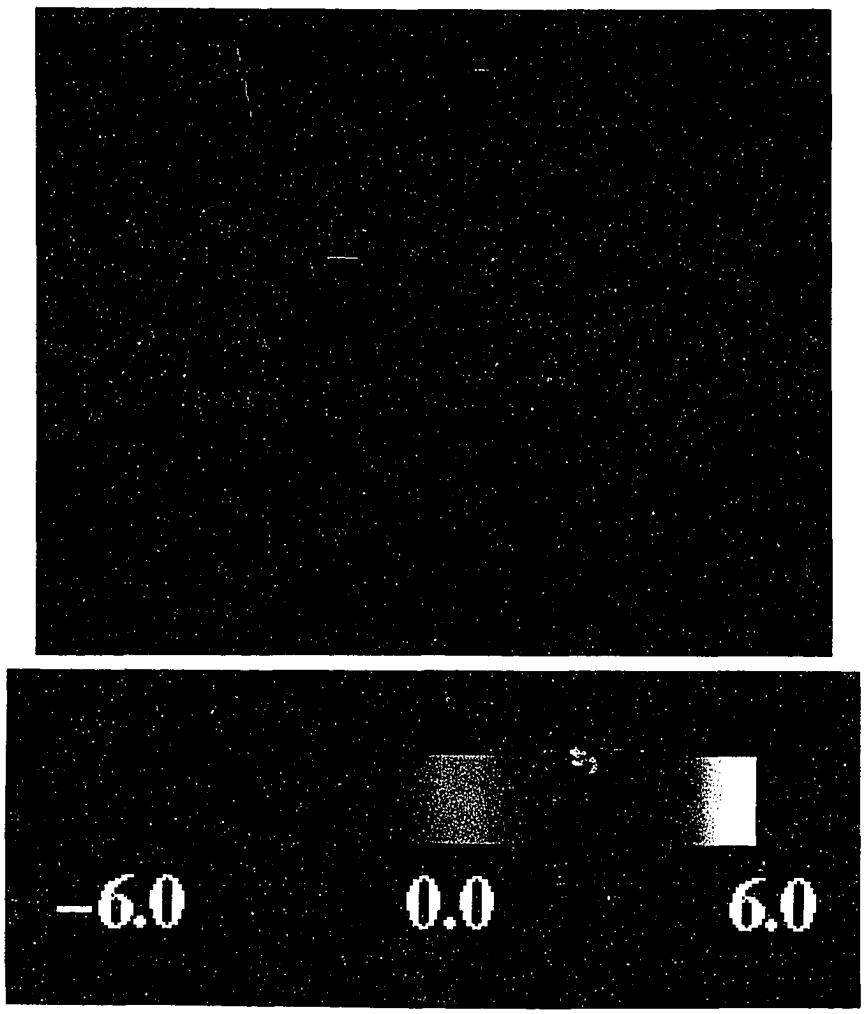

(a) Vorticity contours as t=12

Figure 9.3 Color contours of vorticity field at (a) t=12, (b) t=24, Re=1,000, δ=10, U_∞=0.1

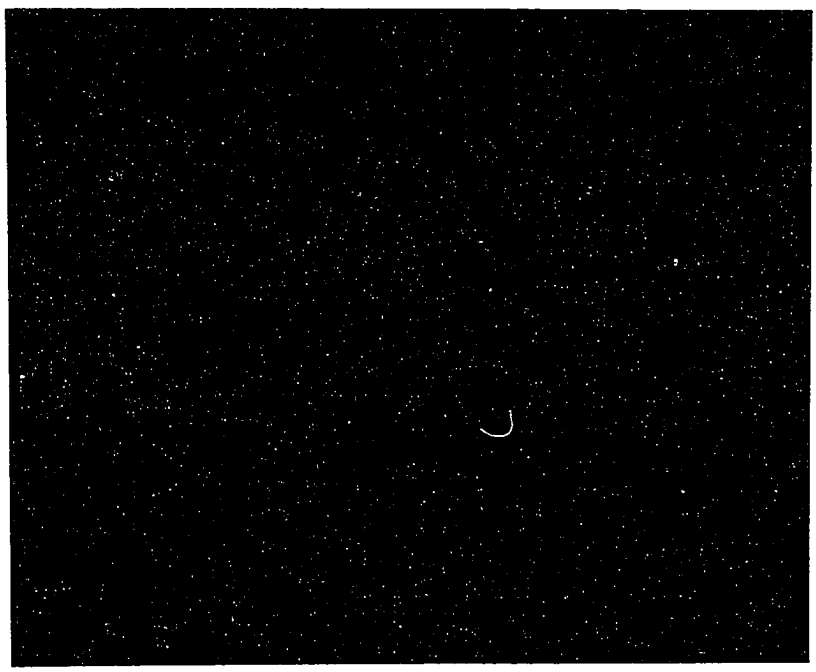

(b) Vorticity contours as t=24

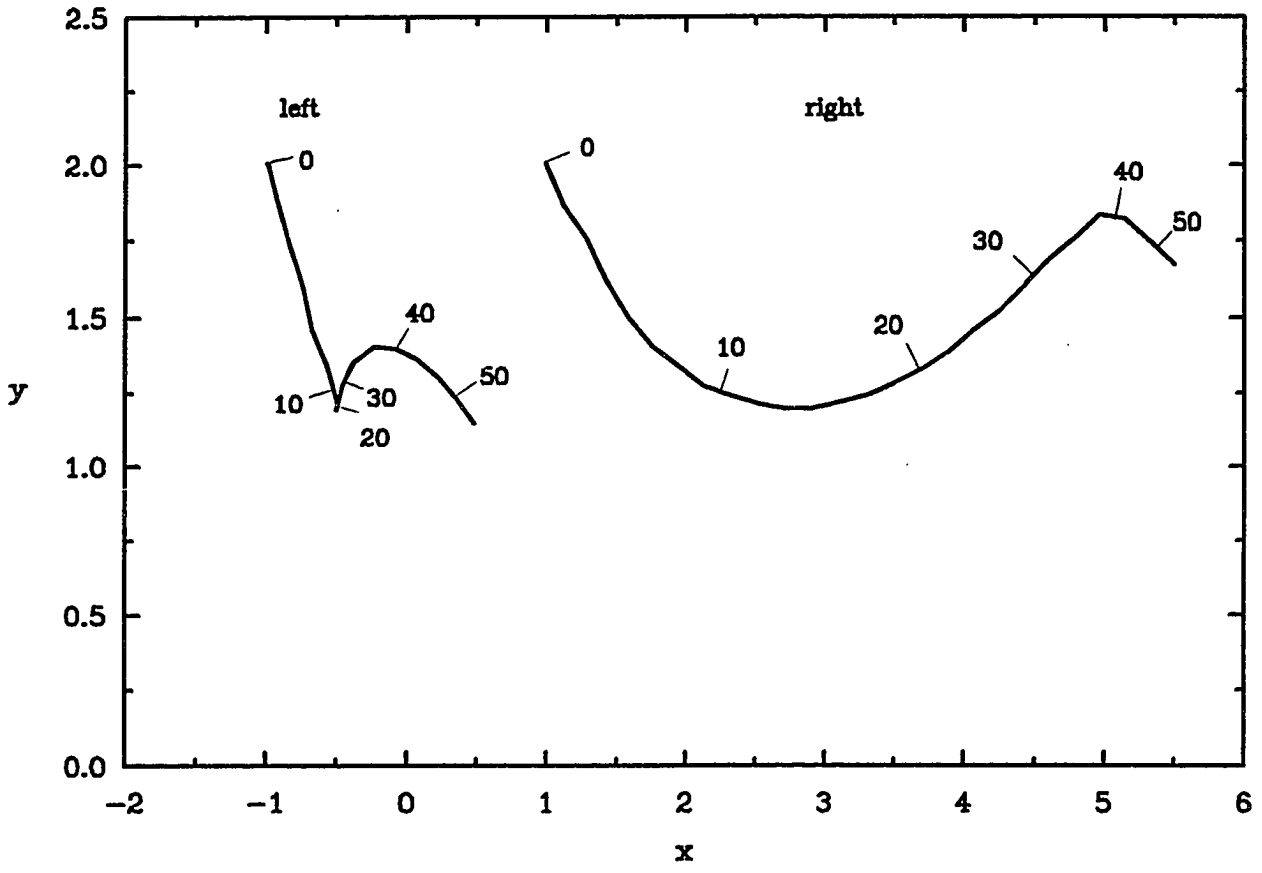

Figure 9.4 Influence of stratification on vortex pair trajectories under crosswind effects at Re=1,000, δ=10, U_∞=0.1

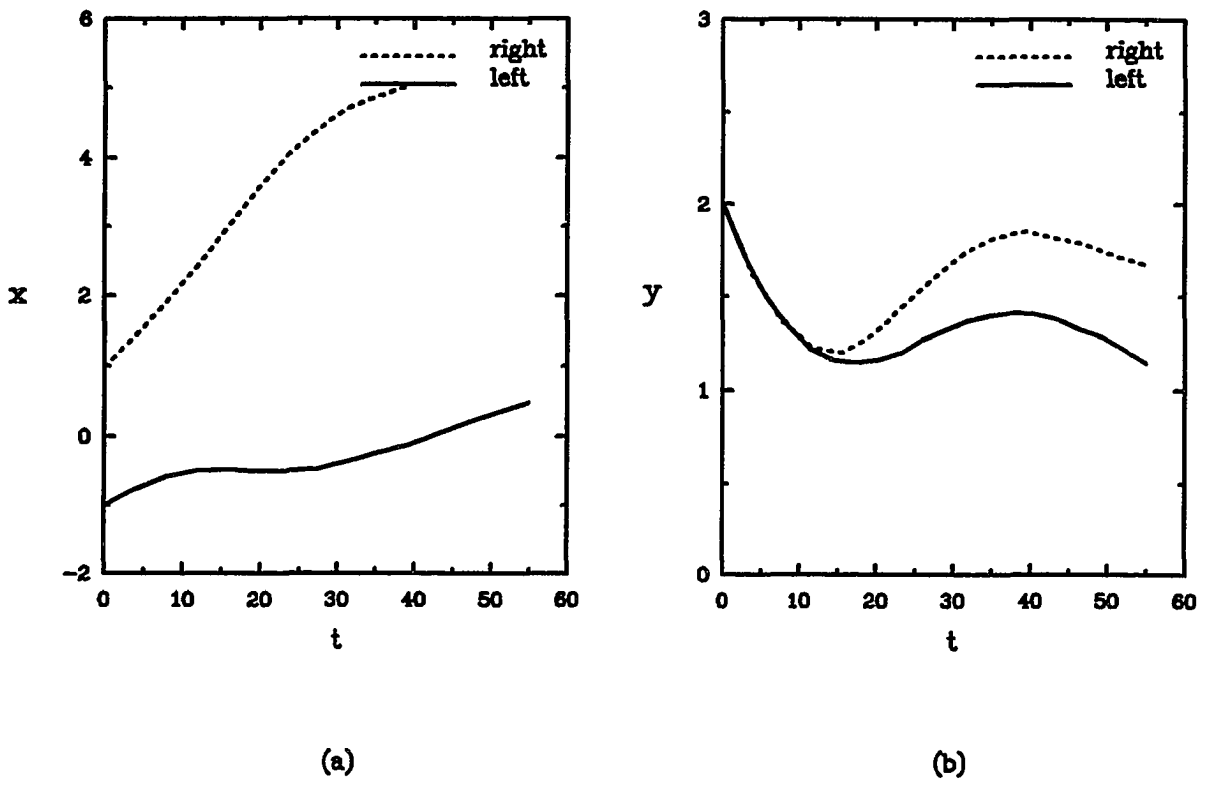

Figure 9.5 Comparison of influence of stratification on (a) lateral vortex position histories, (b) elevation histories, between left and right vortex, at Re=1,000, δ=10, U_∞=0.1

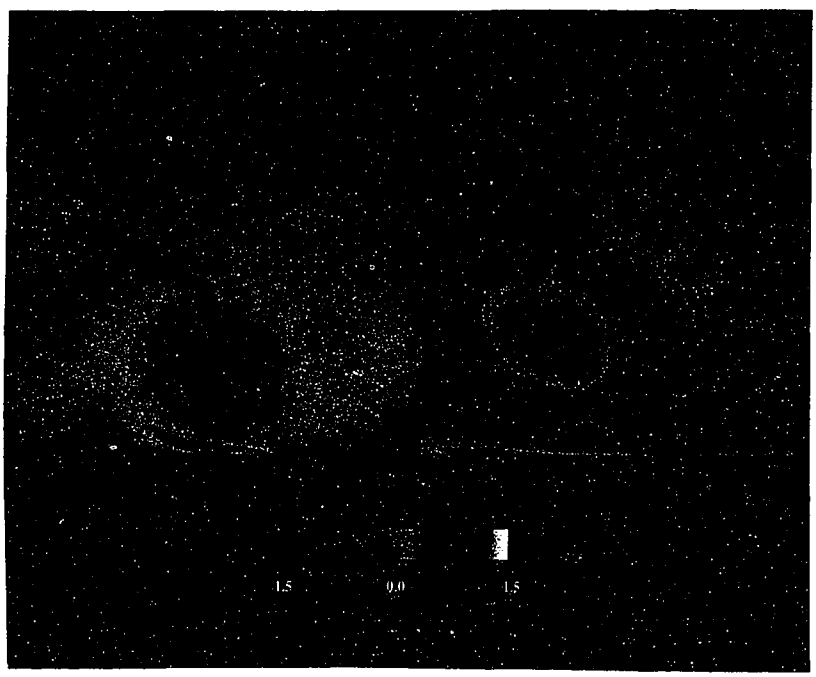

Figure 9.6 Color contours of vorticity field with stratification effects at t=50 , N=0.3, Re=1,000, δ=10, U_∞=0.1

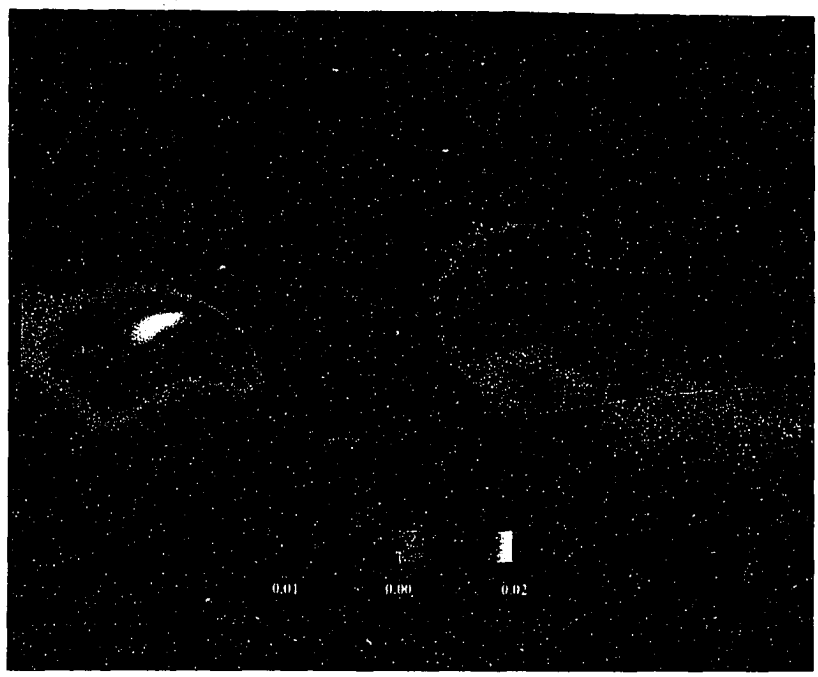

Figure 9.7 Color contours of density departure field at t=50 , N=0.3, Re=1,000, δ=10, U_∞=0.1

Chapter 10 Conclusions

This study has developed a two-dimensional, unsteady viscous numerical simulation of a vortex pair, which can include ground-plane interactions, stratification, crosswind and turbulence effects. The vorticity-streamfunction formulation was found to be an effective method, permitting the accommodation of Reynolds stress, crosswind and buoyancy effects in the vortex wake predictions. While accurate experimental vortex/ground-plane interaction data are very limited, excellent agreement between the laminar predictions from this study and corresponding experimental results of Liu and Srnsky (1990) were obtained.

Proper dimensional arguments were developed which justify the use of Boussinesq approximations for modeling stratification effects near the ground-plane boundary layer. A Reynolds stress transport model was found necessary to simulate turbulent wake vortices because the various eddy-viscosity turbulent approximations all overpredicted viscous dissipation and were unable to handle vortex core relaminarization. A two-parameter asymptotic series expansion technique was developed which could model the initial evolution of the unsteady ground-plane boundary layer accurately for both laminar and turbulent vortices (since the turbulent system must evolve through an initially laminar boundary-layer development). The fixed grid currently used has produced acceptable numerical results.

The vortex rebound near the ground plane was found to be caused by ground boundary-layer separation, at least within the circulation Reynolds numbers of this study. The influence of Reynolds number has shown that lower circulation Reynolds number cases, which obviously have stronger viscous effects in the flow field, produce thicker ground boundary layers. Both the lateral and vertical vortex rebound motion, as well as its strength, are reduced more rapidly than for higher Reynolds number cases.

Density/temperature stratification can have very pronounced effects on predicted vortex trajectories at high Brunt-Väisälä frequencies. The effects can confine both the lateral and vertical motion of the vortex system after its rebound and then destroy the primary vortices. Therefore, at these admittedly high stratification levels, it has been shown that the organized primary vortex hazard can be alleviated by stratification effects within the immediate vicinity of airport runways.

Turbulent vortex predictions have shown that turbulence influences vortex trajectories, particularly the vertical rebound altitude, more strongly than it influences the rate of change in vortex strength. This trend is shown in both stratified and unstratified turbulent vortex cases. The influence of stratification has a similar effect on the primary vortex, as shown in the laminar cases. Furthermore, the way in which the predicted turbulent kinetic energy distributions are shifted via the Reynolds stress transport model is more consistent with physical intuition than the predictions using less complete models.

Crosswind effects cause the upstream primary vortex to rebound less strongly than the downstream vortex. The ground boundary-layer thickness beneath the upstream vortex is reduced while that beneath the downstream vortex is increased. The advection by crosswind confines the lateral motion of the upstream vortex and causes the other

vortex to drift further downstream. Strong stratification still has significant effects on the vortex wake when weak cross flows are present.

It is noted that while the infinite physical domain in the vertical direction gives less uncertainty on the boundary conditions, it restricts the moving grid speed in crosswind cases using the vorticity-streamfunction formulation. Since the vertical motion of the vortex system near the ground is affected only within several wing spans, a finite domain approximation should be tested for the vertical bounds of the physical domain. Effects of strong shear cross flows could then be resolved properly if a modified moving grid was used.

While low Reynolds number (on the order of 10^2) flow cases should also be tested for the purpose of studying fundamental mechanisms for vortex/ground boundary-layer interaction, rather than for aircraft wake vortex predictions, high Reynolds number (on the order of 10^7) vortex wake behavior should be predicted. The Reynolds numbers that can be resolved using the current grid and computer resources remain approximately two orders of magnitude lower than those anticipated for realistic flight conditions associated with large commercial aircraft. Therefore, considerable effort should be devoted to defining the simulation limits for this numerical approach. The grid resolution problem for high Reynolds numbers should be considered and the possibility of using adaptive grid should be investigated in future research. Furthermore, the three dimensional effects of axial velocity deficit or excess must be addressed.

It is difficult to quantify vortex wake hazard. Differences between wake vortex safety criteria have been found (Critchley, 1991). No suitable theoretical description of the hazard is yet available. The ultimate goal of future research is to provide more

rational vortex hazard prediction capabilities than those which have been used previously for airports.

Bibliography

Anderson, C. R. 1986 On vorticity boundary conditions. Center for Large Scale Scientific Computation, Stanford University, Report CLaSSiC 86-14.

Anderson, D. A., Tannehill, J. C. and Pletcher R. H. 1984 *Computational Fluid Mechanics and Heat Transfer*, Hemisphere.

Atias, M. and Weihs, D. 1984 Motion of aircraft trailing vortices near the ground. *J. Aircraft* **21**, 783-786.

Ayad, S. S. and Cermak, J. E. 1980 A turbulence model for tornado-like swirling flows. *Vortex Flows*, edited by Swift, W. L., Barna, P. S. and Dalton, C., The Winter Annual Meeting of ASME, Chicago, Illinois, Nov., 1980.

Bandyopadhyay, P. R., Stead, D. J. and Ash, R. L. 1991 Organized nature of a turbulent trailing vortex. *AIAA J.* **29**, 1627-1633.

Barker, S. J. and Crow, S. C. 1977 The motion of two-dimensional vortex pairs in ground effect. *J. Fluid Mech.* **82**, 659-671.

Bernal, L. P., Hirst, A., Kwon, J. T. and Willmarth, W. W. 1989 On the interaction of vortex rings and pairs with a free surface for varying amounts of surface active agent. *Phys. of Fluids A.* **1**, 2001-2004.

Bilanin, A. J., Teske, M. E., Donaldson, C. duP. and Williamson, G. G. 1977 Vortex interactions and decay in aircraft wakes. NASA Contractor Report, NASA CR-2870.

Bilanin, A. J., Teske, M. E. and Hirsh, J. E. 1978 Neutral atmospheric effects on the dissipation of aircraft vortex wakes. *AIAA J.* **16**, 956-961.

Bozeman, J. D. and Dalton, C. 1973 Numerical study of viscous flow in a cavity. *J. Computational Physics* **12**, 348-363.

Bradshaw, P 1973 Effects of streamline curvature on turbulent flows. *AGARDograph* No. 169.

Brashear, M. R., Logan, N. A. and Hallock, J. N. 1975 Effect of wind shear and ground plane on aircraft wake vortices. *J. Aircraft* **12**, 830–833.

Burnham, D. C., Hallock, J. N., Tombach, I. H., Brashears, M. R. and Barber, M. R. 1978 Ground based measurements of a B-747 aircraft in various configurations. U. S. Dept. of Transportation Report FAA-RD-78–146, December.

Bushnell, D. 1991 Turbulence modeling in aerodynamic shear flow: status and problems. 29th Aerospace Sciences Meeting, Reno, Nevada, AIAA Paper 91–0214.

Childs, R. 1990 Turbulence modeling for impinging jets. 28th Aerospace Sciences Meeting, January 1990, Reno, Nevada, AIAA Paper No. 90–0022

Chorin, A. J. 1973 Numerical study of slightly viscous flow. *J. Fluid Mech.* **57**, 785–796.

Chorin, A. J. 1978 Vortex sheet approximation of boundary layers. *J. Computational Phys.* **27**, 428–442.

Critchley, J. B. 1991 Wake vortex: the program in the United Kingdom. *Proceedings of the Aircraft Wake Vortices Conference*, Washington, D.C., October 1991.

Crow, S. C. 1970 Stability theory fro a pair of trailing vortices. *AIAA J.* **8**, 2172–2179.

Crow, S. C. 1974 Motion of a vortex pair in a stably stratified fluid. Poseidon Research Report No. 1.

Crow, S. C. and Bate, E. R. Jr. 1976 Lifespan of trailing vortices in a turbulent atmosphere. *J. Aircraft* **13**, 476–482.

Deardorff, J. W. 1973 The use of subgrid equations in a three-dimensional model of atmospheric turbulence. *J. Fluids Engineering* **95**, 429–438.

Dee, F. S. and Niclolas, O. P. 1968 Flight measurement of wing tip vortex motion near the ground. British Aeronautical Research Council, London, England, CP 1065.

Delisi, D. P., Robins, R. E. and Fraser, R. B. 1987 The effects of stratification and wind shear on the evolution of aircraft wake vortices near the ground: Phase I Results. Northwest Research Associates, Inc. NWRA-87-R006.

Donaldson, C. duP. 1972a Calculation of turbulent shear flows for atmospheric and vortex motions. *AIAA J.* **10**, 4–12.

Donaldson, C. duP. 1972b The relationship between eddy-transport and second-order closure models for stratified media and for vortices. *Free Turbulence Shear Flows Conference Proceedings* July 1972, NASA Langley Research Center, Hampton, Virginia

Donaldson, C. duP. 1973 Construction of a dynamic model of the production of atmospheric turbulence and the dispersal of atmospheric pollutants. *Workshop on Micrometeorology*, edited by D. A. Haugen, Science Press, Pa., 313–390.

Donaldson, C. duP. and Bilanin, A. J. 1975 Vortex wakes of conventional aircraft. AGARDograph No. 204.

Donaldson, C. duP. and Sullivan, R. D. 1971 Decay of an isolated vortex. *Aircraft Wake Turbulence and Its Detection*, edited by J. H. Olsen *et al.*, Plenum Press, New York, 389–411.

Dutton, J. A. and Fichtl, G. H. 1969 Approximate equations of motion for gases and liquids. *J. Atmospheric Sciences* **26**, 241–254.

Gebhart, B. 1973 Natural convection flows and stability. *Advances in Heat Transfer*, **9**, edited by Irvine, T. F., Jr. and Hartnett, J. P., Academic Press.

Greene, G. C. 1986 An approximate model of vortex decay in the atmosphere. *J. Aircraft* **23**, 566–573.

Hallock, J. N., editor, 1992 *Proceedings of the Aircraft Wake Vortices Conference*, Washington, D.C., October 1991, Documents DOT/FAA/SD-92/1.1 and 1.2, 1992.

Harvey, J. K. and Perry, F. J. 1971 Flowfield produced by trailing vortices in the vicinity of the ground. *AIAA J.* **9**, 1659–1660.

Hecht, A. M., Bilanin, A. J., Hirsh, J. E. and Snedeker, R. S. 1979 turbulent vortices in stratified fluids. 17th Aerospace Sciences Meeting, New Orleans, La., AIAA Paper No. 79-0151.

Hirsh, R. S. 1985 A numerical simulation of vortex motion in a stratified environment and comparison with experiments. Johns Hopkins APL Technical Digest, **6**, 203–210.

Hoffmann, E. R. and Joubert, P. N. 1963 Turbulent line vortices. *J. Fluid Mech.* **16**, 395–411.

Ivanov, A. V., Lebedev, A. V., Ostrovskii, L. A. and Piskarev, A. L. 1987 Experimental investigation of the motion of laminar vortex pairs in a stratified fluid. *Fluid Dynamics* **22**, 322–325.

Iversen, J. D. 1974 Inviscid to turbulent transition of trailing vortices. Technical Report ISU-ERI-AMES-74241, Engineering Research Institute, Iowa State University, Ames, Iowa.

Kandil, O. A. and Chuang, H. A. 1990 Computation of vortex-dominated flow for a delta wing undergoing pitching oscillation. *AIAA J.* **28**, 1565–1572.

Kandil, O. A., Wong, T. C. and Liu, C. H. 1991 Analysis and computation of trailing vortices and their hazardous effects. *Proceedings of the Aircraft Wake Vortices Conference*, Washington, D.C., October 1991.

Kuhn, G. D. and Nielson, J. N. 1972 Analytical studies of aircraft trailing vortices. AIAA Paper 72–42.

Lamb, H. 1945 *Hydrodynamics* 6th edition, Dover.

Launder, B. E. and Spalding, D. B. 1974 Numerical computation of turbulent flows. *Computer Methods in Applied Mechanics and Engineering* **3**, 269–289.

Leonard, A. 1980 Vortex methods for flow simulation. *J. Computational Phys.* **37**, 289–335

Lewellen, W. S., Teske, M. E. and Donaldson, C. duP. 1976 Variable density flows computed by a second-order closure description of turbulence. *AIAA J.* **14**, 382–387.

Lewellen, W. S., Teske, M. E. and Sheng, Y. P. 1979 Wind and pressure distribution in a tornado. *Proceedings of the Fifth International Conference on Wind Engineering* edited by Cermak, J. E., Fort Collins, Colorado, Pergamon Press. 116–126.

Lissaman, P. B. S., Crow, S. C., Maccready, P. B., Jr., Tombach, I. H. and Bate, E. R., Jr. 1973 Aircraft vortex wake descent and decay under real atmospheric effects. Department of Transportation Report No. FAA-RD-73–120.

Liu, C. H. and Ting, L. 1987 Interaction of decaying trailing vortices in spanwise shear flow. *Computers & Fluids* **15**, 77–92.

Liu, H. T. 1992 Effects of ambient turbulence on the lifespan of a trailing vortex wake. *J. Aircraft* **29**

Liu, H. T., Hwang and Srnsky R. A. 1991 Physical modeling of ground effects on vortex wakes. *J. Aircraft* **29**

Liu, H. T. and Srnsky R. A. 1990 Laboratory investigation of atmospheric effects on vortex wakes. Flow Research Inc. Technical Report No. 497.

Lumley, J. L. 1983 Turbulence modeling. *J. Applied Mech.* **50**, 1097–1103.

Mihaljan, J. M. 1962 Arigorous exposition of the Boussinesq approximations applicable to a thin layer of fluid. *Astrophys. J.* **136**, 1126–1133.

Moore, D. W. and Saffman, P. G. 1971 Structures of a line vortex in a imposed strain. *Aircraft Wake Turbulence and Its Detection*, edited by J. H. Olsen et al., Plenum Press, New York, 339–354.

Nam, S. 1990 Higher-order boundary-layer solution for unsteady motion of a circular cylinder. *J. Fluid Mech.* **214**, 89–110.

Ohring, S. and Lugt, H. J. 1991 Interaction of a viscous vortex pair with a free surface. *J. Fluid Mech.* **227**, 47–70.

Orlandi, P. 1990 Vortex dipole rebound from a wall. *Phys. Fluids A.* **2**, 1429–1436.

Oseen, C. W. 1911 Über wirbelbewegung in einer meibenden flüssigkeit. *Arkiv För Mathematic Astronomi Och Fysik* **7**, 1–13.

Peace, A. J. and Riley, N. 1983 A viscous vortex pair in ground effect. *J. Fluid Mech.* **129**, 409–426.

Phillips, W. R. C. and Graham, J. A. H. 1984 Reynolds-stress measurements in a turbulent trailing vortex. *J. Fluid Mech.* **147**, 353–371.

Plate, E. J. 1971 *Aerodynamic Characteristics of Atmospheric Boundary Layers*, U. S. Atomic Energy Commission, Office of Information Services.

Ragsdale, R. G. 1961 Applicability of mixing length theory to a turbulent vortex system. NASA TN D-1051, Lewis Research Center, Cleveland, Ohio, Aug. 1961.

Raj, P. and Iversen, J. D. 1979 Computational simulation of turbulent vortex merger and decay. 17th Aerospace Sciences Meeting, New Orleans, La., AIAA paper No. 79-0278.

Roach, P. J. 1972 *Computational Fluid Dynamics*, Hermosa Pub.

Robins, R. E. and Delisi, D. P. 1990 Numerical study of vertical shear and stratification effects on the evolution of a vortex pair. *AIAA J.* **28**, 661–669.

Rossow, V. J. 1976 Convective merging of vortex cores in lift-generated wakes. 9th Fluid and Plasma Dynamics Conference, San Diego, Calif., AIAA Paper No. 76–415.

Rubin, S. G. and Harris, J. E. 1975 Numerical studies of incompressible viscous flow in a driven cavity. NASA SP-378.

Saffman, P. G. 1973 Structure of turbulent line vortices. *Phys. of Fluids* **16**, 1181–1188.

Saffman, P. G. 1979 The approach of a vortex pair to a plane surface in inviscid fluid. *J. Fluid Mech.* **92**, 497–503.

Sarpkaya, T. and Johnson, S. K. 1983 Evolution of aircraft trailing vortices in a stratified fluid. AIAA 21st Aerospace Sciences Meeting, January 1983, Reno, Nevada, AIAA-83–0564

Sarpkaya, T. and Daly, J. J. 1987 Effect of ambient turbulence on trailing vortices. *J. Aircraft* **24**, 399–404.

Schilling, V. K. 1992 Motion and decay of trailing vorticies within the atmospheric surface layer. *Beitr. Phys. Atmosph.* **65**, 157–169.

Schlichting, H. 1979 *Boundary-Layer Theory* 7th edition, McGraw-Hill.

Schumann, D. 1977 Realizability of Reynolds stress turbulence models. *Phys. of Fluids* **20**, 721–725.

Scorer, R. S. and Davenport, L. J. 1970 Contrails and aircraft downwash. *J. Fluid Mech.* **43**, 451–464.

Sloan, D. G., Smith, P. J. and Smoot, L. D. 1986 Modeling of swirl in turbulent flow systems. *Progress in Energy Combust. Sci.* **12**, 163–250.

Speziale, C. G. 1986 On the advantages of the vorticity-velocity formulation of the equations of fluid dynamics. NASA Contractor Report 178125, ICASE Report No. 86–35.

Spiegel, E. A. and Veronis, G. 1960 On the Boussinesq approximation for a compressible fluid. *Astrophys. J.* **131**, 442–447.

Swarztrauber, P. N. and Sweet, R. A. 1979 Algorithm 541, Efficient FORTRAN subprograms for the solution of separable elliptic partial differential equations [D3]. *ACM Trans. on Math. Software* **5**, 352–364.

Taylor, G. L. 1923 Stability of viscous liquid contained between two rotating cylinders. *Phil. Trans. Roy. Soc.* **223**, 289–343.

Ting, L. 1983 On the application of the integral invariants and decay laws of vorticity distributions. *J. Fluid Mech.* **127**, 497–506.

Tomassian, J. D. 1979 The motion of a vortex pair in a stratified medium. Ph.D. Dissertation in Engineering, University of California at Los Angeles

Tombach, I. 1971 Transport of a vortex wake in a stably stratified atmosphere. *Aircraft Wake Turbulence and Its Detection*, edited by J. H. Olsen et al., Plenum Press, New York, 41–56.

Tombach, I. 1973 Observation of atmospheric effects of vortex wake behavior. *J. Aircraft* **10**, 641–647.

Turner, J. S. 1973 *Buoyancy Effects in Fluids*, Cambridge University Press.

U. S. Standard Atmospheric Tables 1962.

van Dyke, M. 1976 *Perturbation Method in Fluid Mechanics* Stanford: Parabolic.

Widnall, S. E. 1975 The structure and dynamics of vortex filaments. *Annual Reviews of Fluid Mech.* **11**, 141–165.

Wong, T. C., Kandil, O. A. and Liu, C. H. 1992 Computation of vortex wake flows and control of their effects on trailing wings. AIAA Atmospheric Flight Mechanics Conference, Hilton Head, SC, AIAA Paper 92–4429–CP.

Appendix A: Development of Two-Dimensional Equations of Motion in Unsteady Reference of Frames

The dimensionless two-dimensional momentum equations in primitive variables are

$$\frac{\partial u_f}{\partial t_f} + u_f \frac{\partial u_f}{\partial x_f} + v_f \frac{\partial u_f}{\partial y_f} = -\frac{\partial p_f}{\partial x_f} + \frac{1}{Re}\nabla_f^2 u_f \tag{A.1}$$

and

$$\frac{\partial v_f}{\partial t_f} + v_f \frac{\partial v_f}{\partial x_f} + v_f \frac{\partial v_f}{\partial y_f} = -\frac{\partial p_f}{\partial y_f} + \frac{1}{Re}\nabla_f^2 v_f \tag{A.2}$$

in space fixed coordinates.

With the transformation from the space fixed coordinates to non-inertia, translational moving coordinates with moving velocity components $U_\infty(t)$ and $V_\infty(t)$:

$$\frac{\partial}{\partial x_f} = \frac{\partial}{\partial x}, \tag{A.3}$$

$$\frac{\partial}{\partial y_f} = \frac{\partial}{\partial y}, \tag{A.4}$$

$$\frac{\partial}{\partial t_f} = \frac{\partial}{\partial t} - U_\infty(t)\frac{\partial}{\partial x} - V_\infty(t)\frac{\partial}{\partial y}, \tag{A.5}$$

these equations become

$$\frac{\partial u_f}{\partial t} + (u_f - U_\infty)\frac{\partial u_f}{\partial x} + (v_f - V_\infty)\frac{\partial u_f}{\partial y} = -\frac{\partial p_f}{\partial x} + \frac{1}{Re}\nabla^2 u_f, \tag{A.6}$$

and

$$\frac{\partial v_f}{\partial t} + (u_f - U_\infty)\frac{\partial v_f}{\partial x} + (v_f - V_\infty)\frac{\partial v_f}{\partial y} = -\frac{\partial p_f}{\partial y} + \frac{1}{Re}\nabla^2 v_f \,, \tag{A.7}$$

respectively. Since the thermodynamic pressure does not change with the motion of coordinates, that is,

$$p = p_f \tag{A.8}$$

and the velocity components in the moving coordinates have the relation with these in the space fixed coordinates as

$$u = u_f - U_\infty \text{ and } v = v_f - V_\infty \,, \tag{A.9}$$

Eqns. (A.6) and (A.7) can be rewritten as

$$\frac{\partial u}{\partial t} + \frac{dU_\infty}{dt} + u\frac{\partial u}{\partial x} + v\frac{\partial u}{\partial y} = -\frac{\partial p}{\partial x} + \frac{1}{Re}\nabla^2 u \,, \tag{A.10}$$

and

$$\frac{\partial v}{\partial t} + \frac{dV_\infty}{dt} + u\frac{\partial v}{\partial x} + v\frac{\partial v}{\partial y} = -\frac{\partial p}{\partial y} + \frac{1}{Re}\nabla^2 v \,. \tag{A.11}$$

In Eqns. (A.10) and (A.11), it can be seen that after the transformation, Eqns. (A.3)-(A.5), extra terms have been produced, representing the accelerations of the moving frames.

Then, if the cross product is applied to Eqns. (A.10) and (A.11), i.e., $\frac{\partial}{\partial x}$(A.11) $-$ $\frac{\partial}{\partial y}$(A.10), the extra acceleration terms will disappear and the following vorticity transport equation can be obtained:

$$\frac{\partial \zeta}{\partial t} + u\frac{\partial \zeta}{\partial x} + v\frac{\partial \zeta}{\partial y} = \frac{1}{Re}\nabla^2 \zeta \,, \tag{A.12}$$

where

$$\zeta = \frac{\partial v}{\partial x} - \frac{\partial u}{\partial y} \,. \tag{A.13}$$

In deriving Eqn. (A.12), the solenoidal relation of the velocity field in the moving coordinates has been used. Mathematically, it can be observed from Eqn. (A.9) that the spatial derivatives in the transformed coordinates are the same in the fixed coordinates and thus the solenoidal relation does not change. Physically, the incompressibility of the flow field cannot be changed by the moving frame of reference. Hence, the streamfunction equation, which is based on the solenoidal relation of the velocity field, is the same as Eqn. (3.43). Hence, the transparency the vorticity-streamfunction formulation in two-dimensional flow has been proved from above procedures.

This case can be considered as a special case of Speziale's (1986) vorticity-velocity formulation in the non-inertia frame of reference.